IMPACT OF ENGINE ICING ON JET ENGINE COMPRESSOR FLOW DYNAMICS

A Thesis
Presented to
The Academic Faculty

by

Reema Kundu

In Partial Fulfillment
of the Requirements for the Degree
Doctor of Philosophy in the
School of Aerospace Engineering

Georgia Institute of Technology
May 2015

IMPACT OF ENGINE ICING ON JET ENGINE COMPRESSOR FLOW DYNAMICS

Approved by:

Dr. J.V.R. Prasad, Advisor
School of Aerospace Engineering
Georgia Institute of Technology

Dr. J. I. Jagoda
School of Aerospace Engineering
Georgia Institute of Technology

Dr. Jerry M. Seitzman
School of Aerospace Engineering
Georgia Institute of Technology

Dr. Rajkeshar Singh
GE Global Research

Dr. Lakshmi N. Sankar
School of Aerospace Engineering
Georgia Institute of Technology

Date Approved: 21 February 2015

To Ma and Baba

ACKNOWLEDGEMENTS

My thesis would not have been possible without the several people who helped me during my years at Georgia Tech. I would like to express my gratitude and thanks to my advisor Dr. J.V.R. Prasad for his continuous support, guidance and patience throughout the course of this research work. I would like to thank Dr. Lakshmi Sankar, Dr. Jerry Seitzman, Dr. Jagoda and Dr. Rajkeshar Singh for serving on my thesis advisory committee. Their feedback played an important role in adding to the quality of my thesis.

Dr. Manuj Dhingra, for the initial development of the program which was crucial towards my thesis work. Dr. Yedidia Neumeier for his technical advise and guidance.

The financial support from GE Aviation, GE Global Research and Georgia Tech is grateful acknowledged. Andy Breeze-Stringfellow, Tsuguji Nakano and Peter Szucs at GE Aviation and Rajkeshar Singh and Swati Saxena at GE Global Research significantly contributed to my understanding of the physical and computational aspects of my thesis problem. They also made available data required in my work.

James Darrell and Rakesh Srivastava from Honeywell for providing the data and technical feedback towards validation of my thesis work.

All staff of the Aerospace Offices for helping me with the administrative details. Dr. Jeff Jagoda for serving as my thesis committee member and helping me through tough times at school. To past and present lab mates, roommates and friends for their invaluable friendship and support: GiYun Chung, Yong-Boon Kong, Mark Lopez, Prashant Khare and Udita Brahmachari. A special note of thanks to Nicolas Reveles for being there for me through all these difficult years.

Finally, I want to thank my brother for his encouragement and dedicate this thesis to my parents whose unwavering faith in my abilities, patience and sacrifices through all these years helped me survive through graduate school and made the pursuit of this degree worthwhile.

TABLE OF CONTENTS

LIST OF TABLES

LIST OF FIGURES

NOMENCLATURE

$\dot{M}_p$	discrete phase mass flow rate.
$\dot{m}$	mass flow rate.
$\dot{m}_b$	bleed mass flow rate.
$\dot{m}_v$	vapor mass flow rate.
$\dot{m}_{\text{melt}}$	melting rate of mass of water.
$\dot{w}_s$	shaft power per unit volume.
$\mathbf{F}$	vector for the flux variables in Euler equation.
$\mathbf{Q}$	vector for the source terms in Euler equation.
$\mathbf{V}$	vector for the conservative variables in Euler equation.
D_ν	air-water molecular diffusion coefficient.
L_{melt}	latent heat of fusion.
L_{vap}	latent heat of evaporation.
Nu	Nusselt number.
Pr	Prandtl number.
RH	percentage relative humidity.
Re_p	Reynolds number.
Sc	Schmidt number.
Sh	Sherwood number.
$\mathrm{h_m}$	mass transfer coefficient.
h	Heat transfer coefficient.
k	coefficient of thermal conductivity.
$\mathrm{MW_d}, \mathrm{MW_v}$	molecular weight of dry air and vapor, respectively.
A	flow-path area.
A_c	area of the gas flow path with blockage due to discrete particles included.
c	speed of sound.
C_D	drag coefficient.
C_p	specific heat capacity at constant pressure.

D_p	discrete particle diameter.
dV	elemental control volume.
e_w^*	saturated vapor pressure of water.
e_c	specific internal energy of continuous phase.
e_w	partial pressure of water vapor.
F_D	drag force.
f_x	axial blade force per unit volume.
f_θ	circumferential blade force per unit volume.
h_0	total enthalpy.
k_T	throttle constant.
L	total compressor length.
M	Mach number.
m_p	mass of single ice crystal or water droplet.
N	compressor rpm.
N_p	Number of discrete elements.
p_0	gas total pressure.
p_g	gas static pressure.
p_{amb}	ambient pressure.
q	Specific humidity.
R_d, R_v	specific gas constant of dry air and vapor, respectively.
r_m	pitchline radius.
s_{bleed}	bleed source term.
s_{energy}	gas-discrete phase energy coupling term.
s_{mass}	mass source term.
s_{mom}	gas-discrete phase momentum coupling term.
s_{vapor}	gas-discrete phase mass source term.
t	time instant.
T_0	gas total temperature.
T_g	gas static temperature.

T_p	discrete particle temperature.
T_{amb}	ambient temperature.
u	axial component of flow velocity.
u_p	discrete particle velocity.
U_{meanline}	meanline blade rotational speed, $\Omega r_{meanline}$.
v_θ	circumferential component of flow velocity.
x	compressor axial coordinate.
α	absolute angle $\tan^{-1}\left(\frac{v_\theta}{u}\right)$.
α_c	continuous phase volume fraction.
α_d	discrete phase volume fraction.
γ	specific heat ratio.
μ_c	viscosity of air.
$\rho_{v,s}$	saturated vapor density at the surface of the discrete particle.
ρ_c	continuous phase density.
ϕ	flow coefficient, $u/\,\mathrm{U}_{\text{meanline}}$.
ψ_{fx}	axial force coefficient.
ψ_{f_θ}	circumferential force coefficient.

SUMMARY

Core engine icing has been recognized to affect a wide variety of engines since the 1990's. This previously unrecognized form of icing occurs in flights through high altitude convective regions and vicinity of thunderstorms. Engine icing events involve power loss or damage associated to the engine core, namely instabilities such as compressor surge, stall, engine rollback and even combustor flameout events. Unlike the sub-freezing environment required for accretion of supercooled water drops, "ice crystal icing" occurs deeper in the engine core where the local airflow temperature is significantly above freezing.

The effects on compressor performance are significant in understanding the response of the engine to ice ingestion. A methodology is developed that enables fast analysis of axial multistage compressors in the presence of ice ingestion. A one-dimensional axisymmetric flow model is used to simulate the continuous phase through the compressor. The steady state operation of dry air is validated with an industrial database. By changing an exit throttle, the point when the dry compressor mass flow rate slowly starts to drop, is predicted. The stage that is the first to locally collapse, causing the remaining stages and eventually the complete compressor failure, is determined.

The continuous flow model is then coupled with a Lagrangian model for the discrete phase in a framework that conserves mass, momentum and energy. Ice ingestion leads to vapor formation through the compressor, modifying the properties of the carrier gas in the simulation. From numerical simulations of the coupled, continuous-discrete phase flow model, it is observed that a rematching of the stages across the compressor occurs with increasing ice flow rates to accommodate loss of energy to the ice flow. The migration of the operating point towards the stall point at the rear stage eventually causes the compressor to stall. The onset of stall is characterized by initial oscillations followed by a rapid decay of pressures of the last stage with the instability traveling quickly towards the front of the compressor. Effectively, a reduction in the compressor stall margin is observed as the ice

flow rate increases.

Further, the relevance of factors such as blockage due to discrete particles and break-splash semi-empirical models in the icing physics, are analyzed through parametric studies. Conclusions are drawn that underscore the influence of the assumptions and models in prediction of the flow behavior in the presence of ice ingestion. Smaller ice crystal diameters have a greater influence on the gas flow dynamics in terms of a higher reduction in surge margin. The break empirical model for ice crystals and splash model for the droplets that are used to calculate the secondary particle size upon impact with rotor blades have a significant influence on the gas flow predictions.

CHAPTER I

INTRODUCTION

1.1 Motivation

Ice ingestion in engines is a serious safety and performance concern for modern aircraft. Since the mid-1990's several commercial and large transport aircraft have experienced engine power loss events linked to atmospheric ice ingestion, resulting in an impetus on research in modeling the engine icing phenomenon [80].

Mason and Grzych [59] and Mason et al. [60] have reviewed the impact of ice ingestion and shedding in aircraft engines. It was concluded from the flight test data that ice shed inside the engine core was responsible for power loss in large turbofan engines. Engine icing can potentially cause mechanical damage, either directly on impact, or indirectly by triggering compressor instabilities like surge or stall. Surge is a low frequency, essentially axisymmetric oscillation which involves the whole compression system. Rotating stall is a wave propagating in the circumferential direction at a fraction of rotor frequency, which is localized to the compressor blade row. Ice ingested into the compressor can eventually enter the combustion chamber resulting in a flame-out event.

There is a need to simulate the transient behavior of compressor flow field to ice ingestion, for understanding the physics related to compressor instabilities arising from ice ingestion. The flow interaction of the discrete phase, consisting of ice particles and water droplets, with the compressor airflow is a complex, coupled, multiphase flow phenomenon. Given the complex nature of the problem, a simplified model is required to avoid prohibitive computational costs associated with a three-dimensional unsteady simulation of the coupled flow in the compressor.

A separate aero-thermodynamic model is developed to represent the icing physics, which is then coupled with a quasi-one-dimensional axisymmetric gas flow model of the compressor. In addition, the numerical tool is also capable of handling a stage-wise analysis of a

multistage compressor for identifying a stalling stage in response to ice ingestion.

1.2 Background

1.2.1 Icing overview

The dynamics of ice accumulation on exposed aircraft and engine surfaces as an aircraft flies through a cloud of supercooled liquid droplets has been extensively studied and covered in existing FAA regulations [89, 28, 88, 106, 93]. Ice accretion is considered to be mainly caused by the impact and freezing of supercooled water droplets on cold surfaces. In-flight airframe ice accretion can seriously degrade aircraft performance and handling characteristics. Adverse aerodynamic effects of increased drag and loss of lift along with altered controllability can cause aircraft to stall. Traditionally anti-icing agents and deicing techniques are used to either remove or prevent ice accumulation on external surfaces of aircraft.

Wind tunnel experimentation and flight-testing needed for certification can incur high costs. This has prompted numerical design and analysis techniques, along with Computational Fluid Dynamics (CFD), for the detailed design as well concrete evaluation of options. Beaugendre et al. [5] have discussed the design of ice protection systems and icing certifications through cost-effective use of CFD.

Development for ice accretion simulation codes was initiated at the NASA Lewis Research center (LEWICE) to determine the ice build-up on the leading edge of airfoils. Leary [52] has given an exhaustive summary of the icing research at NASA. Extensive work toward the same goal has been carried out in the past two decades. Some other programs that have been developed internationally, include ONERA 3D icing code (France) [36], TRAJICE (UK) [2], FENSAP-ICE (CANADA) [97], CANICE (Canada) [32] and MULTI-ICE (Italy) [66]. Jorgenson et al. [105] have presented the incorporation of another NASA icing analysis tool, GlennICE, in the Numerical Propulsion System Simulation (NPSS) engine software. The above programs use Messinger model [65] to compute a freezing fraction that gives the portion of impinging droplet mass that freezes into a solid ice. The heat and mass balance equations are solved in the Messinger model using certain initial conditions

such as the wall heat transfer and droplet collection efficiency. The various icing tools differ in the techniques used to calculate these values. For example, LEWICE employs an integral boundary layer and the panel method to compute the heat transfer and droplet impingement on a surface in a Lagrangian framework [87]. On the other hand, FENSAP [97], uses a Reynold Averaged Navier-Stokes (RANS) code and volume fraction of water to compute the flowfield and droplet trajectory simultaneously in an Eulerian approach. Most of these efforts focus on icing predictions on wings, fuselages, winglets, radar, engine nacelle and other external stationary surfaces. Kim et al. [43] and Bain et al. [4] have discussed the modeling of ice formation on rotorcraft blades.

1.2.2 Engine core ice crystal icing

The adverse effects resulting from supercooled liquid droplet (SLD) exposure in the engine are generally as follows:

1. Ice shedding from inlet or fan blades can cause structural damage.
2. Ice build-up on engine sensors can result in control malfunction.
3. Blockage and reduced airflow from accretion on fan outlet guide vanes and booster inlet guide vanes can cause increased fuel consumption.
4. Nacelle drag increases from accreted ice.
5. Ice shed from booster IGV can cause compressor stall and combustor flameout.

Kind et al. [44] have reviewed the extensive research related to experimental and computational simulation of in-flight SLD icing. In these past studies, icing due to ice particle ingestion was neglected. It was believed that ice particles are benign, bouncing harmlessly off external surfaces and not affecting the hot core of jet engines. The engine airflow rate in flight was assumed high enough to prevent sufficient residence time for heat transfer to take place between the engine surfaces and ice particles. Also, engine temperatures quickly reached well above freezing as the air progressed downstream and were perceived as adequate to melt particles.

However, Lawson et al.[51] documented engine rollback events in flights maneuvering through the anvil region near the central core of a thunderstorm. Engine rollback is due to reduced compression efficiency characterized by an initial slow loss of power culminated by a rapid and uncommanded reduction of power to engine idle or sub-idle conditions. Contrary to the ice buildup in SLD conditions, when flying through anvil regions there were no detectable build-up of ice on aircraft external surfaces, and aircraft handling were not affected. However ice buildup, broken and shed into the engine compressor, were suspected to have caused the power loss. Analysis of meteorological conditions of thunderstorm anvils confirmed that the atmosphere had high ice-water content (HIWC) conditions.

The AirBridge Cargo (ABC) Boeing 747-8F icing event is one among the growing number of icing related incidents as reported by Hradecky [39]. Investigators noted that as the flight had entered into the region of ice crystals, the total air temperature (TAT) rose by 20 °C to −34 °C that indicated icing, with no sign of exterior aircraft icing, nor any echoes from radar. This temperature anomaly was followed by No. 2 engine experiencing surge, then No. 1 engine rollback ensued. The inspection of three of the four engines revealed damage to the high pressure compressor blades due to ice crystals. The event prompted Boeing to direct airlines to temporarily reroute 747-8s and GE Aviation-powered 787s from flying within 50 nautical miles of high-altitude, convective weather systems to prevent thrust loss caused by ice crystal build-up.

Mason et al.[61] have reported that since the mid-1990's several jet engine power loss events on aircraft have occurred at altitudes higher than 22,000 feet, the extreme upper limit recognized in the industry for supercooled liquid water droplets to exist. This is significant, because at such altitudes the hydrometeors are largely expected to be in the form of ice particles, implying "ice crystal icing", instead of conventional SLD icing conditions. The result has been a greater awareness and recognition of subsequent icing related events leading to focused investigation on engine power loss associated with ice particle icing.

Mason et al.[61] have formed a detailed hypothesis of the environment responsible for engine problems. Unlike the sub-freezing environment required for accretion of supercooled water drops for removal of the released latent heat, ice crystal icing can occur deeper in the

engine core where local airflow temperatures are significantly above freezing. A mixed phase condition results when the warm air melts some of the ice crystals ingested by the engine. The ice water mixture impinges on engine internal flow-path surfaces and lowers the blade temperatures. Ice particles become more likely to stick and accrete to these wetted surfaces. The subsequent shedding of this accreted ice can then result in operation abnormalities.

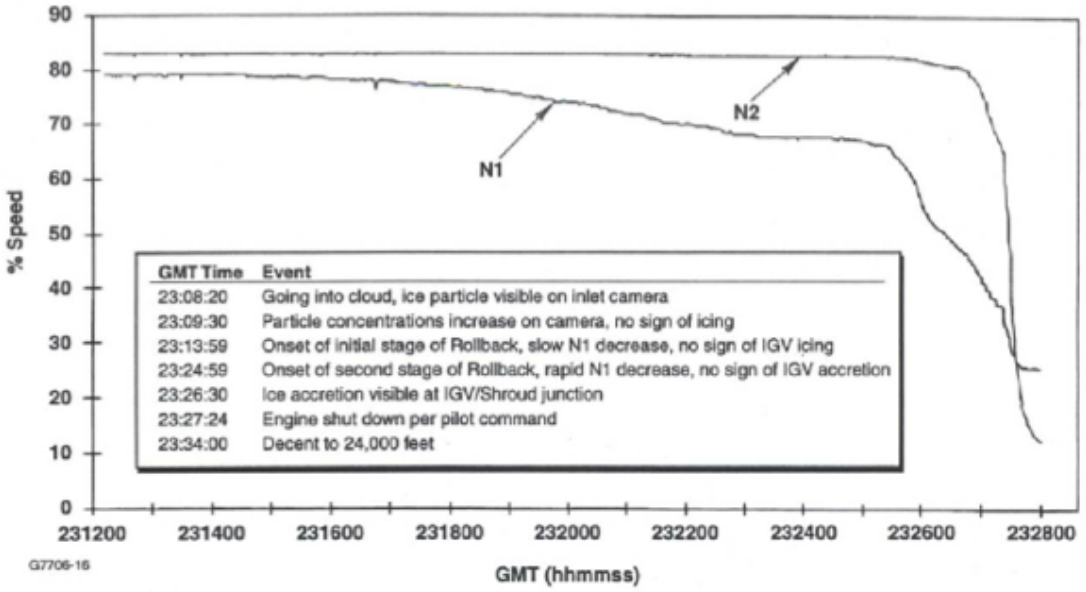

Figure 1: Test data demonstrating engine rollback in a convective cloud (Mason et al. [61])

Engine data from a flight test conducted in a HIWC cloud environment taken from Mason et al. [61] are presented in Fig. 1, where N1 and N2 are the fan and core speeds, respectively. The gradual decay of speeds without any visible ice formation on the fan and first stage compressor stator vanes was noted. Eventually, the speeds droped rapidly, indicating engine rollback. This implied formation of ice near the low speed compressor exit guide vanes with possible shedding into the high pressure compressor causing the engine rollback.

In explaining the mechanisms for engine power-loss, Mason et al. [61] have proposed the following three mechanisms of failure due to ice:

1. The engine can experience a compressor surge where the localized airflow separation

causes sudden flow reversal, followed by a decay in rotor speed as the engine stalls. This type of failure can occur due to the loss of energy of the compressor airflow to the ingested ice particles along with loss of efficiency of airfoils with accreted ice. As a result, the airflow to the combustor can drop, causing the exhaust gas temperature (EGT) to rise quickly.

2. A mixture of vapor and ice flow into the combustor can cause combustor flameout.

3. The impact by shed ice can cause damage to engine blades and vanes.

Rios and Cho [83], Veillard et al. [97] and Venkataramani et al. [98], have described previous attempts to model the ice accretion problem inside an engine core. Veres et al. [100] have determined the location of ice accretion inside the compressor of a high bypass ratio turbofan engine, based on the detection of freezing local wet bulb temperature and the local melt ratio above 10%. The melt ratio of 0% is an indication that the ice particle has not melted and 1% denotes complete melt of the ice particle. Hamed et al. [34] have developed a computational tool to simulate ice accretion on rotating blades in a 3-D unsteady flow in a compressor. The simulation strategy helped predict the droplet collection rate, ice growth and resulting distortion of the aerodynamic shape.

Mason et al.[58] have presented one of the first efforts to simulate the warm air/cold ice conditions occurring inside the engine core using a test rig. Test results demonstrated the formation of ice in mixed-phase conditions (liquid and ice) when the air and surface temperatures were held warmer than freezing.

Recent research at NASA Glenn Research Center's Propulsion Systems Laboratory (PSL) is focussed on the consequences of ice crystal ingestion and subsequent ice accretion at the fan and low pressure compressor blades. Addy and Veres [1] have provided an overview of the NASA Engine ice crystal icing research. The paper identified the research areas required to address the icing issue.

Jorgenson et al. [42] and May et al. [62] presented a proof-of-concept detection scheme for icing related engine rollback. Location and level of blockage due to ice accretion were identified in the low pressure compressor and fan core by utilizing an engine system modeling

code, along with a meanline compressor flow analysis. The Commercial Modular Aero-Propulsion System Simulation 40k (C-MAPSS40k) was used to find the control system response to resulting changes in the air and fuel flow. Additionally, an engine rollback was simulated when the ice accretion in the engine core increased beyond a certain threshold.

Joint experiments are also being carried out between NASA Glenn and National Research Council of Canada (NRC) in the NRC altitude chamber [20]. In 2010, testing occurred at the NRC Research Altitude Facility utilizing a single wedge-type airfoil in a wind tunnel designed to facilitate fundamental studies while retaining critical features of a compressor stator blade or guide vane. Subsequently, Jorgenson et al. [41] and Veres and Jorgenson [99] reported testing at the PSL altitude test facility at NASA Glenn, on a commercial turbofan engine that previously experienced icing related power loss in a high altitude ice crystal environment. The results confirmed ice accretion at the fan and LPC blades due to ice crystal ingestion. The PSL test data is used in combination with a computational tool to assess the risk of ice accretion. The tool consists of an engine system thermodynamic cycle code, compressor flow analysis code and an ice particle melt code to qualitatively simulate the energy loss due to ice flow through the compressor without an actual ice accretion model. Oliver [78] has documented the inaugural of the first full scale, high altitude ice crystal cloud turbofan engine test, conducted in a ground facility at PSL. Analysis of the PSL data showed that uncommanded reduction in thrust occured in an ice crystal cloud operation. A flow reversal was also recorded.

1.2.3 Atmospheric hail and ice detection and mitigation

When flights operate in hail conditions, hail may be undesirably ingested into the engine core. The presence of hail in turbofan engines, especially at low engine power operating conditions, such as idle descent, has been known to cause combustor flameouts and rollbacks. The detection methods for hail rely on parameters such as core speed, temperatures and pressure across the engine and fuel flow.

McDonald [63] tuned a hail ingestion simulation model to best match experimental data at idle power setting for a General Electric gas turbine engine. The fuel flow and engine

speed variation registered a decline towards engine rollback as a consequence of the control system response to hail.

Mouton [67] patented an anti-flameout safety system that prevents engine flameout for a gas turbine engine in the event of ingestion of hail and/or water through the engine intake. The method detected the change in the operating point by sensing the temperature change across the compressor. The signal generated is sent to the engine controller which increases the engine power output. In the event of heavy rain, liquid water can be present in the air exhausted from the high pressure compressor to the combustion chamber. The patent by Rowe [86] provides a unique method of compensating for water in a ducted fan engine. In case liquid water in air flows into the combustion system, the air temperature in the combustor lining tends towards the saturation temperature of water at the combustor operating pressure. Sensors detect this change, and a signal increases the fuel flow to the combustion system. This in turn increases the high pressure compressor shaft speed and aids evaporation.

Myers [70] outlined a method for controlling an aircraft engine using a control system that would enable its operation at low power while hail is ingested. This method makes use of blowout maps along with number of sensed inputs from the engine environmental operating conditions, such as measurements of fuel-air ratio that indicate the offset of compressor airflow pressure and temperature from dry reference values. Djelassi and Riou [26] proposed a method for detecting ingestion of water or hail in an engine by examining the compressor discharge temperature and fuel flow.

The growing number of engine ice crystal icing incidents has triggered recent changes in international certification requirements. Boeing and General Electric flight tested an upgrade to the GEnx-2B full-authority digital engine-control unit that will help the engine detect the presence of ice crystals when the aircraft is flying through a convective weather system. New algorithms were devised for scheduling variable bleed valves to open and eject ice crystals that may have built up in the area aft of the fan or in the flowpath to the core.

Califf and Knezevici [11] devised a detection parameter that scales on the concentration of water in the atmosphere and can be used to sense ice crystals encountered by flights

at high altitudes. This would aid in revising the certification regulations related to the icing envelope where engine abnormalities were witnessed. Also appropriate automated engine response schedules could be triggered. The detection parameter depends on the suppression of the high pressure compressor (HPC) discharge temperature due to energy loss to ice crystals.

To alleviate issues associated with hail ingestion, some engines include a variable bypass valve (VBV) system. VBV systems are designed to extract a substantial portion of hail ingested in an engine core and centrifuge it into the engine bypass stream. High bypass ratio engines have large frontal area making them susceptible to ice accretion on the booster inlet and booster stages during idle operation within an icing environment. Moreover, any accreted ice sheds during the acceleration, particularly at maximum power operation. Large engines have been reported to be at risk of compressor stall due to ice shedding. The booster operation can be controlled below the stall line by opening the VBV doors to extract ice along with booster flow overboard. Modern high bypass ratio engines consist of higher pressure core compressors and lower pressure boosters. Thus less pressure difference is produced between the booster exit and the fan bypass duct. This increases the difficulty to bleed sufficient amounts of air from downstream of the booster. Pritchard et al. [82] patented a VBV useful in preventing surge and easing ice removal from the duct in such high bypass ratio engines. However, in addition to being complex, such VBV systems may provide only limited benefits and may increase the overall assembly cost of the engine.

In the Aviation Week (Sept. 2013), Norris [76] reported that an international team comprising NASA, FAA, Environment Canada, Transport Canada, Airbus, Boeing, the U.S. National Center for Atmospheric Research and the Australian Bureau of Meteorology have come together forming the Engine Harmonization Working Group (EHWG) to conduct a HIWC test campaign. The goal is to research the phenomenon that causes core icing in convective regions, particularly in mid-latitude and tropical regions. The report claimed that the European Union's High Altitude Ice Crystals (HAIC) project would also contribute a specially configured Falcon 20 research aircraft to the effort.

The effort also builds on the European Aviation Safety Agency's (EASA) High Ice Water

Content program. The program used data collected on a series of flight-test campaigns conducted by Airbus in 2010 in the wake of the Air France 447 A330-200 accident in June 2009. The French air accident investigation agency, BEA, recommended as part of its safety recommendations in July 2012 that EASA "undertake studies to determine with appropriate precision the composition of cloud masses at high altitude," and based on these results, modify certification criteria for air data probes. The HIWC/HAIC campaigns are therefore intended to provide better understanding of glaciated icing conditions that could also affect air data probes.

The ice shed inside the compressor from the accreted ice is believed to be a direct cause of engine instability [60]. The research in this thesis addresses the impact of ice ingested inside the hot high pressure compressor zone. It is of interest to numerically simulate the interaction between the airflow and ingested ice and to study the mechanism of induced stall on the engine compressor.

1.2.4 Compressor operation, map and stability

Axial compressors are considered in this study. A typical compressor map for an axial compressor shows pressure ratio as a function of inlet volumetric flow or mass flow for a range of compressor speeds. This compressor map indicates that there are limits on the operating range of such a compressor. The characteristics have a range of operating points from the largest mass flow rate where choking can occur, to the other extreme of small mass flow found at the surge line (Boyce [9]).

A compressor's stability is a measure of its ability to recover from disturbances that alter the compressor operation about an operational equilibrium point [73]. If the disturbances drive the compressor away from the original point, the system is unstable. For the purpose of validating the compressor operation, the mass flow rate is reduced/throttled until eventual breakdown of stable flow operations occurs. This aids in finding the stable operating range. A determination of this stable range is important since the engine operation at off-design speeds may occur close to surge or choke depending on its operating condition.

The static stability of a compression system depends on the characteristic of both the

compressor and the downstream throttle condition. Greitzer et al. [33] and Cumpsty [19] describe a static stability criterion in terms of the compressor and throttle characteristic curves, Ψ_C and Ψ_T.

The throttle characteristic is given by $\Psi_T = \frac{\Delta p_{throttle}}{\frac{1}{2}\rho_c U^2_{meanline}}$. According to the criterion, the system is statically unstable if,

$$\Psi_C > \Psi_T$$

Since the compressor and throttle curves are both steady-state functions, this instability criterion can be checked at one steady state or a succession of steady states without knowledge of the system dynamics; hence the name, static instability.

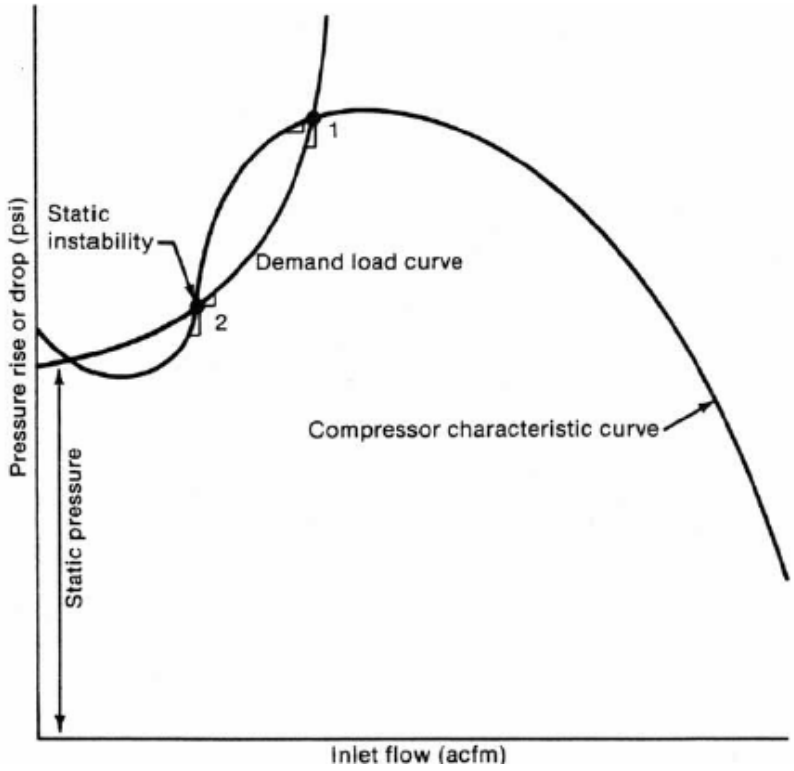

Figure 2: Static stability from compressor and throttle characteristic curves

The compressor stable operation on the characteristic curves supplied by the compressor manufacturer is generally on the negative sloped region (right hand side of the map). The negative slope causes the pressure to change in the opposite direction of a change in flow resulting in a stabilizing effect. Figure 2 shows the operation on the left side of the zero slope

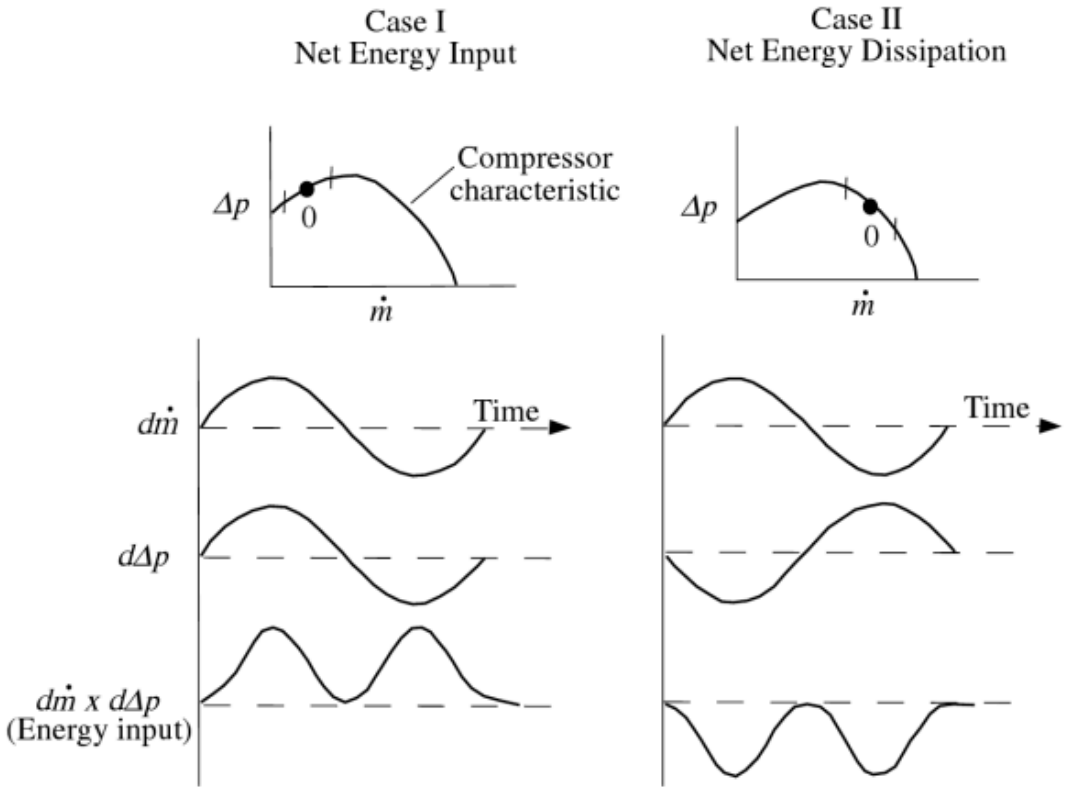

Figure 3: Compressor dynamic stability criteria (Greitzer et al. [33]).

on the compressor map. From the stability criterion it can be deduced that the compressor operation is statically unstable at operating point 2, where the compressor curve slope is steeper than the throttle curve slope. At operating point 2, the pressure imbalance by the throttle (rise or drop) gets exacerbated and the operating point moves away from the initial condition making the system unstable.

Considering a dynamic instability encountered by the compressor that makes it unstable as increasing energy is pumped into the system. Figure 3 is an illustration of the unsteady response of the compressor showing the mechanism that causes dynamic instability. The point 0 on the compressor characteristic denotes the equilibrium operating condition. The vertical lines indicate the nominal oscillation amplitude. It is evident that the operation on the left side of the schematic is positively damped where the transient mass flow rate and pressure add together resulting in an unstable response.

The limit for low flow or high pressure ratio operation is set by a rapid flow instability

known as surge. Prior to reaching a surge event, a number of other aerodynamic flow instabilities are likely to occur within an axial compressor. Local stall is result of a very low momentum flow zone created in a blocked zone. Consequently the low momentum flow results in high-pressure loss. The quasi-one dimensional unsteady solver in the present research captures the inception of stall observed as a fluctuating flow behavior when any particular blade row is no longer able to meet its full pressure ratio characteristic. Such flow oscillations that rapidly progress through the compressor cause the compressor surge instability.

1.2.5 Performance comparison at low and high speed compressor operation

For an engine compressor where the annulus is not parallel and compressibility effects are important, the flow ratio for consecutive stages vary. Depending on the speed of rotation of the engine, the stages experience different loading conditions prior to becoming unstable. To proceed, it is important to check the fidelity of the numerical solver for both low and high speed operation of the compressor. The transient analysis is expected to replicate steady state values of the flow variables across the compressor in the absence of any dynamic events and the initial transients in the simulation are expected to decay.

Day and Freeman [21] have offered insight into the unstable behavior of a compression system at low and high speed compressors. At low speeds the air entering the compressor at the front stages is compressed to a lesser extent. This causes the rear stages to receive air at a higher than design $V_x/U_{meanline}$, pushing away the operating point at the rear stages away from stall. At high speed operation, the air entering the front stages get compressed with higher effectiveness causing the rear stages to receive air at a lower than design flow ratio, $V_x/U_{meanline}$. Thus, the rear stages for high speed compressors move closer to stall. This shift of stage loading at different operating speeds is described by Fig. 4. The position of the stage that is most heavily loaded is most likely to cause stall shift from the front to the rear of the compressor as the speed goes up.

The meanline or pitchline velocity across the compressor is the rotor blade velocity at the mean radius position (see Eq. 50) . The stage flow coefficient is calculated as the ratio

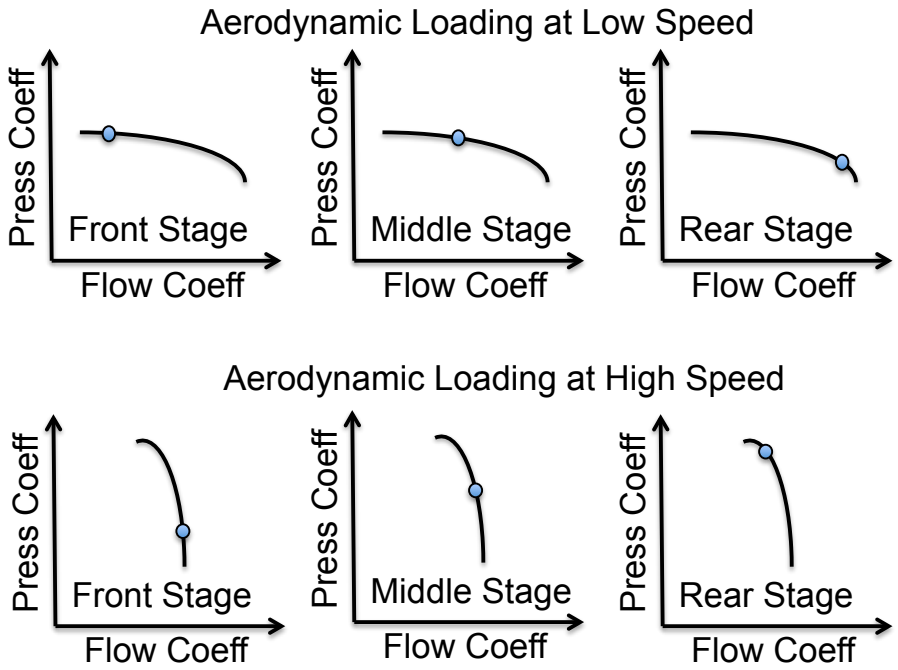

Figure 4: Axial compressor stage matching (adapted from Day and Freeman [21]).

between the axial component of velocity and the meanline velocity.

$$\phi = \frac{u}{U_{\text{meanline}}}$$

The pressure coefficient across a blade control volume is given by the rise in pressure.

$$\text{Press Coeff} = \frac{\Delta p}{\frac{1}{2}\rho_c U^2_{\text{meanline}}}$$

Aerodynamic loading as given by Fig. 4 illustrates the stage matching of an axial multistage compressor at various operating loads [102]. In a well-designed axial compressor system at low speed operations, the front stages of the compressor are designed to operate near the stability limit while the back stages operate near the choking point. At high speed operation of the axial compressor the rear operates near the stability limit while the front is matched near choke [15].

1.2.6 A comparison of ice ingestion effects with wet compression

A parallel can be drawn between the response of flow to ice and that of the wet compression performance used for gas turbine inlet air cooling. There has been considerable research to

better understand the fogging technology that encompasses three techniques depending on the injected water amount and injection position namely, (1) Inlet fogging (also called high pressure fogging), (2) overspray (or wet compression) and (3) interstage injection. During fog cooling, water is atomized to micro-scaled droplets and sprayed in the inlet airflow. Overspray involves additional water droplets that remain in the compressor even after the airflow reaches saturation at the wet bulb temperature. Studies related to inlet fogging and wet compression have shown its wide applicability in power and efficiency augmentation of gas turbine engines attributed to thermodynamic effects [7, 8, 13, 91]. The main research of the complex phenomenon involving multiphase flow during compression were developed by Bagnoli et al. [3], Hartel and Pfeiffer [35], Horlock [38] and White and Meacock [64]. They describe the usage of wet compression to decrease the compressor specific work and discharge temperature, depending on its polytropic efficiency, and to increase the compressor pressure ratio and mass flow rate.

A vital aspect of performance impact with ingested ice that is analogous to wet compression is the shift in operating point with increasing water injection rates. Water evaporation through the compressor changes its operating point on the performance maps, with a redistribution of load among the different compressor stages. White and Meacock [104] explain the mechanism that accounts for rematching of the stages, with the front stages moving towards a choke condition and rear stages towards stall. Due to operability concerns, a similar analysis is required for ice shed into the compressor to capture aero-thermodynamic and mechanical effects resulting in a redistribution of the stage load.

Utamura et al. [96] and Zheng et al. [109] have discussed the influence of parameters such as injected water droplet diameter, the evaporation rate and injected water mass flow rate on the wet compression efficiency. Bianchi [8] analyzed and discussed the effects of wet compression on an existing GE Frame 7EA gas turbine performance. The thermodynamics involving evaporation plays a role for fine droplet fogging application while the mechanical and aerodynamic effects are significant for large droplet related to rain ingestion in gas turbine. The thermal, aerodynamic and mechanical effects of wet compression were studied by Nikolaidis and Pilidis[74]. In case of water ingestion, the effects of any evaporation

may be diminished by the aerodynamic and mechanical consequences. A similar analysis is carried out in this thesis in order to examine the thermodynamic, aerodynamic and the mechanical effects of ice ingestion in the compressor.

The advisory Group for Aerospace Research and Development (AGARD) of the North Atlantic Treaty Organization [30] and Brun et al.[10] discuss the influence of rain, snow and hail on the performance and operability of gas turbine engines. In Fig. 5, the onset of aerodynamic compressor instabilities, such as rotating stall and surge that can result from the usage of evaporative cooling power augmentation technologies in gas turbines, is analyzed. According to the report the compressor undergoes a loss in surge margin due to the increased operating line in the presence of hail or snow. The stable operation of a compressor is limited by the surge line. Rain ingestion in adverse weather conditions has a performance degradation effect due to aerodynamic and mechanical effects [22]. A similar investigation of the impact of ice ingestion on the stall limit of the compressor is carried out in this thesis.

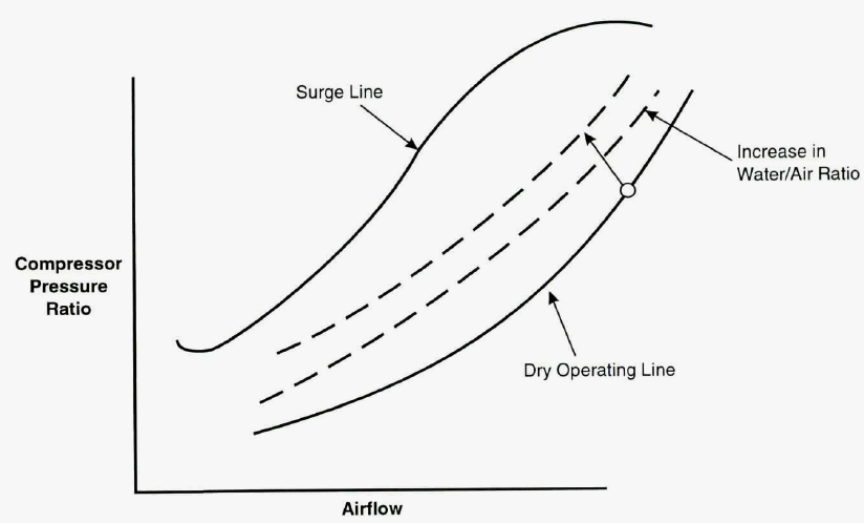

Figure 5: High pressure compressor surge (AGARD [30]).

1.2.7 Computational simulation of flow through engine

The mathematical models and numerical simulations of flow through engines have been classified into three major categories depending on the engine operational regime: (i) on-design and off-design steady-state engine operation conditions, (ii) transient operation of

the gas turbine engine, and (iii) dynamic events such as compressor surge. The modeling of the fluid and thermal phenomena of transient response to ice ingestion involves analysis of the complex transport processes associated with a coupled dispersed phase flow system. The first step towards this analysis is the development of a multistage, axial compressor flow simulation tool.

The compressor is a critical component of a gas turbine engine regarding its operation and its response to any changing operating conditions. Flow non-uniformities conveyed through the engine intake can severely affect the compressor overall performance and operational stability. Therefore a compressor flow simulation model is necessary to predict its response throughout the operational envelope for all possible inlet conditions and throttle schedules.

To date, there have been many different approaches to this problem, all of which can be categorized into the following three methods: one-dimensional mean-line methods, two-dimensional throughflow methods(Shu [37]) and three-dimensional computational fluid dynamics (CFD) methods (Chima [14] and Wu [107]). In most cases, quasi-one-dimensional, two-dimensional and three-dimensional models [40] have been employed as an amalgamation of the above methods. Based on complexity of the flow captured, the methods are classified as Reynolds Average Navier Stokes (RANS), Euler-based or potential flow solvers. In the present work, a quasi-one-dimensional Euler-based flow solver is considered.

Euler or RANS 3-D based methods are far too computationally intensive to be useful as fast assessment tools. A multistage compressor simulation demonstrates several geometry and convergence handling problems with one blade row immediately followed by a second one (rotor stator pair). Consequently the 3-D flow profile present at the compressor inlet plane has to be decomposed to radial and circumferential components. The former is treated with the streamline curvature method based tool and the later is treated with a multiparallel compressor method based tool. Most throughflow codes use the streamline curvature method and derive from those of Denton [23], Novak [77] and Smith [90]. The streamline curvature algorithms were avoided, because of their restricted field of application in handling stalled or reversed flows [12]. On the other hand, over-simplified models do not

offer the versatility of finite-volume solvers. Analytical and lumped-volume 0-D models [95] may simulate a wide range of operating conditions but they are more suited for preliminary low fidelity-low computational load analysis where qualitative assessment is of primary interest.

Garrard [29] constructed the Aerodynamic Turbine Engine Code (ATEC) that simulated the operation of a gas turbine engine using a one-dimensional, time dependent aerothermodynamic mathematical model. Time-dependent Euler equations in the conservation form with turbomachinery source terms were solved by both implicit and explicit equation solvers. ATEC can also be used to address dynamic events such as compressor stall or steady state processes to model both on and off-design engine operation.

The solver in the present study is based on the unsteady quasi-one-dimensional representation of the compressor flow path as described by Dhingra et al. [25]. A similar analysis is also described by Olivier et al. [79]. Their paper uses a row-by-row, with a mean-line performance prediction scheme. Velocity triangles at mid-span are determined with the help of empirical correlations to provide the source terms associated with the blade rows. A subsequent work by [27] dwells in the post-stall behavior that can be predicted by the quasi-one dimensional model.

1.3 Thesis Objectives

The previous subsections, 1.2.2 and 1.2.3, emphasize the present concern related to core engine icing. The fan and low pressure compressor (LPC) ice accretion mechanism has been extensively investigated in terms of experiments and computational studies since its recognition as a mechanism to engine failure. However, an initiative to understand the transient response of the high pressure compressor (HPC) flow to ice ingestion is lacking. Past investigations have found damaged HPC blades due to ice ingestion. Also, past flight events of compressor surge/stall and/or combustor flameout from ice ingestion have been documented. Moreover, flight test data supports the theory that ice builds up in the engine core and sheds downstream (Mason et al. [61]) causing stall/surge events. These findings highlight the significance of the analysis of impact of ice ingestion on flow through the

HPC as carried out in this thesis. The computer simulation of the rapid response of the flow pressure changes due to ingestion of ice is important in order to develop an in-depth understanding of the dynamic behavior during engine icing events.

Although the complex flow field in the multistage compressor requires a three-dimensional computational fluid dynamics analysis for accurate representation, a one dimensional analysis is proposed in order to circumvent large computational costs associated with the following analysis requirements:

1. Model the transient flow of humid air and discrete particles through the compressor.
2. Account for thermodynamic properties of air like pressure, temperature, humidity, physical and thermodynamic characteristics of ice (discrete phase gas property, mass, temperature) in order to evaluate the dynamic process involving heat and mass transfer between humid air and ice.
3. Implement a blade row-by-row analysis of the flow field in the compressor.
4. Achieve two-way interaction of the flow field by coupling the discrete phase model at each time step of the simulation.
5. Demonstrate the flexibility of obtaining performance data at various compressor speeds.
6. Analyze the redistribution of stage loading due to icing.
7. Determine the sensitivity of the developed simulation model to semi-empirical models, assumptions and inputs variables.
8. Validate the existing dry air compressor flow model that has formed the base for building the ice ingestion simulations carried out in this thesis.
9. Verify the change in compressor performance and operability due to the ice ingestion by a comparison with the wet compression process.

CHAPTER II

NUMERICAL MODEL

2.1 Model Setup

2.1.1 Geometry

The compression system examined under icing conditions in the present work is representative of a typical laboratory or rig-test setup. Dhingra et al. [25] have used such a set up in their studies for the identification of a stalling stage in a multistage compression system during rapid transients. A schematic of the system under consideration is presented in Fig. 6. The compressor is assumed to be externally driven and hence operating at a constant rotational speed. A throttle valve downstream of the plenum, modeled as a variable area choked orifice, sets the nominal operating point of the system. The basic element of the compressor is the blade row consisting of a rotor and a stator.

2.1.2 Ice Ingestion

The total ice flow rate ($\dot{M}_p$) entering into the compressor free stream is specified. A distribution of ice particle diameters in the ice flow is assumed. The number of ice crystals (N_p) corresponding to each particle diameter confirms to a Rosin-Rammler distribution $\tilde{f}_m$ [68] that dictates the fraction of the particle mass m_p having diameter D_p.

$$N_p(D_p) = \frac{\tilde{f}_m \dot{M}_p}{m_p(D_p)} \Delta t \tag{1}$$

where Δt is the time required for the particle to traverse computational length, Δx. The initial number of particles N_p in each packet of discrete particles associated with a certain diameter remains unchanged through the stages until complete evaporation. $\tilde{f}_m$ is the fraction of the particle mass, m_p, associated with diameter, D_p.

2.1.3 Bleed mass

Bleed air from a compressor operating at high pressure constitutes 3-5% of the air system for cabin air conditioning, engine inlet anti-ice and the cooling of high temperature components

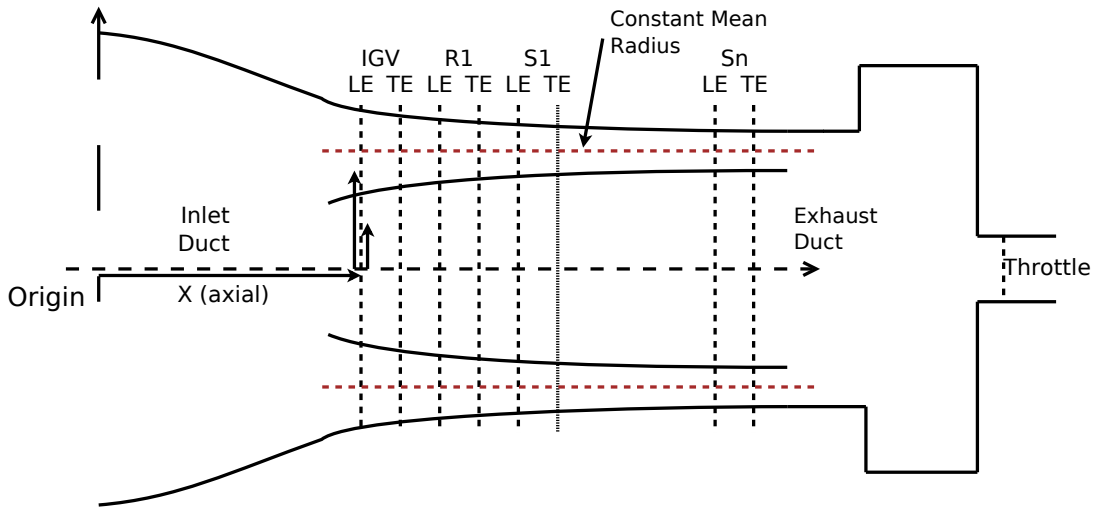

Figure 6: A schematic of a basic compression system test rig (Dhingra et al. [25]).

[108]. Wellborn [103] observed that bleeding at the blade leading edge and trailing edge can increase the compressor efficiency. Leishman and Cumpsty [53] performed a series of studies on the mechanisms of air bleeding in a blade passage. They inferred that the interaction between the bleeding and the primary passage flow was basically an inviscid and pressure-driven phenomenon which largely depended on the rate and the air extraction location.

In the present work, the ten stage compressor flow model has bleed mass flow rate aft of the 4th stage control volume and again aft of the 7th stage control volume. The bleed mass flow rate $\dot{m}_b$ is calculated as a function of the gas pressure p_g and gas temperature T_g to account for transient effect on the amount of bleed.

$$\dot{m}_b = \frac{k_b \ p_g}{\sqrt{T_g}} \tag{2}$$

where, k_b is the bleed mass coefficient that is specified. p_g and T_g are the gas pressure and temperature, respectively.

2.2 Continuous Phase Model

The modeling approach treats the air-water vapor mixture as a "continuous phase" and the ice particles/ water droplets form a separate "discrete" phase. This section describes the continuous phase model.

A quasi-one-dimensional axisymmetric unsteady numerical simulation model of the flow in the compression system is developed in which flow variations in the axial direction are considered but the variations in the cross-stream direction are neglected. The flow-path area A is a function of the axial coordinate $A = A(x)$.

In the present treatment, the flow is assumed to be inviscid, unsteady and compressible. With the stated assumptions, the general three-dimensional Navier Stokes equations reduce to a one-dimensional axisymmetric Euler system of equations with source terms.

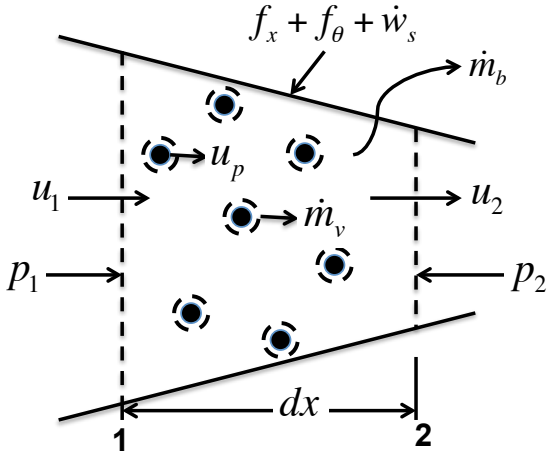

Figure 7: Quasi-one-dimensional control volume with dispersed phase elements (adapted from Crowe et al. [16])

The computational methodology involves the solution of the transport equations for the continuous phase (air) that contain additional volumetric mass source and heat sink terms due to the existence of the discrete phase. The control volume used for the quasi-one-dimensional flow is shown in Fig. 7. $\dot{m}_b$ denotes the bleed mass flow rate leaving the volume, whereas $\dot{m}_v$ is the vapor added to the volume. f_x and f_θ are the blade axial and circumferential forces, respectively applied on the airflow. $\dot{w}_s$ is related to shaft work in the form of enthalpy added due to rotation of the blades. The coefficients are calculated for

both rotor and stator blades. The elemental volume dV has infinitesimal length dx, leading to the expression:

$$dV = A(x)dx \tag{3}$$

Blockage effect: The effective area of the compressor section gets blocked by ice flow. The numerical scheme employed accounts for this blockage. Crowe et al. [16] have shown that if there are a total of N_p discrete particles of radius r_p intersecting the compressor area A then the blockage area, A_b is given by,

$$A_b = \frac{2\pi}{3} N_p r_p^2$$

The dispersed phase volume fraction, α_d and the corresponding continuous phase volume fraction, α_c are,

$$\alpha_d = \frac{A_b}{A} \qquad \alpha_c = 1 - \alpha_d$$

Thus the mass flow rate $\dot{m}$ of the continuous phase through a cloud of discrete phase elements can be expressed as,

$$\dot{m} = \rho_c u \left(\alpha_c A\right)$$

$$\dot{m} = \rho_c u A_c$$

The area in the continuous phase calculations is A_c, that has the blockage included. With eventual evaporation of the ice, $\dot{m}$ represents the mass of humid air. ρ_c is density of humid air.

2.2.1 Governing Equations: Continuity

The continuity equation expounds that the rate of change of mass in the control volume is balanced by the net efflux of mass through the control surface.

$$\frac{\partial \left(\rho_c A_c\right)}{\partial t} + \frac{\partial \left(\rho_c A_c u\right)}{\partial x} = -A_c s_{mass} \tag{4}$$

The mass source term s_{mass}, in mass conservation equation appear from the bleed mass and the discrete phase. The source term from the bleed mass, $\dot{m}_b$ per unit volume given by

Eq. 2, can be expressed as,

$$s_{\text{bleed}} = \frac{\dot{m}_b}{dV} \tag{5}$$

It should be noted that evaporation of the discrete phase will result in mass flow into the continuous phase (influx), s_{vapor}, as computed by the mass transport equation of the discrete phase model in Section 2.7, Eq. 33.

The continuity equation can be rewritten by dividing by the areas as,

$$\frac{\partial}{\partial t}\left(\rho_c\right) + \frac{\partial}{\partial x}\left(\rho_c u\right) = s_{\text{vapor}} - s_{\text{bleed}} \tag{6}$$

2.2.2 Governing Equations: Axial momentum equation

The momentum balance in the x-direction can be written as,

$$\frac{\partial}{\partial t}\left(\rho_c u A_c\right) + \frac{\partial}{\partial x}\left((p_g + \rho_c u^2)A_c\right) = p_g \frac{dA_c}{dx} + A_c f_x - A_c u s_{mass} \tag{7}$$

Source terms from the continuous phase

1. $p\dfrac{dA_c}{dx}$ term arises from the quasi-one-dimensional axisymmetric assumption that accounts for an area change in the x-direction.

2. f_x is the blade force per unit volume acting on the continuous phase that represents the pressure rise of the fluid across the rotor and stator blade rows, axially. The blade force is interpreted from a given axial stage pressure coefficient map detailed in section 2.3.

3. Momentum loss due to bleed of air flowing with axial velocity u per unit volume, is given by: $u s_{\text{bleed}}$.

Source terms from the discrete phase

The discrete phase influence on per unit volume of the gas given by s_{mom}, is detailed in the Section 2.7, Eq. 34.

Summing the contribution from all the source terms and dividing by the compressor area, the momentum balance in Eq. 7 simplifies to

$$\frac{\partial}{\partial t}\left(\rho_c u\right) + \frac{\partial}{\partial x}\left(p_g + \rho_c u^2\right) = \frac{1}{A_c} p_g \frac{dA_c}{dx} + f_x - u\, s_{\text{bleed}} + s_{mom} \tag{8}$$

The momentum loss due to wall friction and gravity forces are neglected in Eq. 8.

2.2.3 Governing Equations: Circumferential momentum equation

The circumferential momentum equation is obtained by assuming a constant meanline radius, r_m across the control volume (Fig. 7).

$$\frac{\partial}{\partial t}\left(\rho_c v_\theta\right) + \frac{\partial}{\partial x}\left(\rho_c u v_\theta\right) = f_\theta - v_\theta s_{\text{bleed}} \tag{9}$$

where, f_θ is the circumferential blade force per unit volume that accounts for the increase in energy across the blades due to the circumferential velocity v_θ for a quasi-one-dimensional axisymmetric flow. It is interpolated from the stage map for the turning force coefficient.

2.2.4 Governing Equations: Energy equation

The first law of thermodynamics states that the rate of change of energy in a control volume plus the net efflux of energy though the control surface is equal to the net heat transfer to the system minus the rate at which work is done on the system. The energies consist of the internal and kinetic energy. The compressor work done arises as an enthalpy change.

The energy balance is expressed as (Crowe et al. [16]),

$$\frac{\partial}{\partial t}\left[\rho_c A_c\left(e_c + \frac{u^2+v_\theta^2}{2}\right)\right] + \frac{\partial}{\partial x}\left[\rho_c u A_c (h_c + \frac{u^2+v_\theta^2}{2})\right] = -A_c h_0 s_{mass} + \frac{1}{dx}\left(\dot{Q} - \dot{W}\right) \tag{10}$$

Here, $h_c = e_c + p_g/\rho_c$, where e_c is the specific internal energy of the continuous phase. The total enthalpy h_0 is given by, $h_0 = h_c + \dfrac{u^2+v_\theta^2}{2}$.

Source terms from the continuous phase

1. The change in enthalpy through a control volume (Fig. 7) due to the work done by the blades on the air is reflected in the shaft power per unit volume, $\dot{w}_s$. This is interpolated from the compressor characteristic map of work coefficient versus flow coefficient as described in section 2.3.

2. The enthalpy loss due to bleed mass can be expressed as, $\dot{m}_b\left(h_c + \dfrac{u^2+v_\theta^2}{2}\right)$,

Source terms from the discrete phase

The discrete phase influence on per unit volume of the gas given by s_{energy}, is detailed in the Section 2.7, Eq. 35.

Rewriting the Eq. 10 with the definitions of s_{bleed} and dividing by the control volume yields the following energy equation

$$\frac{\partial}{\partial t}\left[\rho_c(e_c + \frac{u^2+v_\theta^2}{2})\right] + \frac{\partial}{\partial x}\left[\rho_c u(h_c + \frac{u^2+v_\theta^2}{2})\right] = \dot{w}_s - s_{\text{bleed}}\left(h_c + \frac{u^2+v_\theta^2}{2}\right) + s_{\text{energy}} \tag{11}$$

It is assumed that there are no radiation losses or friction losses at the walls. The work done by gravity forces are neglected.

2.3 Modeling of compressor blade row source terms

The continuous phase model of the airflow through the compressor consists of blade force source terms that represent the blade's energy interaction with the working fluid. The axial momentum exchange in Eq. 8 is through pressure coefficient ψ_{fx}. The circumferential momentum exchange is through $\psi_{f\theta}$ in Eq. 9 and the work coefficient $\dot{w}_s$ in Eq. 11 communicates the change in total enthalpy of the fluid due to the blades. The correct evaluation of these source terms is imperative for accurately capturing the observed compression system behavior [25].

The compressor system is modeled by control volumes. Acting on the control volume is a body force, f per unit volume, attributable to the effects of the compressor blades (Fig. 8). To provide these stage forces and shaft work inputs to the momentum and energy equations, a set of quasi-steady stage characteristics must be available for closure.

2.3.1 Evaluation of source terms

The compressor maps are constructed by the application of steady state force balance to a control volume as illustrated in Fig. 8, along with the flow continuity equation. Dhingra et al. [25] have derived the coefficients by balance of forces on the control volume.

The flow coefficient ϕ is expressed as a ratio of the axial gas velocity u, and the compressor meanline velocity U_{meanline}.

$$\phi = \frac{u}{U_{\text{meanline}}} \tag{12}$$

Depending on the flow coefficient ϕ computed at every blade row, a unique value of the force coefficient can be interpolated from the maps.

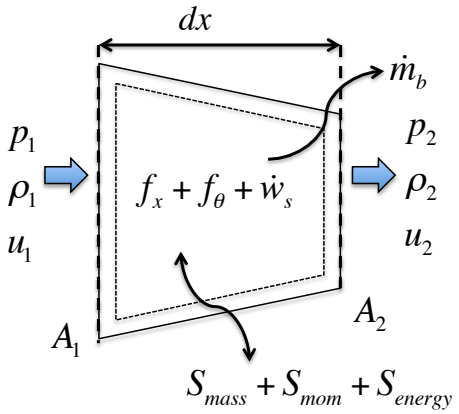

Figure 8: Application of conservation equation on an elemental control volume

Applying force balance in the x-direction across the control volume of length dx (Fig. 8) and implementing mass continuity, leads to,

$$f_x \frac{A_1 + A_2}{2} dx = \left(p_2 A_2 - p_1 A_1\right) + \left(\rho_2 u_2^2 A_2 - \rho_1 u_1^2 A_1\right) - \frac{p_1 + p_2}{2}\left(A_2 - A_1\right)$$
$$= \left(p_2 - p_1\right)\frac{A_1 + A_2}{2} + \dot{m}\left(u_2 - u_1\right)$$

The steady state axial body force coefficient, ψ_{fx} is then expressed as:

$$\begin{aligned}\psi_{f_x} dx &:= \frac{f_x dx}{\frac{1}{2}\rho_c U^2_{\text{meanline}}} \\ &= \frac{p_2 - p_1}{\frac{1}{2}\rho_c U^2_{\text{meanline}}} + \frac{\dot{m}\left(u_2 - u_1\right)}{\frac{1}{2}\rho_c U^2_{\text{meanline}}\left(A_1 + A_2\right)/2} \\ &= \frac{p_2 - p_1}{\frac{1}{2}\rho_c U^2_{\text{meanline}}} + 2\phi_1 \frac{2A_1}{A_1 + A_2}\left(\phi_2 - \phi_1\right)\end{aligned} \tag{13}$$

ψ_{fx} can be interpreted as the total pressure rise of the gas in the x-direction.

Applying force balance in the circumferential direction across the control volume of length dx (Fig. 8) and implementing mass continuity, leads to

$$f_\theta \frac{A_1 + A_2}{2} dx = \left(\rho_2 u_2 A_2 v_{\theta 2} - \rho_1 u_1 A_1 v_{\theta 1}\right)$$
$$= \dot{m}\left(v_{\theta 2} - v_{\theta 1}\right)$$

For a constant mean radius, the circumferential force coefficient ψ_{f_θ} is expressed as,

$$\begin{aligned}\psi_{f_\theta} dx &:= \frac{f_\theta dx}{\frac{1}{2}\rho_c U^2_{\text{meanline}}} \\ &= 2\phi_1 \frac{2A_1}{A_1 + A_2}\left(\phi_2 \tan\alpha_2 - \phi_1 \tan\alpha_1\right)\end{aligned} \tag{14}$$

where, α is the absolute angle given by $\alpha = \tan^{-1}\left(\frac{v_\theta}{u}\right)$.

Finally, the enthalpy change across a control volume of the compressor is represented by shaft power per unit volume, $\dot{w}_s$. A consideration of steady state energy balance yields,

$$\dot{w}_s dx := \dot{m}\frac{2}{A_1 + A_2}\Delta h_0 \tag{15}$$

Characteristic maps consist of the steady state values of blade force coefficients, axial, ψ_{fx} and circumferential, $\psi_{f\theta}$ and the shaft work per volume, $\dot{w}_s$ over a range of flow coefficients, ϕ.

2.3.2 Lagged blade force

The characteristic maps provide an instantaneous response to the unsteady flow rate as given in the previous section. Realistically, the body force on the flow through the blade control volume is lagged. A first order lag model connects the unsteady performance of the compressor blade row to its steady counterpart [25].

$$\tau\frac{dF}{dt} + F = F_s(\phi) \tag{16}$$

where,

ϕ : local, unsteady axial velocity coefficient of the compressor

F_s: steady performance of the blade row given by Eqs. (13) - (15)

F: instantaneous value of the flow field quantity

τ: time constant

The time lag constant through a physical control volume of length Δx with airflow having axial velocity u at the inlet is given as,

$$\tau = \tau_{amp}\frac{\Delta x}{u} \tag{17}$$

$$\tau\prime = \tau/\Delta t \tag{18}$$

The unsteady force and work terms at time instant $n+1$, can be derived as

$$F^{n+1} = \frac{(F_s^n + \tau\prime F^n)}{1 + \tau\prime} \tag{19}$$

For a high speed operation, an amplifying factor of $\tau_{amp} = 100$ for the first rotor is chosen. Else, $\tau_{amp} = 1$ for remaining blade rows and low speed operation. First stage pressure rise characteristic for a high speed operation shows a steep slope, indicating a large pressure rise with flow rate as compared to the pressure rise characteristic of the consequent stages. Thus τ_{amp} is a heuristic parameter dependent on the numerical model chosen in the present study that offers sufficient acoustic attenuation of the flow at the first stage, at high speeds.

According to Csanady [17], the mixture composition has negligible effect on stage characteristics; thus the stage characteristics are assumed to be unchanged due to vapor presence. The stage characteristics are also assumed to remain unaffected by ice or water in the present study.

2.4 Importance of modeling the discrete phase

Equations (6), (8) and (11) aid in assessing the importance of a discrete phase model. Ice ingested in the compressor results in rapid changes in the temperature and pressure of the air. The increase of the air temperature due to the compression process is contrasted by the cooling effect of water droplet evaporation. Moreover, evaporation changes the thermodynamic conditions of the air through the compressor, which in turn influences the thermal exchange with discrete particles. For example, the increase of temperature and pressure influences the saturation capacity of the air and then the droplet evaporation process. This coupled phenomenon is a continuous process which occurs along the whole compressor until complete evaporation of the ingested ice.

The concentration of discrete phase elements, ice crystals and water droplets, at a particular location at any given time in the compressor can be determined from a momentum transport equation of the discrete phase which is governed by the drag force, F_D on the discrete element. In turn, F_D is reflected as momentum and energy losses in the continuous phase.

The ingested ice melts and eventually evaporates. The phenomenon of phase change needs to be modeled via a mass transport equation which determines the concentration of

vapor in the compressor, s_{vapor}. This term appears as a source in the continuous phase formulations. An energy transport equation of the discrete phase is essential to model the exchange of heat energy $\dot{Q}_p$ from the airflow to heat the ice crystals and water droplets and also capture the melting and evaporation of the discrete elements through absorption of latent energy.

2.5 Discrete phase model

A discrete phase model of the heat and mass transfer process accompanying the ingestion of ice particles in the compressor is described.

The discrete phase is considered in a Lagrangian reference frame. A Lagrangian approach allows one to account for the instantaneous flow properties encountered by the particles, and thus involves each particle history starting from its injection into the flow field. Moreover, the evolution of particle diameter can be readily introduced in a Lagrangian approach. A few basic assumptions are listed.

1. The ice particles are in the shape of a sphere.
2. The radiation from the ambient air to the ice particles is ignored.
3. The heat transfer to the blade or wall surfaces is neglected.
4. The casing and any associated interactions with it are not modeled in the present study.
5. The ice accretion on blade surfaces and ice agglomeration is neglected.
6. The temperature remains constant across the ice particle at any instant of time (lumped capacitance method).
7. Ice particles entering the compressor are divided into groups depending on their initial diameters. The Rosin-Rammler distribution decides the number of particles in each group. A group property and the individual particle property are used interchangeably in this work.

Additionally there are no interactions among water droplets resulting in coalescence (Bagnoli et al. [3]). The discrete phase model considers the impact of particles on the compressor blades, however it neglects the phenomenon of water film formation on the compressor blade. This phenomenon can play a role for bigger sized droplets, however for less than 10-15 microns it is less important (Bhargava et al. [7]). The water droplet diameters splashed from a melting ice particle is smaller than this range and thus the assumption holds.

2.5.1 Particle fragmentation and splash semi-empirical models

It is inevitable that water droplets and ice crystals will collide with the blades throughout the compressor. It is computationally infeasible to solve the complete Navier-Stokes equations for each droplet-surface collision in a reasonable time frame. Thus empirical or semi-empirical models are sought to predict the effect.

For the model employed here, the basic assumptions related to the discrete particle encounter with rotor blades are listed,

1. All discrete particles break and splash on impact when they enter a rotating blade row.

2. The spherical structure of the particle is maintained after it breaks up.

3. The ice core loses any water film when it enters a rotating blade row, after a critical mass of the water shell is reached.

4. An ice particle sublimates to vapor below a critical ice crystal diameter.

Figure 9 demonstrates the secondary size after fragmentation due to a collision with a rotor blade. Ten different sizes of incoming ice crystals are considered in the present study. The sizes are normalized with the mean diameter of the spread. The computational solver applies a particle fragmentation model that is a function of the incoming diameter (Dhingra et al. [24]). The number of particles are updated accordingly to preserve the total volume before and after impact. A droplet breakup occurs rapidly compared to the trajectory time step. Thus the breakup is considered to be instantaneous (Wright and Potapczuk [106]).

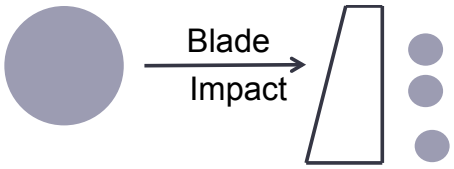

(a) Schematic of fragmentation of ice crystals and splash of water droplets

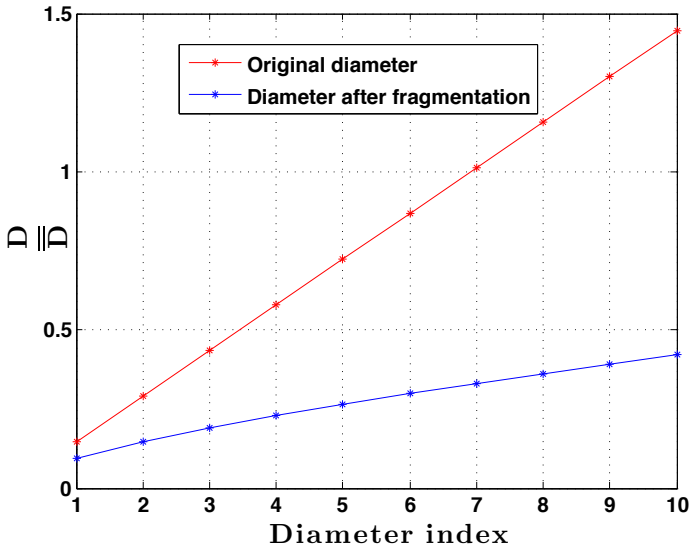

(b) Particle diameter before and after fragmentation

Figure 9: Discrete particle fragmentation

The result of a discrete particle impingement on a solid surface depends on the properties of the particle, the surface conditions and the kinematic parameters. A significant dimensionless parameter is the Reynolds number representing the ratio of the inertia to the viscous dissipative forces expressed as,

$$\mathrm{Re} = \frac{\rho_p D_{p0} u_{p0}}{\mu_p}$$

The Weber number describes the ratio of kinetic energy to surface energy

$$\mathrm{We} = \frac{\rho_p D_{p0} u_{p0}^2}{\sigma_p}$$

where, ρ_p, μ_p and σ_p are the droplet density, dynamic viscosity and surface tension for the fluid-air interface, respectively. D_{p0} and u_{p0} are the initial droplet diameter and normal velocity to the surface respectively, before impingement. The Reynolds number and the

Weber number can be combined to the Ohnesorge number, expressed as,

$$\mathrm{Oh} = \frac{\sqrt{\mathrm{We}}}{\mathrm{Re}}$$

Vidaurre and Hallet [101] discussed the parameters influential in particle impact and breakup. A breakup criterion for water was given by, We ≥ 7. Ice undergoes major fragmentation for We > 100. The present study assumes all particles collide when encountering a blade row and undergo breakup/splash.

A splash model presented by Mundo et al. [69], is applied for comparison with the results from the present study. The empirical formulas calculate splashed drop size as a function of the incoming parameters. Mundo et al. [69] introduced the characteristic fragmentation parameter influencing the droplet breakup

$$K = \mathrm{Oh}\,\mathrm{Re}^{1.25}$$

Thus, for splash to occur the following criterion is required,

$$K = \left(\frac{\rho_p^3 D_p 0^3 u_p 0^5}{\sigma_p^2 \mu_p}\right)^{1/4} \geq 57.7 \tag{20}$$

The resulting number of secondary droplets are computed as,

$$n_s = 1.676 \times 10^{-5} K^{2.539} \; ; \; n_s \leq 1000 \tag{21}$$

Chapter 6, Section 6.5, for parametric studies, compares the results obtained by applying the fragmentation and splash model used in the present study, with the model presented by Mundo et al. [69].

2.6 Discrete phase governing equations

Coupling between the two phases happens through mass, momentum and energy transfer between phases. The governing equations are constructed from the coupled physics as shown in Fig. 10.

2.6.1 Governing Equations: Momentum Transport

The airflow imparts momentum to the discrete phase as formulated by the equation of motion given by Eq. 22. Due to the large ice/water droplet and air density ratio, the force

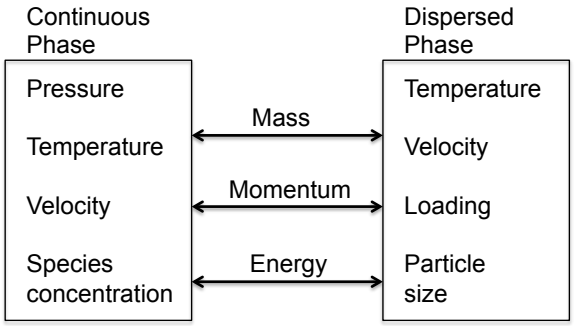

Figure 10: Schematic of coupling effects (Crowe et al. [16])

governing the momentum transfer between the continuous and discrete phase is predominantly the drag force.

$$m_p \frac{du_p}{dt} = \frac{1}{2}\rho_c C_D A_p |u - u_p| (u - u_p) = F_D \tag{22}$$

The parameter f_D is defined as follows to represent the drag force, F_D for all discrete elements,

$$f_D = \frac{N_p}{u - u_p} \frac{F_D}{dV} \tag{23}$$

Equation 22 tracks the motion of the discrete particles in a Lagrangian reference frame. C_D is the drag coefficient which depends on the particle shape and the relative Reynolds number. m_p is the particle mass and A_p is projected area in the direction of relative velocity of the particle, ρ_c is the density of air, and u_p and u are the velocities of the ice/water droplet and the humid air respectively. Drag force contributes to the coupling of the discrete and gas phases through the gas momentum equation (Eq. 8).

Defining the dispersed phase relative Reynolds number Re_p as

$$\mathrm{Re}_p = \frac{\rho_c D_p |u - u_p|}{\mu_c}$$

where, D_p is the ice crystal or water droplet diameter and μ_c is viscosity of air (continuous phase). Ice particles are assumed to enter the compressor at 1/10th the speed of the incoming airflow rate.

The distance travelled by the particle can then be found by integrating the velocity.

$$s - s_0 = \int_0^t u_p \, d\tau \tag{24}$$

2.6.2 Governing Equations: Mass Transport

Evaporation of water droplets leads to an addition of mass (s_{vapor}) to the air stream resulting in a mass coupling between the continuous and discrete phase. Figure 11 illustrates the ice particle break-up/ water splash and phase changes of ice ingested in the compressor.

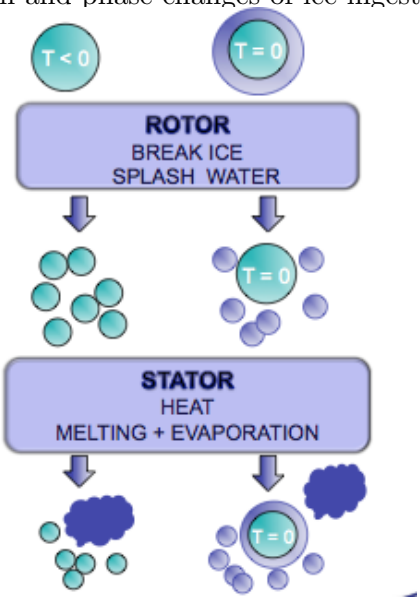

Figure 11: Schematic of ice flow and corresponding phase changes

The driving force for evaporation is the difference in concentration of the droplet vapor between the droplet surface and free stream. The mass efflux at the surface of evaporating droplet can be derived from Fick's law (Crowe et al. [16]).

$$\frac{dm_v}{dt} = -\,\mathrm{h_m}\left(\rho_{v,s}(T_p) - \mathrm{RH}\,\rho_{v,s}(T_g)\right)\pi D_p^2 \tag{25}$$

where, $\mathrm{h_m}$ is the mass transfer coefficient. $\rho_{v,s}(T_p)$ is the saturated vapor density at the same temperature as the water surface, T_p. $\rho_{v,s}(T_g)$ is the saturated vapor density at the free stream temperature, T_g . RH is the percentage relative humidity of the air and is defined as the ratio of the partial pressure of water vapor (e_w) to the saturated vapor pressure of water (e_w^*), at a prescribed temperature.

$$\mathrm{RH} = \frac{e_w}{e_w^*} \times 100\% \tag{26}$$

In order to account for the influence of convection on the water evaporation process, empirical correlation laws are used both for heat and mass transfer modifications. The mass

transfer coefficient (h_m) is expressed as a function of the Sherwood number (Sh) and the air-water molecular diffusivity (D_ν). A similar correlation is applicable for the heat transfer coefficient (h), which is a function of the coefficient of thermal conduction (k) and Nusselt number (Nu) ([34]). Sh and Nu are functions of the relative particle Reynolds number, Schmidt number Sc and Prandtl number Pr.

$$\begin{aligned} \mathrm{Sh} = \frac{h_m\, D_p}{D_\nu} &= 2 + \left(0.4\sqrt{\mathrm{Re}_p} + 0.06\,\mathrm{Re}_p^{2/3}\right)\mathrm{Sc}^{0.4} \\ \mathrm{Nu} = \frac{h\, D_p}{k} &= 2 + \left(0.4\sqrt{\mathrm{Re}_p} + 0.06\,\mathrm{Re}_p^{2/3}\right)\mathrm{Pr}^{0.4} \end{aligned} \tag{27}$$

The correlation is for a spherical particle. Possible sticking and accretion of the ice to metal is neglected. Thus the mass transfer relation from Eq. 25 can be rewritten as,

$$\frac{dm_v}{dt} = -\,\mathrm{Sh}\,D_\nu\left(\rho_{v,s}(T_p) - \mathrm{RH}\,\rho_{v,s}(T_g)\right)\pi D_p \tag{28}$$

The diffusion coefficient calculated from the formulation proposed by Marrero and Mason [57], is given by,

$$D_\nu(m^2/s) = \begin{cases} 1.87\times10^{-10}\,\dfrac{T_g^{2.072}}{p_g}, & 280 < T_g < 450K \\ 2.75\times10^{-9}\,\dfrac{T_g^{1.632}}{p_g}, & 450 < T_g < 1070K \end{cases}$$

where, p_g is the gas pressure in Pa and T_g is the gas temperature in Kelvin.

2.6.3 Governing Equations: Energy Transport

Convective heat transfer from the continuous phase is manifested as a rise in discrete element temperature. Some of the energy is expended as work associated with phase change [54].

The first law of thermodynamics dictates,

$$m_p C_p \frac{dT_p}{dt} = h\,\pi D_p^2\,(T_g - T_p) + L_{\mathrm{vap}}\frac{dm_v}{dt} + L_{\mathrm{melt}}\frac{dm_{\mathrm{melt}}}{dt} \tag{29}$$

where, L_{melt} and L_{vap} are the respective latent heats for melting and evaporation. C_p is the discrete particle (ice/water) specific heat at constant pressure.

The form of the energy equation changes according to the phase of the discrete particle [85]. An ice crystal at subzero temperatures absorbs energy from air to increase temperature, T_p assuming no phase change, as follows

$$m_p C_p \frac{dT_p}{dt} = h\,\pi D_p^2\,(T_g - T_p) \tag{30}$$

The ice crystals below a certain threshold diameter is assumed to directly sublimate.

As ice crystals start to melt, a thin water film forms on the surface. The ice core and the water film remain at freezing temperatures with all the heat absorbed in phase changes. During the change in phase, when the particle temperature remains constant at the saturation temperature, the heat transferred is just sufficient to balance the energy required for the change in phase to water, $\dot{m}_{\text{melt}}$ and vapor, $\dot{m}_v$.

$$\mathrm{h}\,\pi D_p^2\,(T_g - T_p) = -\,\mathrm{L}_{\text{vap}}\,\frac{dm_v}{dt} - \mathrm{L}_{\text{melt}}\,\frac{dm_{\text{melt}}}{dt} \tag{31}$$

Once the ice core completely melts, the temperature of the water droplet formed can be evaluated by the energy balance. The heat conducted is partially used for latent heat transfer, L_{vap} and remaining energy is used to increase its temperature, T_p.

$$m_p C_p \frac{dT_p}{dt} = \mathrm{h}\,\pi D_p^2\,(T_g - T_p) + \mathrm{L}_{\text{vap}}\,\frac{dm_v}{dt} \tag{32}$$

The momentum, mass and energy transfer of the discrete phase as given by Eq. 22, Eq. 28, and Eq. 29, give rise to source terms in the continuous phase [47]. Also the discrete particle position, phase (ice, ice with water film or water droplet), velocity, temperature and mass are updated for the next time step.

2.7 Modeling of discrete phase source terms

2.7.1 Water vapor mass coupling term

The vapor flux term per unit volume is written as,

$$s_{\text{vapor}} = -\frac{1}{dV}\sum_p N_p\,\dot{m}_v \tag{33}$$

where, $\dot{m}_v$ is the water vapor flux from all p discrete particles. s_{vapor} is the vapor mass source per unit volume. The negative sign indicates that a water droplet losing mass is adding mass to the carrier phase. This term couples the discrete and gas phases through the gas continuity equation (Eq. 6).

2.7.2 Momentum equation coupling term

The momentum coupling term consists of the following two terms,

1. Force on the fluid per unit volume due to dispersed phase moving with velocity u_p, arises due to addition of vapor (Eq. 33) into the flow : $u_p s_{\text{vapor}}$

2. Drag force acting on the discrete particles by the fluid (Eq. 23).

Adding up the source terms, the total contribution towards the momentum of the gas phase (Eq. 8), can be expressed as,

$$s_{\text{mom}} = u_p s_{\text{vapor}} - f_D \left(u - u_p\right) \tag{34}$$

2.7.3 Energy equation coupling term

The energy coupling term consists of the following three terms,

1. The enthalpy added due to mass of vapor (Eq. 33), from discrete particles moving with a velocity u_p , is expressed as $s_{\text{vapor}} \left(h_p + u_p^2\right)$. h_p is the discrete phase enthalpy flux.

2. The air does work in driving the discrete phase particles through the compressor (Eq. 23). The corresponding power lost in drag per unit volume of the gas is given by, $f_D \left(u - u_p\right) u_p$.

3. Energy is transferred between the discrete and the continuous phase,

$$\dot{q}_p = \frac{\dot{Q}}{dV} = \frac{N_p}{dV} \, \text{h} \, A_p (T_p - T_g)$$

   where h is the heat transfer coefficient and T_p is the temperature of the discrete particles, while T_g in the gas temperature.

Thus the total contribution from the discrete phase to the energy of the gas phase (Eq. 11) can be expressed as,

$$s_{\text{energy}} = s_{\text{vapor}} \left(h_p + u_p^2\right) - f_D \left(u - u_p\right) u_p + \dot{q}_p \tag{35}$$

2.8 Unsteady discrete phase equation

A species transport equation for conservation of water vapor is used to evaluate the specific humidity or the mixing ratio, q. This equation simply indicates that the total amount of water vapor in a parcel is conserved as the parcel moves, except when there are sources due to evaporation and sinks due to condensation. Specific humidity ratio (q) is expressed as a ratio of mass of water vapor (m_v) per unit mass of dry air (m_a).

The unsteady transport equation for q states that

$$\frac{\partial}{\partial t}\left(\rho_c q\right) + \frac{\partial}{\partial x}\left(\rho_c u q\right) = s_{\text{vapor}} \tag{36}$$

where u is the axial velocity of airflow. s_{vapor} is given by Eq. 33.

Water vapor at partial pressure e_w and dry air at partial pressure $p_g - e_w$, are both assumed to behave as ideal gases. Relative humidity is defined in Eq. 26. Specific humidity is related to the relative humidity by the following equation.

$$\begin{aligned} q = & \quad \frac{m_v}{m_a} \\ = & \quad \frac{R_d}{R_v}\frac{e_w}{p_g - e_w} = 0.622\frac{e_w}{p_g - e_w} \\ = & \quad 0.622\,\text{RH}\,\frac{e_w^*}{(p_g - \text{RH}\,e_w^*)} \end{aligned} \tag{37}$$

Table 1: Gas properties

Gas	Specific gas constant (J/kg/K)	Molecular weight (g/mole)
Dry air	R_d: 287.04	MW_d : 28.96
Vapor	R_v: 461.50	MW_v : 18.015

The specific gas constants (R_d, R_v), and molecular weights ($\text{MW}_\text{d}, \text{MW}_\text{v}$), for dry air and water vapor, respectively, are given in Table 1. Relative humidity is updated at the end of every time step and plays an important role in the mass transport equation as shown in Eq. 28.

2.9 Summary of unsteady governing equations

The unsteady governing equations for mass (Eq. 6), axial momentum (Eq. 8), circumferential momentum (Eq. 9), energy (Eq. 11), and water vapor transport (Eq. 36) have been

derived.

A generic conservative law governing one dimensional unsteady flow through the compressor can be expressed as,

$$\frac{\partial \mathbf{V}}{\partial t} + \frac{\partial \mathbf{F}}{\partial x} = \mathbf{Q} \tag{38}$$

$\mathbf{V}$ is a vector of conserved quantities with independent variables of space x and time t, $\mathbf{F}$ is a vector for the convection flux, and $\mathbf{Q}$ is a vector for the source terms.

$$\mathbf{V} = \begin{bmatrix} \rho_c \\ \rho_c u \\ \rho_c v_\theta \\ \rho_c \left(e_c + \frac{1}{2}\left(u^2 + v_\theta^2\right)\right) \\ \rho_c q \end{bmatrix} \qquad \mathbf{F} = \begin{bmatrix} \rho_c u \\ \left(p_g + \rho_c u^2\right) \\ \rho_c u v_\theta \\ \rho_c u h_0 \\ \rho_c u q \end{bmatrix} \tag{39}$$

$$\begin{aligned} h_0 &= \left(e_c + \frac{1}{2}\left(u^2 + v_\theta^2\right)\right) + \frac{p_g}{\rho_c} \\ &= \frac{\gamma}{\gamma - 1}\frac{p_g}{\rho_c} + \frac{1}{2}\left(u^2 + v_\theta^2\right) \end{aligned}$$

Here, $\rho_c \left(e_c + \frac{1}{2}\left(u^2 + v_\theta^2\right)\right)$ is the total energy density. h_0 is the total gas enthalpy.

We assume a perfect gas satisfying the following relations, $p_g = \rho_c R T_g, p_g = (\gamma - 1)\rho_c e_c, \gamma = C_P/C_V$.

The source term vector in Eq. 38 is categorized by their physical contributions as:

$$\mathbf{Q} = \mathbf{Q}_{\text{blade}} + \mathbf{Q}_{\text{bleed}} + \mathbf{Q}_{\text{discrete}} \tag{40}$$

$$\mathbf{Q}_{\text{blade}} = \begin{bmatrix} 0 \\ \frac{1}{A_c} p_g \frac{dA_c}{dx} + f_x \\ f_\theta \\ \dot{w}_s \\ 0 \end{bmatrix} \qquad \mathbf{Q}_{\text{bleed}} = - \begin{bmatrix} s_{\text{bleed}} \\ u\, s_{\text{bleed}} \\ v_\theta\, s_{\text{bleed}} \\ s_{\text{bleed}} \left(h_c + \frac{1}{2} \left(u^2 + v_\theta^2 \right) \right) \\ 0 \end{bmatrix} \tag{41}$$

A control volume in a typical compressor illustrated in Fig. 7 is acted upon by a body force, f_x per unit volume in the axial direction. The circumferential momentum exchange is f_θ and the shaft work $\dot{w}_s$ links the change in total enthalpy of the fluid due to the blades. A set of quasi-steady stage characteristics provides these stage forces and shaft work inputs to the momentum and energy equations as derived in the section 2.3. The quasi-linear approach of modeling the flow permits flow area variation, $\frac{dA_c}{dx}$, in the axial direction of the compressor, and is manifested by an additional geometrical source term. These contributions are reflected in $\mathbf{Q}_{\text{blade}}$. Equation 2 computes the bleed mass flux, $\dot{m}_b$ and the corresponding effect is modeled by $\mathbf{Q}_{\text{bleed}}$.

$$\mathbf{Q}_{\text{discrete}} = \begin{bmatrix} s_{\text{vapor}} \\ u_p\, s_{\text{vapor}} - f_D \left(u - u_p \right) \\ 0 \\ s_{\text{vapor}} \left(h_p + u_p^2 \right) - f_D \left(u - u_p \right) u_p + \dot{q}_p \\ s_{\text{vapor}} \end{bmatrix} \tag{42}$$

The discrete phase source terms are detailed in Sec. 2.7. The source terms in the continuous phase governing equations as given by $\mathbf{Q}_{\text{discrete}}$, arise from the mass (Eq. 33), momentum (Eq. 34), and energy (Eq. 35) interactions with the discrete phase.

2.10 Impact of moisture on the compressor flow dynamics

The melting ice crystals and water droplets evaporate as they flow through the compressor. The presence of water vapor alters the working medium gas properties [75]. The air-water mixture has different molecular weight (MW) as that compared to dry air. The dynamic characteristic of the air-vapor continuous phase is altered as a consequence. Thus, it is important that the model captures the changing gas properties as water vapor is produced with increasing ice ingestion.

The relations governing moist air properties are adopted from Walsh and Fletcher [102]. The gas constant for a mixture or a single constituent is $R = R_0/\,\mathrm{MW}$, where R_0 is the universal gas constant. In the case of the dry air and vapor mixture, $\mathrm{R_{HUMID}}$ becomes,

$$\mathrm{R_{HUMID}} = \frac{R_0}{\mathrm{MW_m}}$$

$\mathrm{MW_m}$ is the moist air molecular weight. With q defined as the water to air ratio by mass, the mixture molecular weight is given as,

$$\mathrm{MW_m} = \frac{1}{\dfrac{q}{\mathrm{MW_v}} + \dfrac{1-q}{\mathrm{MW_d}}}$$

where, $\mathrm{MW_v}$ is the molecular weight of vapor and $\mathrm{MW_d}$ is the molecular weight of dry air. The values are given in the table for gas properties (Table 1). The molecular weight of humid air is less than that of dry air. Thus the gas constant of humid air is higher than that of dry air. Also the specific heat ratio, γ of humid air is higher than that of dry air. This affects the ideal gas relation, speed of sound through the humid air and all related results.

The ratio of specific heats of air water mixture is obtained from the mass average values of its constituents.

$$\gamma_{\mathrm{HUMID}} = q_{\mathrm{molar}}\gamma_w + \left(1 - q_{\mathrm{molar}}\right)\gamma_a$$

where, $q_{\mathrm{molar}} = \dfrac{\mathrm{MW_d}}{\mathrm{MW_v}}q$, is the ratio of water to air by the number of moles.

The moisture impacts the specific heat at constant pressure, C_p. The specific heat of

Table 2: Constants for specific heat of dry air and water

Constants	Dry Air C_{pa}	Water C_{pw}
A_0	0.992313	1.937043
A_1	0.236688	-0.967916
A_2	-1.852148	3.338905
A_3	6.083152	-3.652122
A_4	-8.893933	2.33247
A_5	7.097112	-0.819451
A_6	-3.234725	0.118783
A_7	0.794571	0
A_8	-0.081873	0
A_9	0.422178	2.860773
A_{10}	0.001053	-0.000219

air is calculated from a 10th order polynomial fit.

$$C_p = A_0 + A_i T_g^i \quad \text{for } i = 1, \ldots, 10$$

where, T_g is the gas static temperature divided by 1000. Table 2 shows the values for A_i

The specific heat of moist air becomes,

$$C_{p\text{HUMID}} = q_{\text{molar}} C_{pw} + \left(1 - q_{\text{molar}}\right) C_{pa}$$

The accuracy of the curve fitted C_p using the above constants is within 0.6% range at $0 - 370°C$.

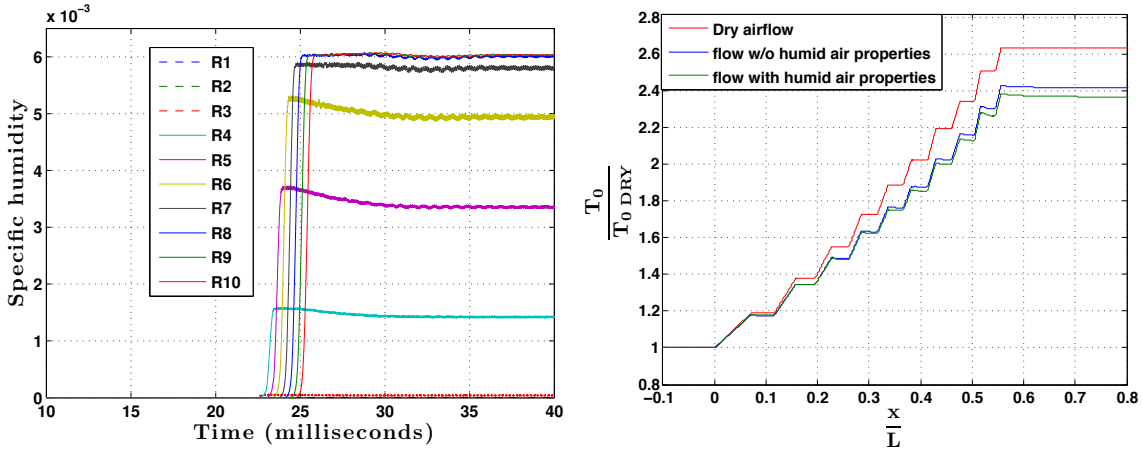

(a) Specific Humidity

(b) Temperature distribution

Figure 12: Impact of humidity on compressor response.

Figure 12(a) shows the transient variation of specific humidity (q), the ratio of mass of vapor to the mass of dry air, for 0.74% of steady flow rate of ingested ice. The vapor content is captured at the inlet of all the rotor blades of the ten-stage compressor. This is evident from the increasing specific humidity. Figure 12(b) compares the variation in the temperature profile across the compressor, with and without taking into account the change in gas properties due to moisture for a 0.74% ice inflow rate. The temperature difference is subtle in the front stages that contain a higher concentration of ice particles. The effect is more pronounced at the rear stages where more evaporation occurs. The water vapor in the air decreases the molecular weight of the gas mixture and consequently increases the gas constant. The specific heat ratio shows a decrease with each stage because of the increasing temperature profile across the compressor. The reduction in specific heat is furthered by the addition of vapor to air. The compressor response will be increasingly affected as the ice flow rate increases. Therefore, the present work includes the impact of water vapor on the humid air gas properties.

CHAPTER III

SOLUTION TECHNIQUE

The mathematical model was discussed in Chapter 2 and the solution methodology is addressed in this chapter. The coupled governing equations that model the humid air flow and discrete phase through the compressor consists of the quasi-one-dimensional Euler equations given by,

1. Mass continuity of humid air, Eq. 6
2. Axial momentum, Eq. 8
3. Circumferential momentum, Eq. 9
4. Energy conservation, Eq. 11
5. Mass conservation of vapor, Eq. 36

The discrete phase Lagrangian model is given by,

1. Mass transport, Eq. 25
2. Momentum transport, Eq. 22
3. Energy transport, Eq. 29

The one-dimensional nature of the numerical model offers simple and fast computations. A description of the time accurate second order scheme is presented in Section 3.4.2. The flow is assumed to be inviscid and the absence of viscous terms reduces scheme stability. Hence, in case of high speed operation, a more diffusive first order spatial scheme is applied instead of the second order spatial scheme that is used otherwise. The source terms to model the flow response of the blades in the multistage compressor are interpolated from the given characteristic blade force and work coefficient maps, as described in Section 2.3. The solution technique incorporates different aspects of the numerical model including bleed air

and ice ingestion. The methodology involves initializing the flow variables and then solving the time accurate set of equations. Additionally, the boundary conditions at the inlet and exit of the compressor are formulated.

3.1 Input parameters

The stagnation pressure, p_0 and temperature, T_0, are prescribed at the inlet of the compressor. In a simulation of a rig compressor set-up that draws air from the atmosphere, these quantities may be set to ambient conditions, p_{amb} and T_{amb}. Figure 6 shows a schematic of the multistage compressor geometry. The compressor is divided into rotor-stator stages. A non-uniform grid is used to discretize the one-dimensional computational domain across which the calculations are performed.

The inlet guide vane (IGV) angle and the mass flow rate at the choked nozzle at the exit of the compressor are also specified. The geometry of the compressor is specified in the form of hub radius, tip radius, and axial chord length of the blades in the compressor and the total compressor length, L. The rotor annular area perpendicular to the axial flow component is calculated from the hub and tip radii from the centerline as given in Eq. 43. The aerodynamic blockage, B, is multiplied to account for reduced area available for the flow due to blockage of blades and boundary layer.

$$A = B\pi \left(R_{\text{tip}}^2 - R_{\text{hub}}^2\right) \tag{43}$$

3.2 Steady State Initialization

The steady state initialization is done in three steps. In the first step, the Mach number is found at the IGV exit, which is also the first rotor blade inlet point. Then starting from the IGV exit, all the static flow quantities such as pressure, p_g, temperature, T_g, density, ρ_c, velocities u and v are solved at each upstream station of the multistage compressor from the steady state mass, momentum and energy equilibrium equations. The second step involves solving for these conservative values through the rotor/ stator and inter-blade stations in the compressor. In the last step, the values are solved at the exit duct and plenum. These steps are as detailed below.

3.2.1 Static Flow Conditions at Inlet to the First Rotor

An IGV precedes the first rotor of the compressor. The Mach number at the IGV exit or the first rotor blade inlet can be found from the specified mass flow rate, $\dot{m}$, and the IGV exit angle, α_{IGV}.

The mass flow rate for ideal compressible gas in terms of total flow condition is,

$$\dot{m} = \frac{(A\cos\alpha_{IGV})\,p_0}{\sqrt{T_0}}\sqrt{\frac{\gamma}{R}}M\left(1+\frac{\gamma-1}{2}M^2\right)^{-\frac{\gamma+1}{2(\gamma-1)}} \tag{44}$$

where, area, A, as given by Eq. 43 is perpendicular to the axial direction. The equation yields the Mach number, M, and consequently the static flow conditions are computed as a function of Mach number. For an isentropic flow of a calorically perfect gas, the static pressure and temperature are given by,

$$\begin{aligned} p_g &= p_0\left(1+\frac{\gamma-1}{2}M^2\right)^{-\frac{\gamma}{\gamma-1}} \\ T_g &= T_0\left(1+\frac{\gamma-1}{2}M^2\right)^{-1} \end{aligned} \tag{45}$$

The velocity at the rotor inlet becomes,

$$c = \sqrt{\gamma R T_g} \qquad u = cM\cos\alpha_{IGV} \qquad v_\theta = cM\sin\alpha_{IGV} \tag{46}$$

where u and v_θ are axial and circumferential components of the flow velocity, respectively, while c is the speed of sound.

3.2.2 Steady State Initialization Upstream of First Rotor Blade

The control volumes of an inlet guide vane and an inlet duct are upstream of the compressor blades as shown in Fig. 6. The steady state Euler equations are solved between unknown static flow variables at an upstream station, m, and the known values at a downstream station, $m+1$, starting from the rotor inlet values computed in Eq. 45 and Eq. 46.

The humid air flow rate, $\dot{m}$, remains constant in the absence of any bleed air escaping from the inlet volumes. Therefore the circumferential velocity is rendered constant at all stations upstream of the first rotor, as given by the steady state circumferential momentum equation,

$$\dot{m}\,(v_{\theta m+1} - v_{\theta m}) = 0 \qquad \Rightarrow v_{\theta m} = v_{\theta m+1} \tag{47}$$

The axial momentum equation is solved to find the converged static conditions as explained by the flowchart given in Fig. 13. The process is started from the rotor inlet where the flow quantities are computed previously and marched upstream through the discretized compressor grid points towards the compressor inlet. The mass flow rate, $\dot{m}$, circumferential velocity, $v_{\theta m}$, and the geometry are known at every station m. The total pressure, p_0, and temperature, T_0, remain constant through these volumes in the absence of any external work on the flow.

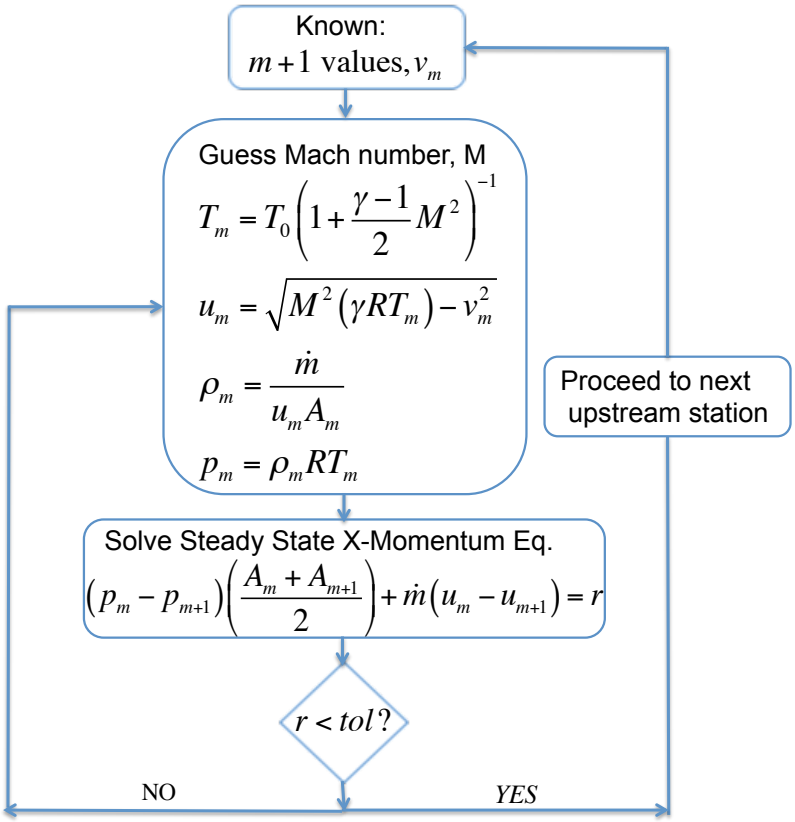

Figure 13: Flowchart displaying calculation of static conditions upstream of first rotor.

The velocities obtained at the first inlet location of the compressor are used to set the angle of the flow into the compressor as an inlet boundary condition.

$$\alpha_{\text{inlet}} = \tan^{-1}\left(\frac{v_{\theta\text{inlet}}}{u_{\text{inlet}}}\right) \tag{48}$$

3.2.3 Steady State Initialization at Compressor Blade Rows

Chapter 2, section 2.9 expresses the unsteady one-dimensional Euler equations in vector form in Eq. 38. The steady state flow field in the compressor is derived by neglecting the transient part of the equation. The steady state equation in vector form then becomes,

$$\frac{d\mathbf{F}}{dx} = \mathbf{Q} \tag{49}$$

where, $\mathbf{F}$ is a vector for the convection flux, and $\mathbf{Q}$ is a vector for the source terms. This flow field is then used as the initial condition for the transient computations.

Calculation of force and work source terms across blade rows from given data

The flow dynamics of the blade rows now depend on interactions with the blades. This is reflected by the blade source terms on the right hand side of the steady state Euler equations. The static quantities from the data are used to calculate the force, work and flow coefficients for all the blade stages. The meanline or pitchline velocity across the rotor stages for a compressor operated at a rpm, N, is given by

$$U_{\text{meanline}} = \frac{2\pi N}{60}\frac{R_{\text{tip}} + R_{\text{hub}}}{2} \tag{50}$$

The stage flow coefficient is calculated as the ratio between the axial component of velocity and the meanline velocity.

$$\phi = \frac{u}{U_{\text{meanline}}} \tag{51}$$

Equation 52 shows the pressure coefficient across a blade control volume.

$$\psi_{\text{Pressure}} = \frac{p_{g\text{Blade Exit}} - p_{g\text{Blade Inlet}}}{\frac{1}{2}\rho_c U^2_{\text{meanline}}} \tag{52}$$

Equation 53 expresses the momentum contribution by the mass flow rate across a blade control volume,

$$\psi_{\text{Mass}} = \dot{m}_{\text{Blade Inlet}}\left(\frac{u_{\text{Blade Exit}} - u_{\text{Blade Inlet}}}{A_{avg}\frac{1}{2}\rho_c U^2_{\text{meanline}}}\right) \tag{53}$$

The axial force coefficient become $\psi_{f_x} = \psi_{\text{Mass}} + \psi_{\text{Pressure}}$. Equation 13 in section 2.3 explains the contribution of ψ_{f_x} in the momentum equation.

The work coefficient depends on the enthalpy rise through the stage

$$\psi_{\mathrm{W}} = \left(\int_{T_{0Inlet}}^{T_{0Exit}} C_p(T_g) T_0 \right) / U^2_{\mathrm{meanline}} \tag{54}$$

The turning force coefficient is obtained as,

$$\psi_{f\theta} = \dot{m}_{\text{Blade Inlet}} \left(\frac{v_{\theta\text{Blade Exit}} - v_{\theta\text{Blade Inlet}}}{\frac{1}{2}\rho_c U^2_{\mathrm{meanline}}} \right) \tag{55}$$

Equation 14 in section 2.3 describes the contribution of $\psi_{f\theta}$ in the circumferential equation.

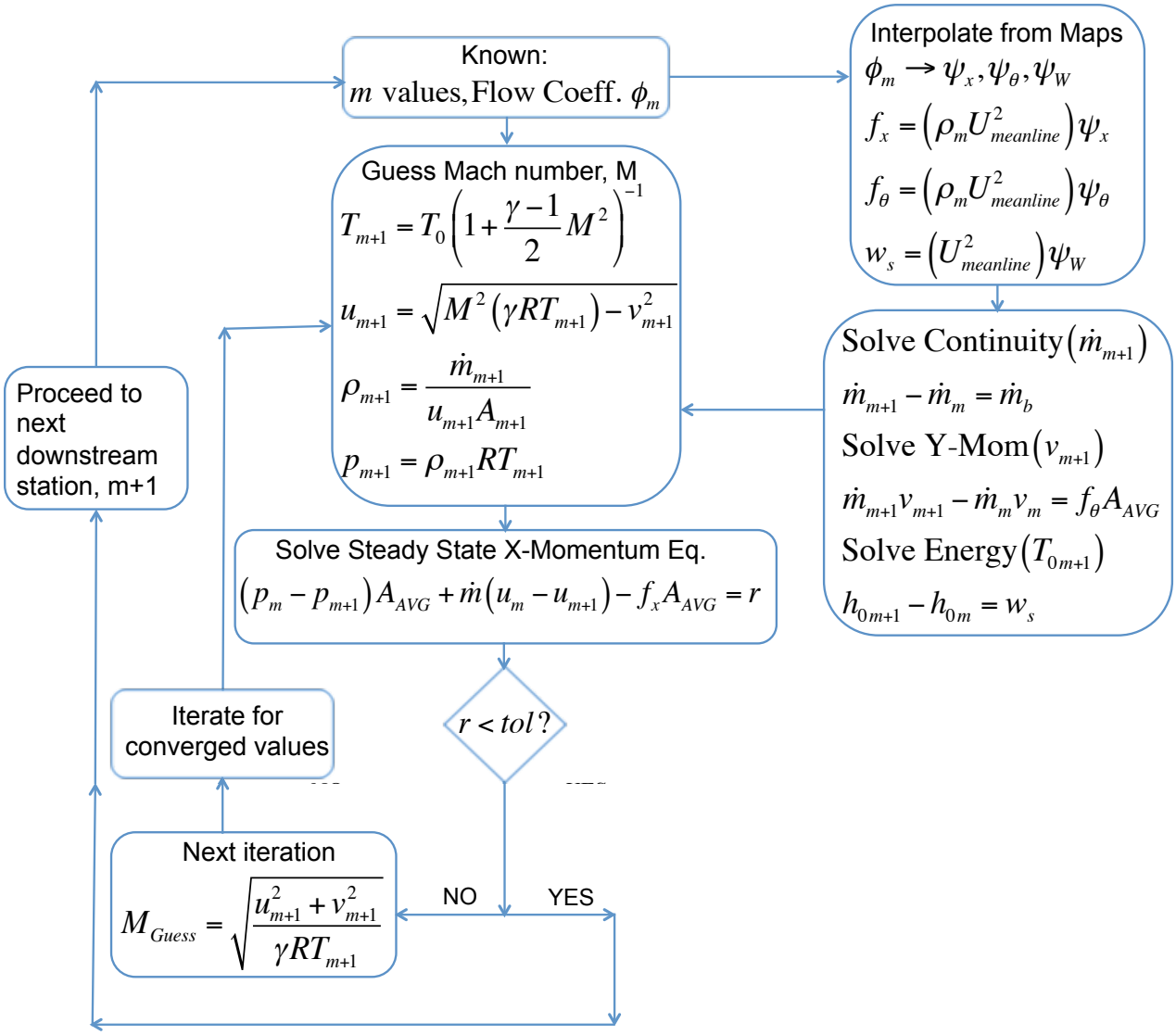

Figure 14: Flowchart displaying calculation of static conditions of the blade row grid points.

Once the compressor performance maps are constructed from the given data, the steady state Euler equations are solved. The calculations are started from the rotor inlet where the flow quantities are as computed previously and marched through the discretized compressor grid points towards the exit of the last stator stage. The algorithm in Fig.14 describes the scheme.

3.2.4 Compressor Interstage and Diffuser Volume Flow Quantities

Every rotor and stator blade row control volume has an intermediary control volume. Also the compressor has an exit diffuser after the last blade row. At these interstage gaps and exit volume the procedure for finding the flow parameters is same as described for the inlet volumes. The mass flow rate is adjusted for any possible bleed air through the compressor. The blade forces and shaft work are absent resulting in $f_x = 0, f_\theta = 0, \dot{w}_s = 0$. Similar to the blade row calculations, static flow values are found from the iterative procedure for Mach number as given by Fig. 14.

Exit boundary condition based on steady state calculations

The mass flow rate of an ideal compressible gas in terms of total conditions,

$$\begin{aligned}\dot{m} &= \rho_c u A \\ &= \frac{A p_0}{\sqrt{T_0}} \sqrt{\frac{\gamma}{R}} M \left(1 + \frac{\gamma - 1}{2} M^2\right)^{-\frac{\gamma+1}{2(\gamma-1)}}\end{aligned}$$

A choked exit implies maximum mass flow rate at Mach number, $M = 1$. Thus, mass flow rate becomes,

$$\dot{m} = \frac{A p_0}{\sqrt{T_0}} \sqrt{\frac{\gamma}{R}} \left(\frac{\gamma + 1}{2}\right)^{-\frac{\gamma+1}{2(\gamma-1)}}$$

Based on the above expression, a simplified constant throttle value, k_T, is calculated as an exit boundary condition.

$$k_T = \frac{\dot{m}_{\text{exit}}}{(p_{\text{exit}} - p_{amb})} \tag{56}$$

where, the mass flow rate at the exit, $\dot{m}_{exit} = \dot{m} - \dot{m}_b$.

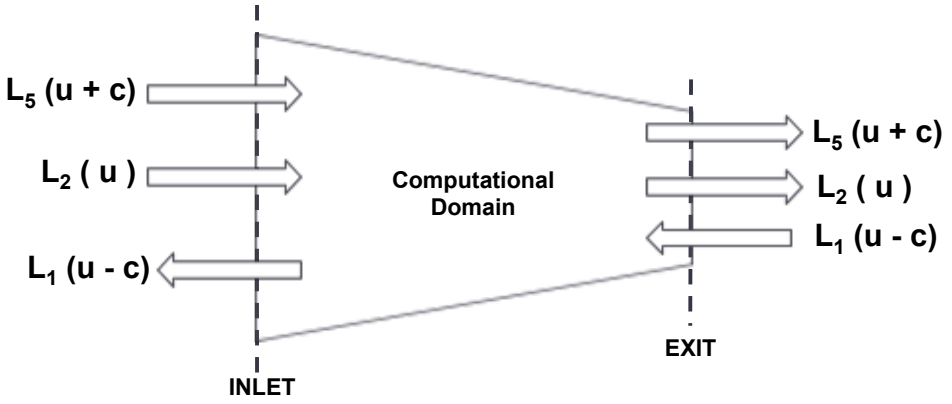

Figure 15: Waves entering and leaving the computational domain which is the compressor inlet and exit, for subsonic flow boundary conditions

3.3 Transient Operation: Boundary conditions

The numerical solution to a hyperbolic system of differential equations like the compressible Euler fluid flow equations, are computed over a finite computational domain which is across the compressor length. The state in the interior of the domain as well as the waves propagating across the boundary, define the evolution of the system through time. Figure 15 illustrates waves propagating into the computational volume and leaving the volume. The outgoing waves are prescribed entirely by the characteristic equations that offer a solution at or in the interior of the domain. The incoming waves require boundary conditions to completely specify their behavior. Thus, the specification of boundary conditions for the Euler system of equations (Eq. 38) becomes challenging since it has eigen values of both signs that imply incoming and outgoing waves. Thompson [94] and Poinsot and Lele [81] noted the appeal of using the characteristic form at the boundaries resulting in consideration for each of the waves separately.

A characteristic form of the Euler equations provides time dependent density, velocity and pressure equations.

$$\frac{d\rho_c}{dt} = \frac{-1}{c^2}\left[\mathrm{L}_2 + \frac{1}{2}\left(\mathrm{L}_1 + \mathrm{L}_5\right)\right] \tag{57a}$$

$$\frac{dp_g}{dt} = \frac{-1}{2}\left(\mathrm{L}_1 + \mathrm{L}_5\right) \tag{57b}$$

$$\frac{du}{dt} = \frac{-1}{2\rho c}\left(\mathrm{L}_5 - \mathrm{L}_1\right) \tag{57c}$$

where, c is the speed of sound given by Eq 46. L_1, L_2 and L_5 are the amplitudes of the characteristic waves associated with each characteristic velocity λ, $\lambda_1 = u - c, \lambda_2 = u, \lambda_3 = u + c$, respectively, as illustrated in Fig. 15. L_3 and L_4 are the characteristic waves in the Y and Z-directions that are neglected in the present one-dimensional approach. The wave amplitudes in terms of the flow variables are written by,

$$L_1 = \lambda_1 \left(\frac{\partial p_g}{\partial x} - \rho_c c \frac{\partial u}{\partial x} \right) \tag{58a}$$

$$L_2 = \lambda_2 \left(c^2 \frac{\partial \rho_c}{\partial x} - \frac{\partial p_g}{\partial x} \right) \tag{58b}$$

$$L_5 = \lambda_5 \left(\frac{\partial p_g}{\partial x} + \rho_c c \frac{\partial u}{\partial x} \right) \tag{58c}$$

Nonreflecting boundary conditions:

Thompson applied the nonreflecting boundary conditions for several fluid dynamics problems modeled by Euler equations. The formulation of nonreflecting boundary conditions prevents spurious, nonphysical reflections at domain boundaries, so that the solution of the flowfield is independent of the location of the far-field boundaries. As a result, the computational domain can be made smaller leading to higher computational efficiency (Giles [31]).

3.3.1 Inlet boundary conditions

Method 1: At the inlet boundary, physical conditions of the compressor inlet angle, stagnation pressure and stagnation temperature are specified. A physical boundary condition implies the specification of known physical behavior of dependent variables at the boundaries [81].

Governing laws that are employed to model the inlet boundary conditions are:

1. The total enthalpy preserved at the inlet gives the following condition,

$$\frac{\gamma}{\gamma - 1} \frac{p_1}{\rho_1} + \frac{1}{2} u_1^2 = C_p T_{amb} \tag{59}$$

   where T_{amb} is the inlet stagnation temperature, generally ambient conditions.

2. The isentropic flow relation at the inlet gives,

$$\frac{p_1}{p_{amb}} = \left(\frac{\rho_1}{\rho_{amb}} \right)^{\gamma} \tag{60}$$

where, p_{amb} and ρ_{amb} are the ambient pressure at the inlet and the corresponding density.

3. The inlet condition also takes into account the flow from the inlet guide vanes where the IGV angle is specified from the steady state initialization in Eq. 48.

$$\frac{v_\theta}{u} = \tan\left(\alpha_{\text{inlet}}\right) \tag{61}$$

4. Mass continuity at the inlet is given by the time dependent Euler equation as,

$$\frac{d\rho_c}{dt} + \frac{\rho_2 u_2 - \rho_1 u_1}{\Delta x} = 0 \tag{62}$$

The data point 1 is at the inlet boundary of the compressor and 2 is the interior data point. The pressure, density, axial and the swirl velocities are determined at the inlet from Eqs.(59) - (62).

Method 2: Nonreflecting Boundary conditions

The nonreflecting boundary condition at the inlet dictate, $\mathrm{L}_2 = 0$ and $\mathrm{L}_5 = 0$. L_1 is the amplitude of the wave traveling out of the compressor and can be extrapolated from the interior point at the compressor inlet. The swirl velocity v_θ is computed from Eq. 61. Thus, the characteristic form of Euler equations (Eq. 57), can be solved for all the unknown variables of pressure, velocities and density as follows,

$$\begin{aligned}
\mathrm{L}_1 &= \lambda_1 \left(\frac{\partial p_g}{\partial x} - \rho_c c \frac{\partial u}{\partial x} \right) \\
\frac{d\rho_c}{dt} &= -\frac{\mathrm{L}_1}{2c^2} \\
\frac{dp_g}{dt} &= -\frac{\mathrm{L}_1}{2} \\
\frac{du}{dt} &= \frac{\mathrm{L}_1}{2\rho_c c} \\
\frac{v_\theta}{u} &= \tan\left(\alpha_{\text{inlet}}\right)
\end{aligned}$$

The compressor steady state solution obtained by application of either of the methods, is the same. The method 1 is chosen for all the results shown in the present study since the acoustic waves entering the compressor are preserved. An external disturbance at the inlet that does not originate inside the compressor domain can be captured.

3.3.2 Exit boundary conditions

Method 1

The unknowns are the density, velocity and pressure and the L_1 wave traveling into the compressor at the exit boundary. The following steps are followed to compute the flow variables at the exit.

1. L_2, L_5 are the amplitude of the waves traveling out of the compressor and can be extrapolated from the interior points at the compressor exit, as given by Eq. 58.

2. A choked throttle prescribed at the exit boundary is manifested as a simplified relation between mass flow rate and static pressure at the exit station. The value for the throttle constant, k_T, is found from the initial condition given by Eq. 56 and is held constant. The throttle can be varied to control the mass flow rate through the compressor

$$\begin{aligned} \dot{m} &= k_T \left(p - p_{amb}\right) \\ \dot{\rho_c} u + \rho_c \dot{u} &= \left(k_T/A\right) \left(p - p_{amb}\right) \end{aligned} \tag{63}$$

3. Rewriting the characteristic equations (Eq. 57) as well as the throttle condition (Eq. 63),

$$\begin{aligned} \dot{\rho_c} &= \frac{-1}{c^2} \left[\mathrm{L}_2 + \frac{1}{2} \left(\mathrm{L}_1 + \mathrm{L}_5\right) \right] \\ \dot{p_g} &= \frac{-1}{2} \left(\mathrm{L}_1 + \mathrm{L}_5\right) \\ \dot{u} &= \frac{-1}{2\rho_c c} \left(\mathrm{L}_5 - \mathrm{L}_1\right) \end{aligned}$$

The above equations are solved simultaneously to find the unknown variables at the exit boundary, namely, ρ_c, u, p_g and L1. The swirl velocity is assumed to remain the same as the velocity at the interior point.

Method 2

Exit boundary condition for 100% **speed for a 4 stage compressor** A choked exit boundary reflects acoustic waves and excites acoustic oscillations. For the case of 100%

speed flow, it has been observed that the solver is unable to converge to a steady state. In a real engine the choked exit is interfaced with a plenum that provide acoustic attenuation. In the simulation the attenuation provided by the plenum has been achieved by combining nonreflecting boundary condition with a first order time lag that represents the volume of the plenum. The following steps are followed to compute the flow variables at the exit.

1. L_2 and L_5 are computed from the interior point as given by the Eq. 58.

2. Nonreflecting boundary condition is imposed by setting $L_1 = 0$.

3. The characteristic equations can be integrated in time to obtain the flow variables of pressure, velocity and density. Swirl velocity is maintained at the same value as in the interior.

$$\dot{\rho_c} = \frac{-1}{c^2}\left[\mathrm{L_2} + \frac{1}{2}\left(\mathrm{L_1} + \mathrm{L_5}\right)\right]$$
$$\dot{p_g} = \frac{-1}{2}\left(\mathrm{L_1} + \mathrm{L_5}\right)$$
$$\dot{u} = \frac{-1}{2\rho_c c}\left(\mathrm{L_5} - \mathrm{L_1}\right)$$

4. In addition to the above equations, an additional relation is formulated to provide an ability for changing the pressure at the throttle exit. A steady state pressure is calculated as,

$$p_{g\text{Exit SS}} = k_T u_{Exit} \tag{64}$$

The pressure at the exit at every time step is calculated via a time lag equation,

$$p_g^{n+1} = p_g^n + \left(p_{g\text{Exit SS}} - p_g^n\right)\frac{\Delta t}{\tau}$$

The variable τ takes into account the damping effect of a plenum at the compressor exit. The damping can be increased or reduced depending on how fast (time constant) the simulation is required to change to the modified pressure.

3.4 Numerical Scheme

3.4.1 Background

Numerical schemes can be classified as upwind and central difference schemes. Roe's linearized Riemann solver is a popular upwind scheme [84]. The upwind schemes involves

discretization of hyperbolic partial differential equations by using a finite difference stencil biased in the direction determined by the sign of the characteristic speeds (direction of propagation of information in a flow field). The implementation of central schemes are straightforward for general conservation laws and related equations governing the spontaneous evolution of large gradient phenomena. Lax-Friedrichs (LxF) central schemes are widely used. The central Nessyahu Tadmor (NT) scheme [72] is a modification to the basic LxF approach. Kurganov and Tadmor (KT) scheme [50] used in the present work, is built on the NT scheme. Naidoo and Baboolal [71] show the applicability of the KT scheme on hyperbolic problem with non-linear source terms.

3.4.2 Numerical solver

Second-order central difference KT scheme [50] admits a semi-discrete formulation, where the original partial difference equation is transformed into a set of ordinary differential equations (ODE). The resulting ODE's are solved with the standard Runge-Kutta solver.

The fully discrete second-order central scheme is constructed for systems of one-dimensional hyperbolic conservation laws.

1. The one dimensional unsteady flow through the compressor is given by Eq. 38 in a vector form,

$$\frac{\partial \mathbf{V}}{\partial t} + \frac{\partial \mathbf{F}}{\partial x} = \mathbf{Q} \tag{65}$$

Let v_j^n be an approximate value of the conservative variable $v(x = x_j, t = t^n)$ at the grid point $(x_j := j\Delta x, t^n := n\Delta t)$. The spatial term containing the numerical flux $f(v_j^n)$ is approximated by the KT scheme as,

$$H_{j+1/2}(t) := \frac{f\left(v_{j+1/2}^+\right) + f\left(v_{j+1/2}^-\right)}{2} - \frac{a_{j+1/2}^n}{2}\left[v_{j+1/2}^+ - v_{j+1/2}^-\right] \tag{66}$$

The left and right intermediate values $v^{\pm}$ at $x_{j+1/2}$

$$\begin{aligned} v_{j+1/2}^+ &:= v_{j+1}^n - \frac{\Delta x}{2}\left(v_x\right)_{j+1}^n \\ v_{j+1/2}^- &:= v_j^n + \frac{\Delta x}{2}\left(v_x\right)_j^n \end{aligned} \tag{67}$$

The conservation form of the scheme is written by substituting Eq. 66 in the conservation equation Eq. 65,

$$\frac{d}{dt}v_j(t) = -\frac{H_{j+1/2}(t) - H_{j-1/2}(t)}{\Delta x} \tag{68}$$

The local speed of propagation at the cell boundaries appearing in Eq. 66 is found as

$$a^n_{j+1/2} := max\ (u - c, u, u + c)^n_{j+1/2} \tag{69}$$

where, u is the axial velocity and c is speed of sound.

Here the exact spatial derivatives, $v_x(x_{j+1/2}, t^{n+1})$ appearing in Eq. 67, are approximated by

$$(v_x)^{n+1}_{j+1/2} = \frac{2}{\Delta x}\,\text{minmod}\left(\theta\frac{v^n_j - v^n_{j-1}}{\Delta x}, \frac{v^n_{j+1} - v^n_{j-1}}{2\Delta x}, \theta\frac{v^n_{j+1} - v^n_j}{\Delta x}\right),\ 1 \le \theta \le 2 \tag{70}$$

where, the multivariable minmod limiter is given by,

$$\text{minmod}\,(v_{x1}, v_{x2}, \cdots) := \begin{cases} \min_j & \text{if} \quad v_{xj} > 0 \quad \forall j \\ \max_j & \text{if} \quad v_{xj} < 0 \quad \forall j \\ 0 & \text{otherwise} \end{cases}$$

Note: v_x is most dissipative for $\theta = 1$, and is least dissipative for $\theta = 2$.

2. A second order Runge-Kutta method is used to solve the time domain. Let $C[u]$ be the spatial recipe discussed above for central differencing a grid function.

$$\begin{aligned} v^{(1)} &= v^n + \Delta t^n C[v^n] \\ v^{(l+1)} &= \eta_l v^n + (1 - \eta_l)\left(v^{(l)} + \Delta t^n C[v^{(l)}]\right),\ l = 1, 2, \cdots, s-1 \\ v^{n+1} &:= v^{(s)} \end{aligned} \tag{71}$$

For a second order Runge Kutta Method, $s = 2, \eta_l = 1/2$.

3.4.3 Stability Criterion

The Courant-Friedrichs-Lewy (CFL) condition specifies a necessary condition for convergence while numerically solving partial differential equation with an explicit time integration scheme. For a one-dimensional case the CFL has the following form,

$$C = \frac{u\Delta t}{\Delta x}$$

where, C is the Courant number, u is the velocity magnitude, Δt is the time step and Δx is the spatial distance between any two grid points across the compressor. The numerical stability of an explicit time-marching method is ensured for $C < 1$. In this work, the spatial discretization and time step are chosen such that the CFL criterion is met.

3.4.4 Modifications to solver for high speed operating conditions

For high speed and load operating conditions of the compressor flow, implementation of the numerical solver is challenging. High pressure loads, high mass flow rates with steep stage characteristic map make the solver sensitive to numerical variations. In the absence of a diffusive viscous term in the governing equations, the solver requires modification to reduce transient oscillations.

The following are the modifications performed to extend the solvers capability to robustly handle numerically difficult operating conditions,

1. Variable time interval

   The Courant number, C, and the grid size are specified and the time interval, Δt, is now computed from the following relation.

$$\psi = \frac{|u| + a}{\Delta x} + \frac{|m_b|}{\Delta x \rho_c A}$$

$$\Delta t = \text{MIN} \left(C_0 \frac{2}{\psi + \sqrt{\psi^2 + 4\left(\frac{|f_x| + |f_\theta|}{\rho_c \Delta x}\right)}} \right) \forall x \tag{72}$$

   $C_0 = 0.45$ for our calculations. The Courant number C is revised to account for the source terms. Thus a conservative time interval is computed when the forcing terms are large or when bleed mass is present.

2. First order scheme

   A first order discretization of the conservative variables is chosen to diffuse numerical oscillations. The grid size is sufficiently refined to preserve the accuracy of the physics. The Euler equations do not contain any viscous terms and apply no numerical smoothing (artificial viscosity). The first order scheme is applied for dissipation

of steady high wave number oscillations which have wavelengths comparable to grid spacing, and which are solutions of the finite difference equations, but not of the partial differential equations. These waves can amplify and lead to instabilities. Thus the conservative terms as defined in Eq. 67 become,

$$v^{+}_{j+1/2} = v^{n}_{j+1} \quad v^{-}_{j+1/2} = v^{n}_{j}$$

3.5 Coupling Framework

The equations and associated boundary conditions for the continuous and discrete phases are resolved in a two-step process that lead to a coupled formulation. The first step involves solving the governing equations for the continuous phase (Eq. 38) to calculate the conservative flow variables in vector $\mathbf{V}$.

In the second step, the results of the computations for the continuous phase are then passed as inputs to solve Eqs. (22)-(29) for the discrete phase. The mass, momentum and energy source/sink terms ($\mathbf{Q}_{\text{blade}}$, $\mathbf{Q}_{\text{bleed}}$ and $\mathbf{Q}_{\text{discrete}}$) for the humid air and discrete phase are then updated using Eqs. (41) and (42) and applied in the next time step. The time steps are first run in dry conditions until the initial transients decay and the compressor reaches a steady state operating point. Then a steady ice flow rate is introduced in the compressor airflow. The ice flow influences the fluid flow characteristics of the compressor.

The present work develops a quasi-one-dimensional unsteady model to investigate the impact of ice ingestion on the flow in a typical gas turbine engine compressor. It demonstrates the treatment of coupling between the continuous (air) and discrete (ice crystals and water droplets) phases. The flow chart for the numerical scheme is shown in Fig. 16.

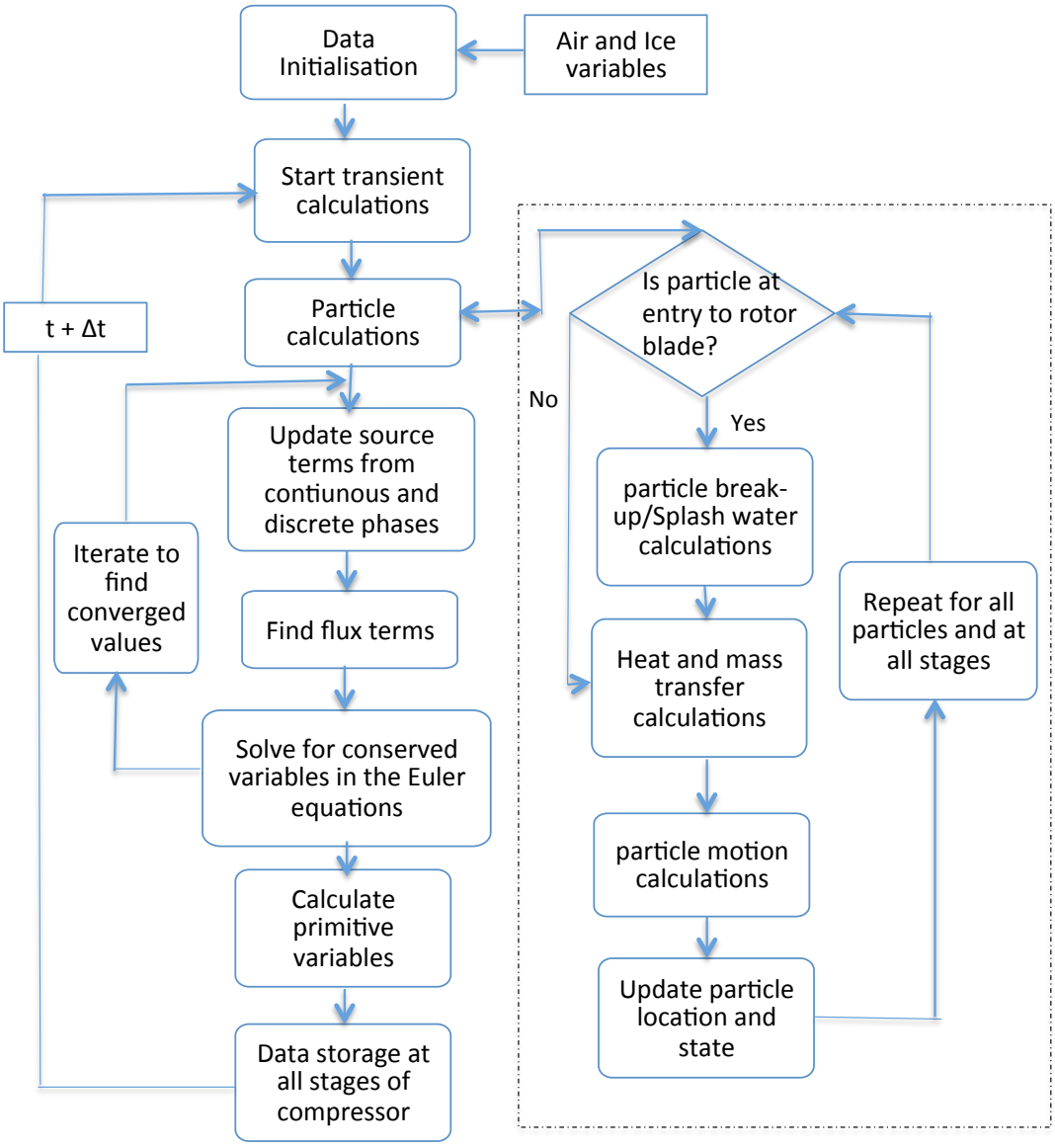

Figure 16: Flow diagram for numerical scheme

CHAPTER IV

VALIDATION

The present study investigates icing induced stall of the compressor at nominal and ground idling operating speeds. These results rely on an axisymmetric one-dimensional unsteady fluid dynamics solver that is capable of handling all operating conditions (except post-stall operation). In order to establish the fidelity of the solution predicted by the numerical model, the results of the steady state and stall analysis are compared to the measured performance of the compressor. The validation of the stalling stage was previously performed by Dhingra et al. [24] for a ten stage compressor, between experimental data and the solver used in the present work. It is detailed in the Appendix A. This chapter covers the validation of the surge point predicted by the solver for a four stage axial compressor, with experimental data. The four stage compressor has a different geometry as compared to the ten stage compressor.

4.1 Compressor performance analysis for a four stage axial compressor

The compressor operation is simulated for 95% and 100% speeds with performance maps constructed from test data for a four stage axial compressor. Fourteen different operating points consisting of pressure, temperature and velocity readings are given for each of the speeds.

In the simulation, an operating point is shifted along a fixed speed characteristic by the setting of a downstream throttle valve. The flow conditions are slowly driven towards stall. Thus the stall pressure and stalling stage of the given multistage compressor are determined for validation.

This validation study is important in determining the robustness of the solver to different operating speeds and to compressor geometry. The solver's accuracy in simulating the compressor steady state operation is verified and the detection of the stalling stage from pressure transients is attempted.

4.1.1 Compressor performance analysis at 95 % speed for a four stage compressor

4.1.1.1 Operation in stable non-stalled regime

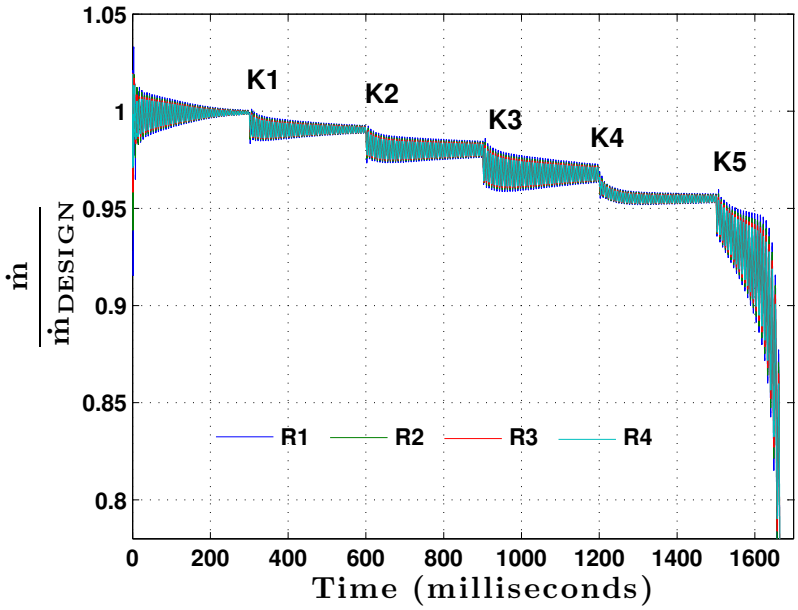

Figure 17: Mass flow rate through time for 95% speed with reflecting boundary conditions.

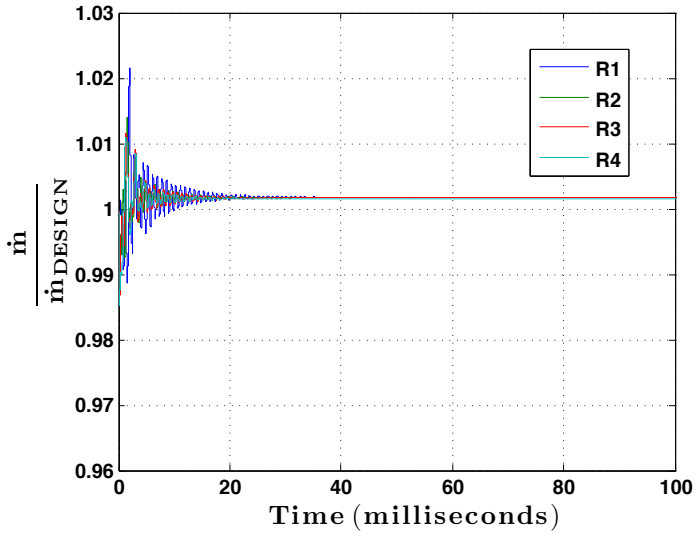

Figure 18: Mass flow rate through time for 95% speed with a nonreflecting boundary condition and a plenum volume applied. Fast attenuation of the flow transients take place in the first 30 milliseconds of compressor operation

In these simulations, the compressor inlet stagnation pressure and temperature are held constant. Method 1 as detailed in Chapter 3, Section 3.3 is used for inlet boundary condition (reflecting boundary conditions). The exit boundary condition is also as specified by Method 1 in Chapter 3, Section 3.3 (reflecting boundary). A throttle on the compressor discharge side is used to vary the back pressure of the compressor, and thereby the mass flow rate and pressure ratio across the stages. The Method 2 with nonreflecting boundary condition including a plenum volume usually gives a better attenuation of flow transients (Fig 18). However, the reflecting boundary condition (Method 1) is used for all the results related to 95% operating conditions.

Figure 17 shows the change in mass flow rate with time as the throttle is being closed until the stall margin is crossed. The compressor simulation at operating points from 9 to 14 are all stable. In order to capture the stall point, the simulation in started at the 9th operating point. The operating conditions at the 9th operating point are designated as the design point conditions. The plots for 95% speed data are normalized with these values. The steady mass flow rate at the throttle point K_1 is at the 9th operating point. Once the throttle is changed the system is given an appropriate time to stabilize to a steady operating condition, as portrayed in Fig.17.

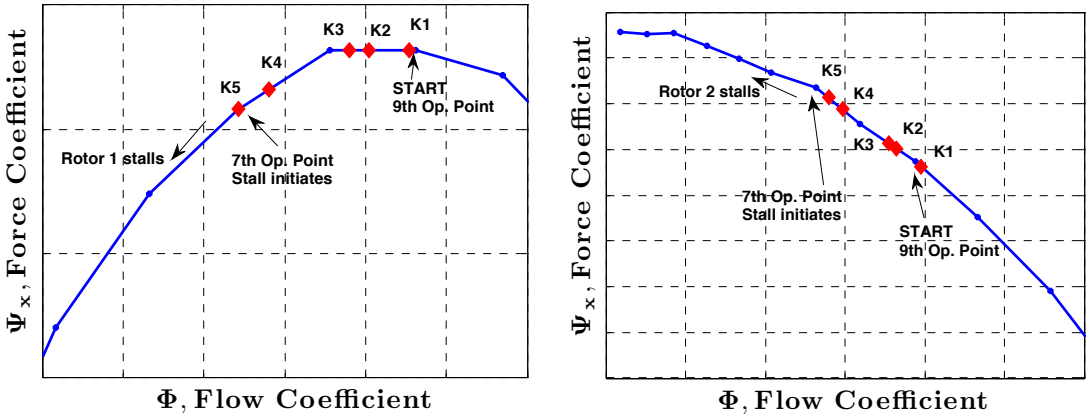

(a) Rotor 1 (b) Rotor 2

Figure 19: Stage-wise behavior of axial force coefficient for rotors 1 and 2. The diamonds mark the stable equilibrium conditions after every throttle application.

The shift of stable operating conditions denoted by K_1 to K_5, towards stall are recorded

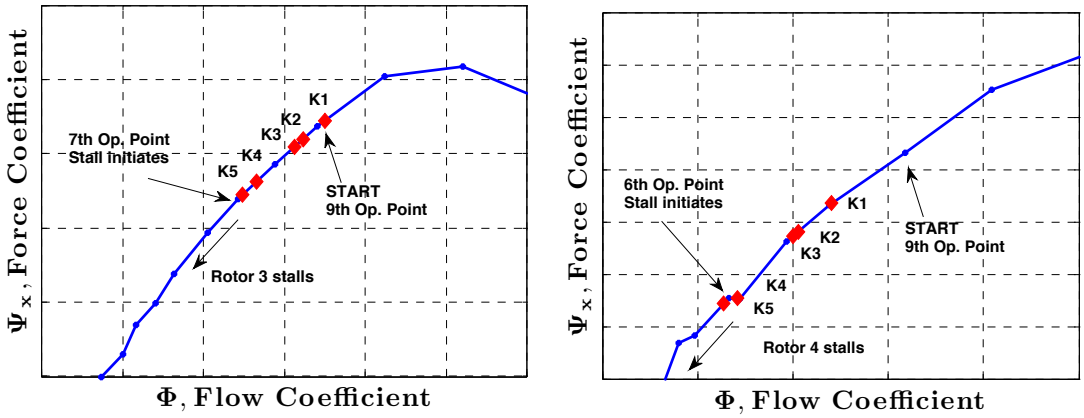

(a) Rotor 3 (b) Rotor 4

Figure 20: Stage-wise behavior of axial force coefficient for rotors 3 and 4. The diamonds mark the stable equilibrium conditions after every throttle application.

on the characteristic maps of rotors 1 to 4 in Figs. 19 and 20. The compressor stalls around the 7th operating point. The mass flow rate shows a drop at 1600 milliseconds on application of the last throttle change at K_5.

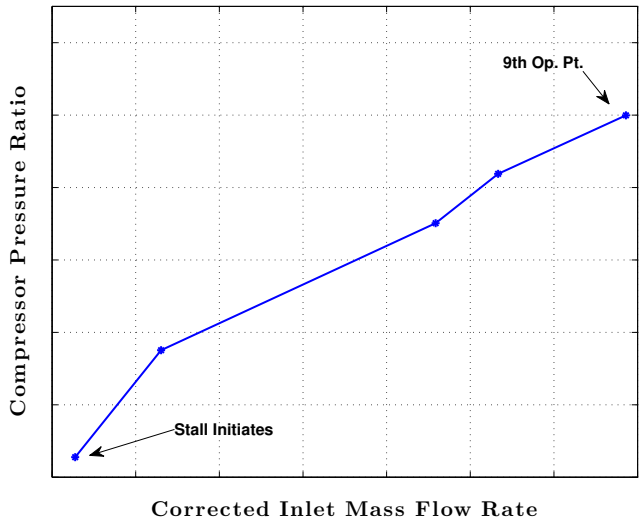

Figure 21: Compressor pressure ratio for 95% speed with changing throttle conditions.

The compressor overall stagnation pressure ratio is shown in Fig. 21. The overall pressure drops as the compressor is throttled to stall. The compressor crosses the stall limit

around the 7th operating point. The final pressure ratio and mass flow rate attainable before stall is obtained. These are the surge points that are compared with the experimental data.

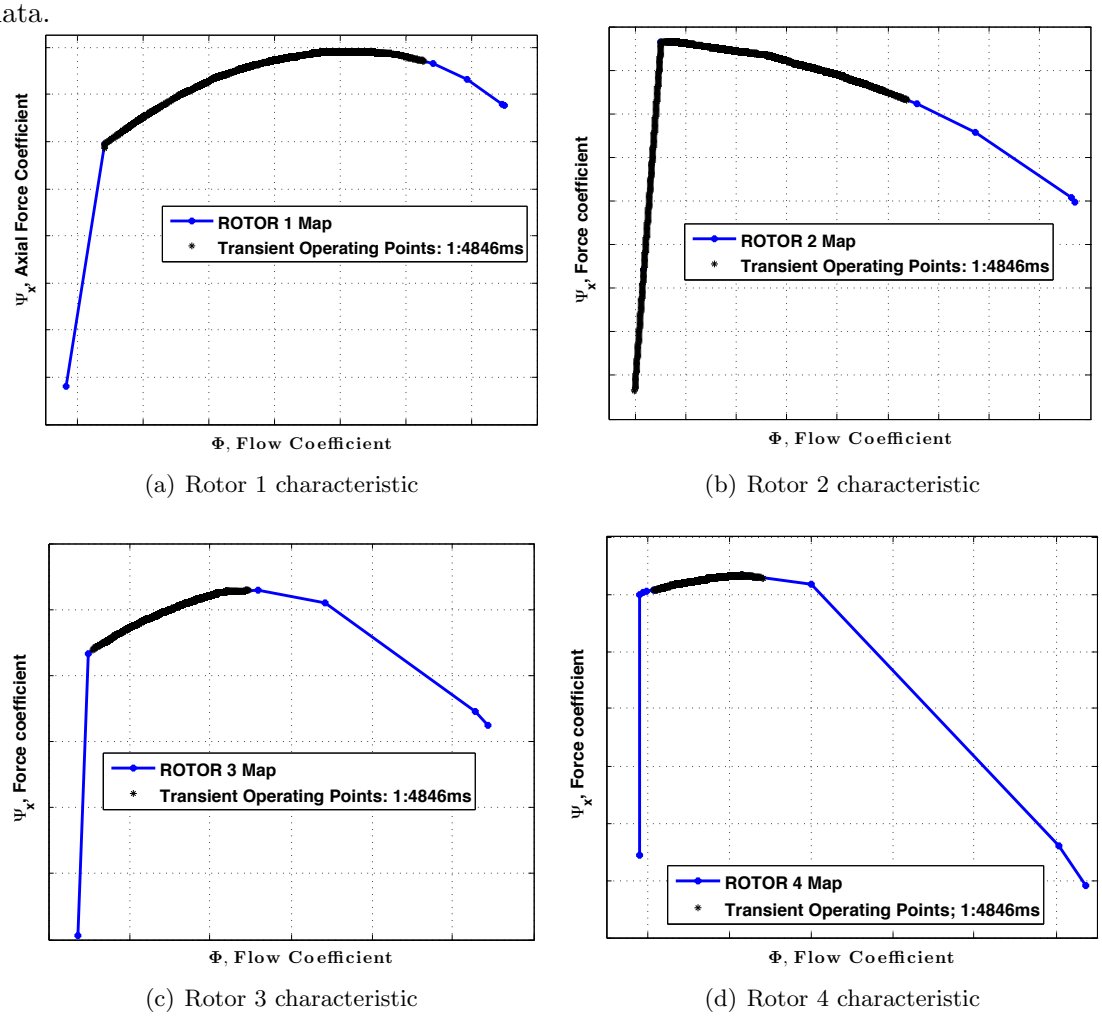

(a) Rotor 1 characteristic

(b) Rotor 2 characteristic

(c) Rotor 3 characteristic

(d) Rotor 4 characteristic

Figure 22: Black points mark the transient operation at the Rotors 1 to 4 respectively, as the compressor is throttled till it reaches stall.

4.1.1.2 Slope Modification in the stalled regime

The manufacturer has provided a sequence of artificial steady state data points on the stall side. The compressor operation in the stall regime is manifested in a gradual decaying of pressures that follow the characteristic map. On application of the last throttle, K_5 in Fig. 17, the compressor exhibits a gradual decay of the mass flow rate indicating a global stall. The operation no longer comes to a steady equilibrium point in this regime. In order

to demonstrate a radical drop in pressure indicating a deep stall, an artificial steep slope is introduced at the end of the each of the rotor force characteristic maps. This can be noted from Fig. 22. Any unsteady flow oscillations in the stalled regime that reaches this part of the map will display a clean sharp stall characteristic. The transient operation of the rotor that is the first to hit this boundary will collapse and trigger fast stall. It will load up the upstream stages while unloading the downstream stages. Black markers indicate the transient operation from the start of the compressor operation to 4846 milliseconds, prior to the collapse of the entire compressor operation.

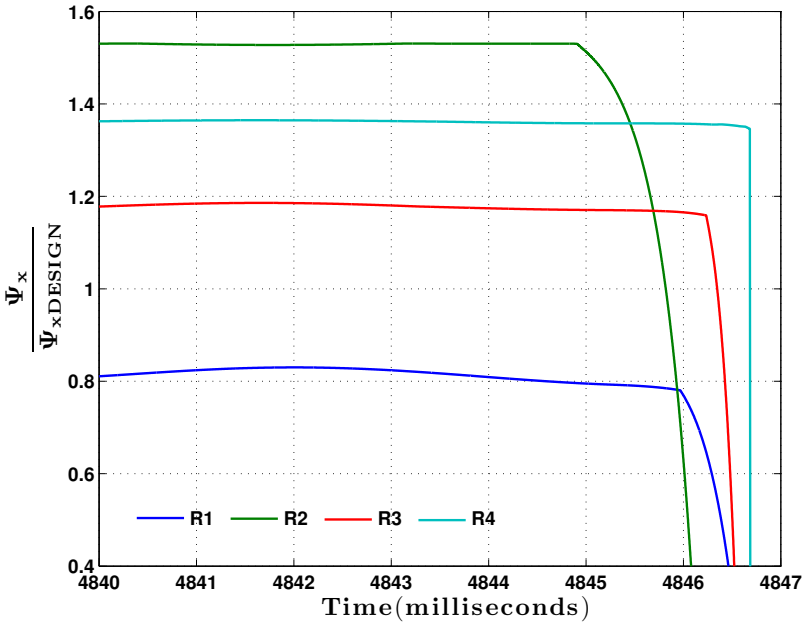

Figure 23: Axial force coefficients prior to stall for 95% speed displaying the order in which the stages collapse.

4.1.1.3 Stalling stage for 95% *speed*

The simulation for 95% speed is repeated with longer time periods in between each throttle. A throttle is applied incrementally. This ensures that the stalling conditions are very closely captured. The transient operation of the rotors starting from 10th steady state operating point is recorded on each of the rotor characteristic maps in Fig 22. The operation shifts as the throttle is closed. Eventually, pressures and mass flow rate oscillations begin when

the compressor crosses the stall point. The transients until the time instant when the oscillations reach the steep slope of the map (4846 milliseconds) is recorded with black markers in Fig. 22. The unsteady pressure oscillations indicate a global stall. However, a local instability at a weak stage causes the compressor to fail. It is evident from Fig. 22(b) that rotor 2 oscillations are the first to cross over the sharp slope of its characteristic map.

The force characteristics are also useful in determining the sequence in which the stages stall. The advance of the oscillations on the maps are an indicator to the rotors that are closer to complete instability. Figure 23 plots a snapshot of the transient variation of the force coefficients for each of the rotors prior to stall. It is noted that rotor 2 force coefficient is the first to drop. Rotor 1 follows rotor 2 closely. Eventually, rotors 3 and 4 collapse.

4.1.1.4 Pressure time history to detect stage that triggers stall

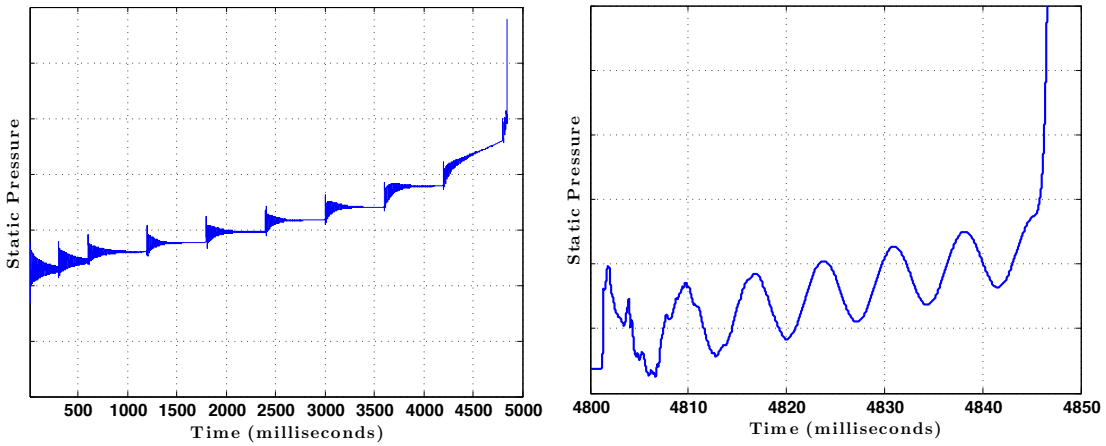

(a) Complete pressure time history

(b) Pressure time history showing stall

Figure 24: Time history of static pressure at Rotor 1 inlet.

Figures 24 - 27 show the pressure fluctuations with throttle changes recorded at the inlet of each rotor blade row. The complete time histories presented in Figs. 24(a) - 27(a) show that initially the pressure increases gradually. This region is in the non-stalled regime. As the throttle is increased beyond a certain limit there is an abrupt change in the pressure. The compressor is said to have stalled. The pressure time history from 4800 to 4850 milliseconds plotted in Figs. 24(b) - 27(b) is used to detect the stalling stage.

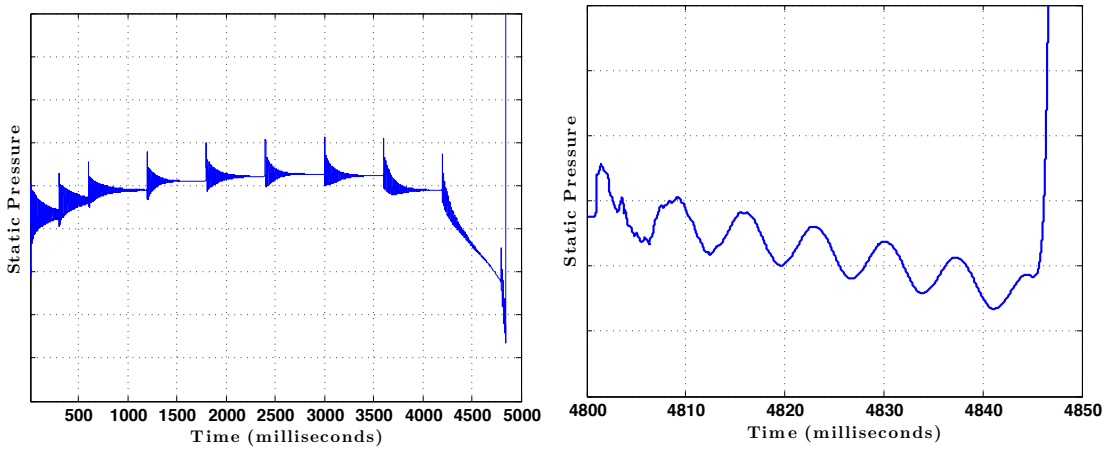

(a) Complete pressure time history (b) Pressure time history showing stall

Figure 25: Time history of static pressure at Rotor 2 inlet.

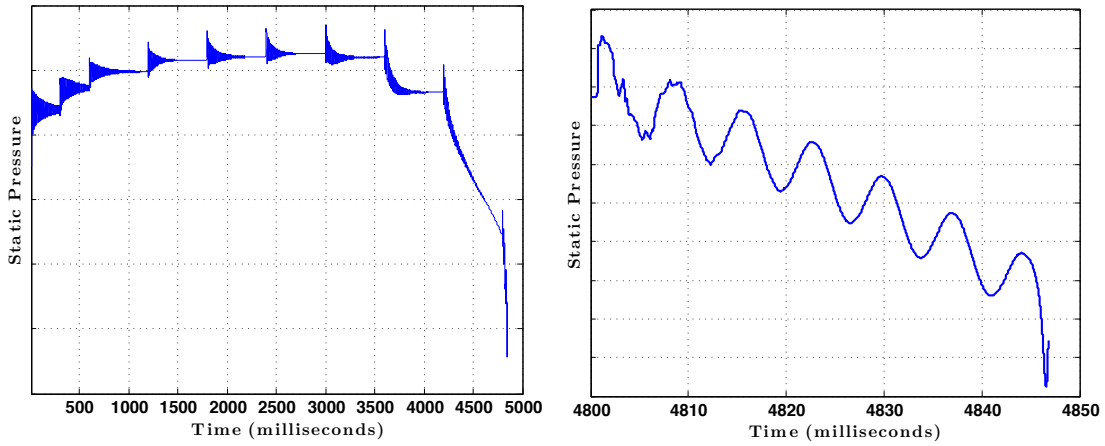

(a) Complete pressure time history (b) Pressure time history showing stall

Figure 26: Time history of static pressure at Rotor 3 inlet.

The stall predicted by the solver is an irreversible disturbance and once formed it leads to a collapse of the pressure rise across the compressor. The stalling point is where the throttle characteristic is tangential to the compressor map. Any small reduction in mass flow rate makes the compressor unstable as shown in the illustration in Fig. 17. The stall occurs when the compressor can no longer handle the increased pressure rise required by the downstream throttle. As the compressor enters into a slow global stall, one of the stages collapses abruptly. Once the stage fails, a sharp compression wave originates from the stage and moves upstream towards the inlet and an expansion wave simultaneously emanates and

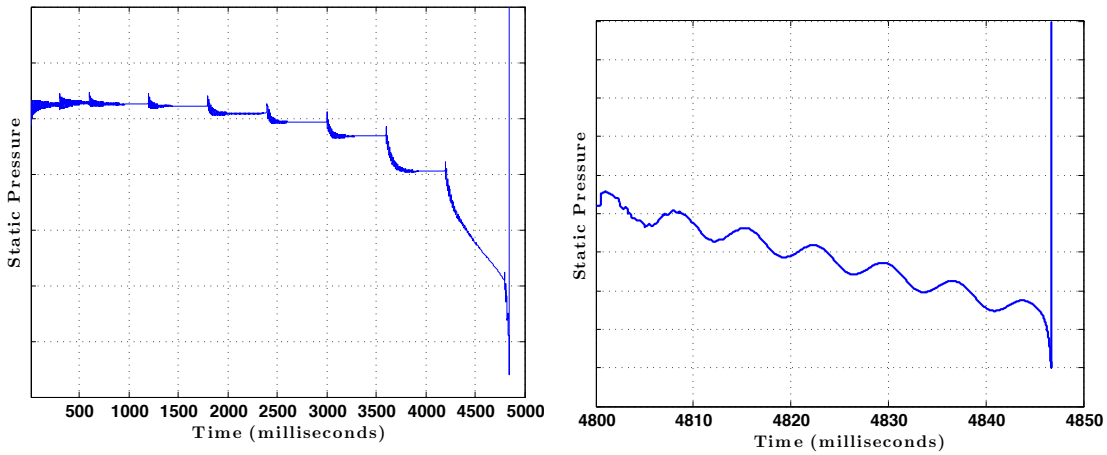

(a) Complete pressure time history

(b) Pressure time history showing stall

Figure 27: Time history of static pressure at Rotor 4 inlet.

moves downstream towards the exit. It is deduced from Fig. 23 that stage 2 is the first stage where local instability is initiated. Thus a pressure jump due to compression wave generated by rotor 2 that has travelled upstream is noted in Fig. 24(b) showing the transient pressure variation at rotor 1. The pressure jump is also conspicuous in the rotor 2 time history in Fig. 25(b). Meanwhile, the expansion wave emanated by rotor 2 and traveling downstream is recognized in the pressure history in Figs. 26(b) and 27(b) for rotors 3 and 4, respectively.

It is concluded that the compressor stable operation regime is above the 7th operating point, and the stall gets initiated at rotor 2 for the compressor operation at 95% speed.

4.1.2 Compressor performance analysis at 100 % speed for a four stage compressor

A throttle on the compressor discharge side is used to vary the back pressure of the compressor, and thereby the mass flow rate and pressure ratio across the stages for 100% speed. Method 1 detailed in Chapter 3, Section 3.3 is used for the inlet boundary condition. Method 2 is used for the exit boundary condition. A nonreflecting exit boundary condition is imposed and the throttle application has a finite time lag.

Figure 28 shows the change in mass flow rate with time as the throttle is being closed. The compressor simulation at operating points from 11 to 14 are all stable. In order to

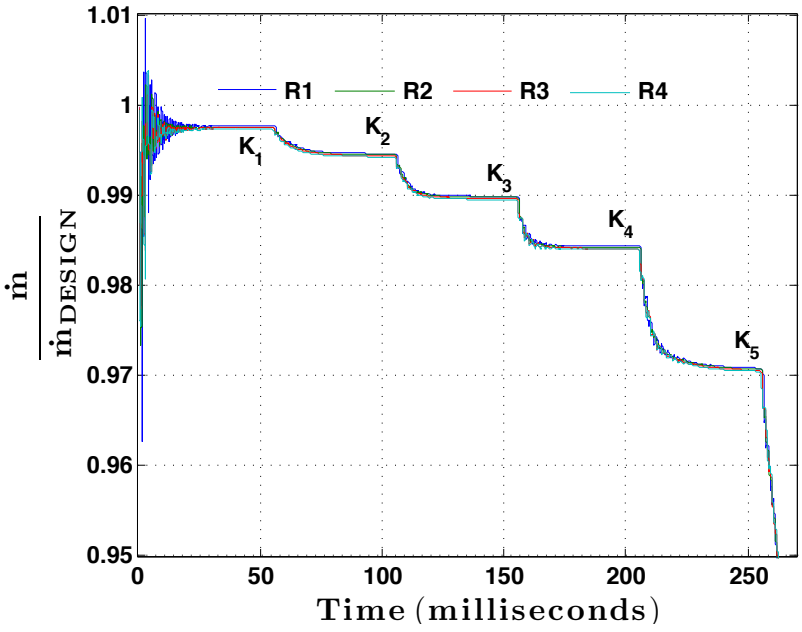

Figure 28: Mass flow rate through time for 100% speed

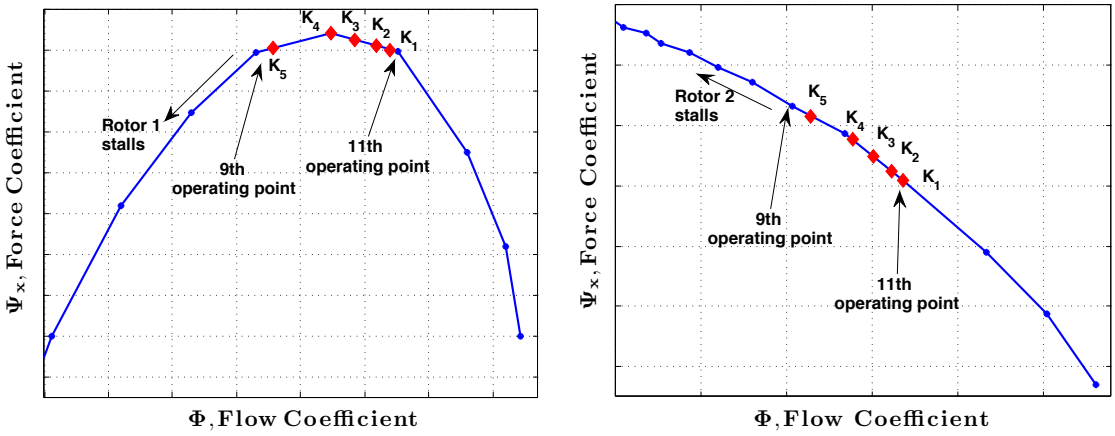

(a) Stage 1 (b) Stage 2

Figure 29: Stage-wise behavior of axial force coefficient. The diamonds mark the stable equilibrium conditions after every throttle application.

capture the stall point, the simulation is started at the 11th operating point. The operating conditions at the 11th operating point are designated as the design point conditions. The mass flow rate is again throttled to stall.

Figures 29 and 30 show the shift of the corresponding stable operating conditions denoted by K_1 to K_5, towards stall. Eventually the compressor stalls around the 9th operating point. The mass flow rate shows a drop at 250 milliseconds on application of the last throttle

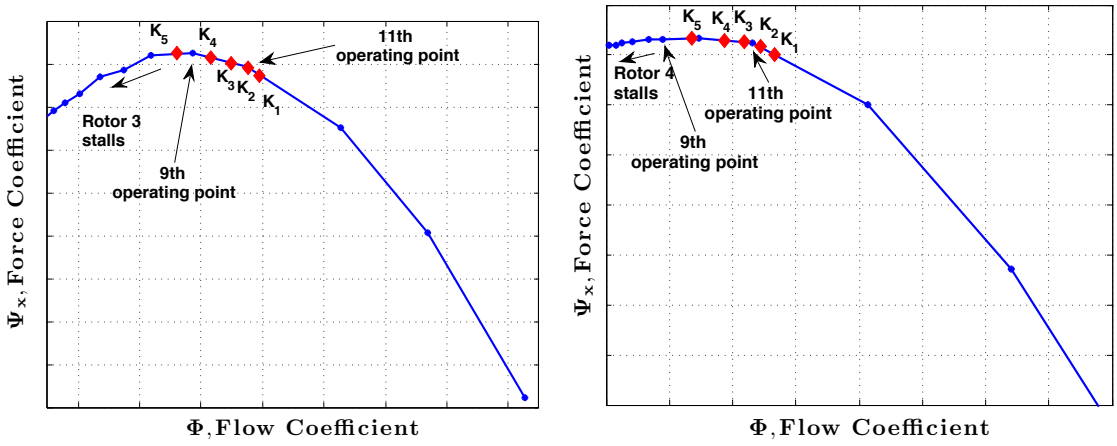

(a) Stage 3 (b) Stage 4

Figure 30: Stage-wise behavior of axial force coefficient. The diamonds mark the stable equilibrium conditions after every throttle application.

at K_5.

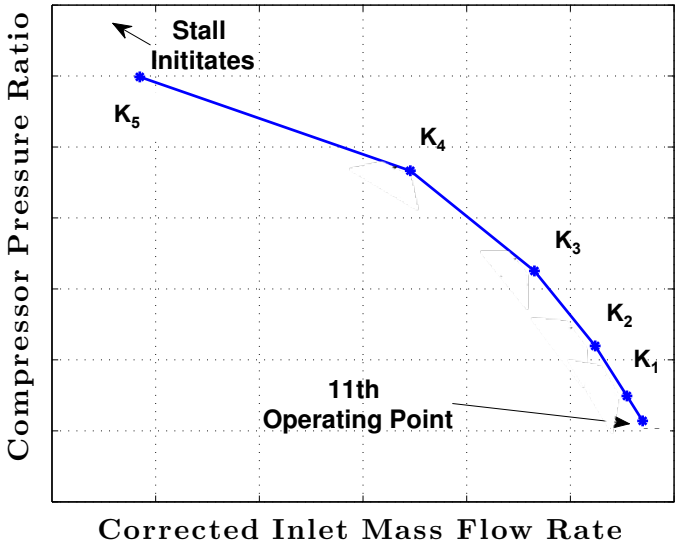

Figure 31: Compressor pressure ratio for 100% speed with changing throttle conditions.

The compressor overall stagnation pressure ratio is shown in Fig. 31. The overall pressure rises as the compressor is throttled to stall. The compressor crosses the stall limit around the 9th operating point. The maximum pressure ratio and mass flow rate attainable before stall are obtained. These are the surge points that will be compared to the experimental data.

This simulation does not capture the stalling stage for 100% accurately. The initial trend

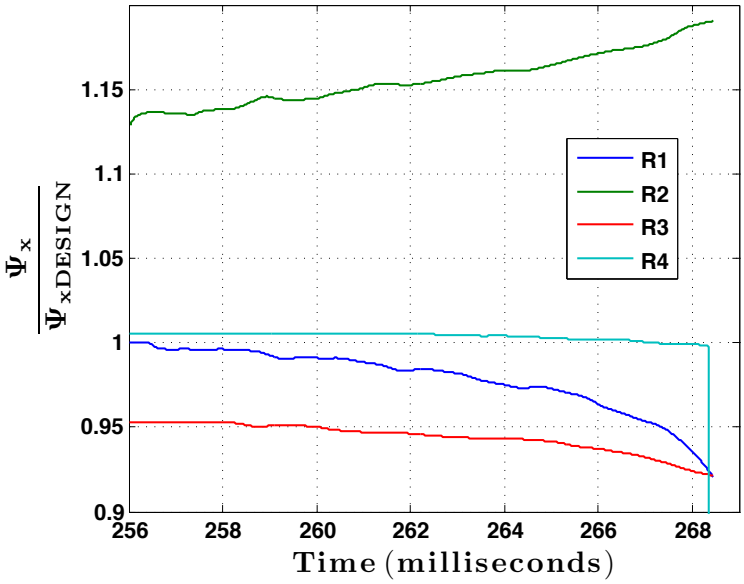

Figure 32: Axial force coefficient for 100% speed in the stall regime.

in Fig. 32 highlights rotor 2 as the blade row that would cause the system to ultimately collapse. Yet, rotor 4 is the first to collapse after 268 milliseconds as depicted in Fig. 32. Also, the subsequent collapse of the upstream stages is not obtained from this simulation. The operating points in the post-stall region of the given data for Stage 4 are highly erratic. The foray of the transient operation beyond 250 milliseconds in the post-stall region of rotor and stator 4 may have caused a false collapse of stage 4. A further investigation of the given data in the stalled region is needed in order to accurately detect the stalling stage.

4.1.3 Validation of simulation for a four stage compressor with experimental data

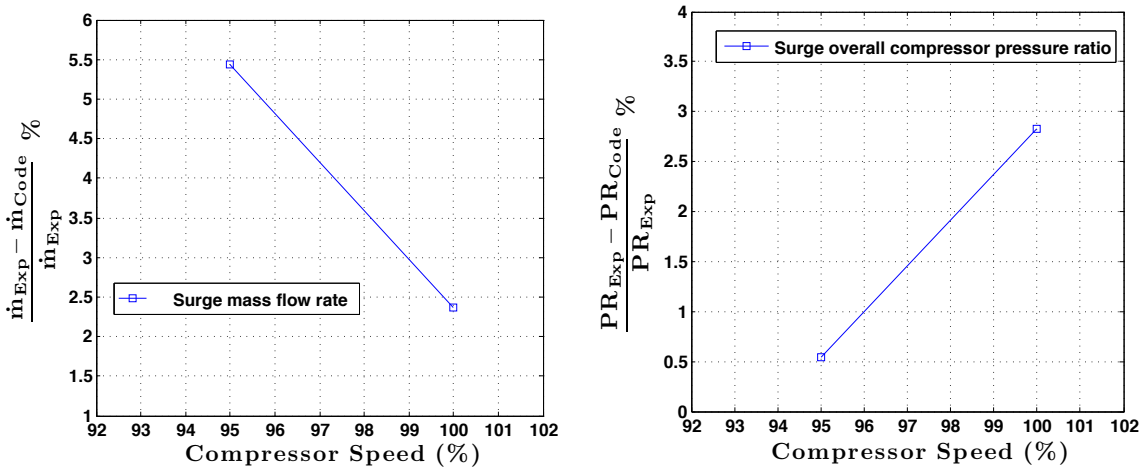

(a) Mass flow rate at surge

(b) Overall pressure ratio at surge

Figure 33: Validation of surge points with respect to experimental data

The surge points from experimental data are compared to that obtained from the computational solver. Figure 33(a) plots the mass flow rate obtained before the compressor stalls for 95% speed (Fig. 17) and 100% (Fig.28), as a percentage difference from the experimental mass flow rates. The match is within a 5% range.

Figure 33(b) plots the overall pressure ratio before stall occurs in the simulation for 95% speed (Fig. 21) and 100% speed (Fig. 31), as a percentage difference from the experimental surge pressure ratio. The match is within a 3% range.

CHAPTER V

IMPACT OF ICING ON COMPRESSOR FLOW DYNAMICS

The effect of ice ingestion on the gas flow through the compressor is explored. Section 5.1 first establishes the importance of a coupled analysis between the air and discrete phase. Next, the variation of fluid flow variables such as pressure, temperature, density and velocity, across the compressor is compared between dry and humid air operating conditions for a single ice flow rate. It is of interest to evaluate the change in flow response with increasing ice flow rates and compare the performance impact at both high and low speed operations of an engine compressor. To this end, Sec. 5.2 discusses the performance and stall analysis of a compressor operating at nominal speed and loading conditions. This corresponds to a 98% inlet corrected speed that is close to cruise and take-off conditions. Section 5.3 investigates the flow behavior at ground idling speed which is at 65% inlet corrected speed. Section 5.4 summarizes the findings for the low and high speed operations. Finally, Sec. 5.5 compares the effects due to ice ingestion with that of wet compression effects.

5.1 Performance analysis of dry air and humid air operation

This section presents a comparison between the steady state dry operation of the compressor with the altered compressor operation in the presence of a steady ice flow rate. A ten bin Rosin-Rammler ice crystal distribution with 175 µm mean value diameter is selected. Lawson et al. [51] provides meteorological data with modal diameters of ice particles in the outlying areas of thunderstorms. The input parameters are as detailed in the Table 3. The dry air operation of the compressor is started and allowed to stabilize for the first 60 milliseconds. A steady flow rate of ice is then introduced where the discrete phase is assumed to flowing in at 1/10th the speed of the incoming dry air. The coupled steady state behavior of the flow is first investigated, followed by an analysis of the transient response of the compressor flow.

Table 3: Compressor variables for performance comparison between dry and humid air operation at ground idling conditions.

Parameter	Value
Corrected operating speed	Ground idling (68%)
% $\dot{m}_{ice}$	0.47% of dry air

5.1.1 Coupled framework significance in presence of a discrete phase: Pressure and temperature profile response

The icing physics model is best understood by comparing the "frozen field" or "one-way coupling" results to the results obtained when a "two-way coupling" is implemented. In a frozen field, any changes in the discrete phase do not affect or update the properties of the surrounding continuous phase, so that a one-way coupling is exercised. For a two-way coupled multiphase flow there is a mutual effect between the different phases. The equations that govern the compressor flow field and the icing physics are coupled as the phase changes in ice and water molecules modify the characteristics of the surrounding air phase. The vapor produced by the droplets is a mass source for the fluid. Also the vaporization process generates modifications in the momentum and energy balances between both phases [6]. These modify the temperature and pressure variation through the compressor as illustrated in Figs. 34 and 35, which are input terms to the governing equations for the discrete phase.

The impact of coupling between the discrete and continuous phases is analyzed by examining the static temperature and pressure variation across the compressor predicted by the model as illustrated in Figs. 34 and 35. The results are normalized with stagnation values at the inlet. Likewise, the axial location is normalized by the total length of the compressor. In all the icing simulations the mass flow rate of the dry air is specified at the start of the simulation. The flow conditions are modified as ice particles are ingested when the compressor simulation is run.

The heat lost by air due to interactions between the air flow and ingested ice crystals, water droplets, and vapor, is manifested as a drop in the temperature as compared to the dry air results (Fig.34). The reduction in temperature is highest when there is a two-way

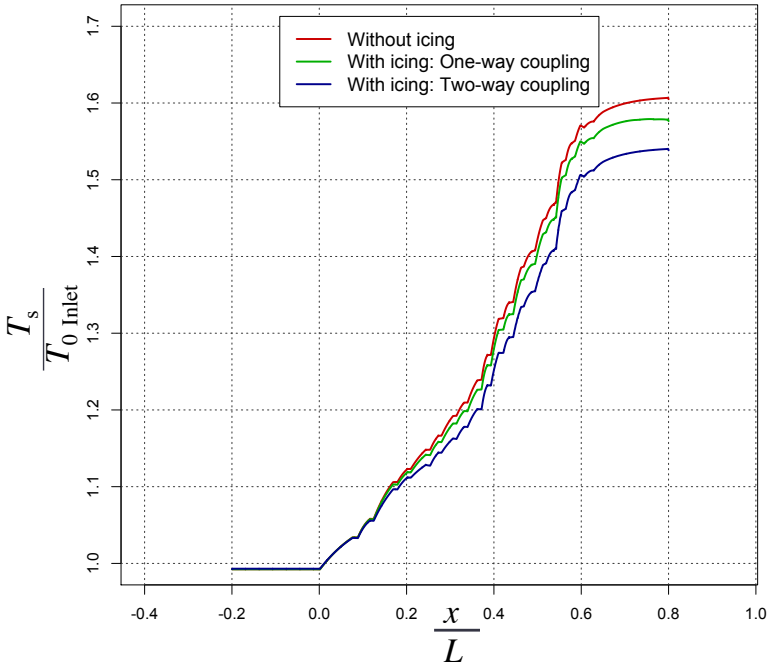

Figure 34: Temperature profile for gas through compressor with one-way and two-way coupling respectively

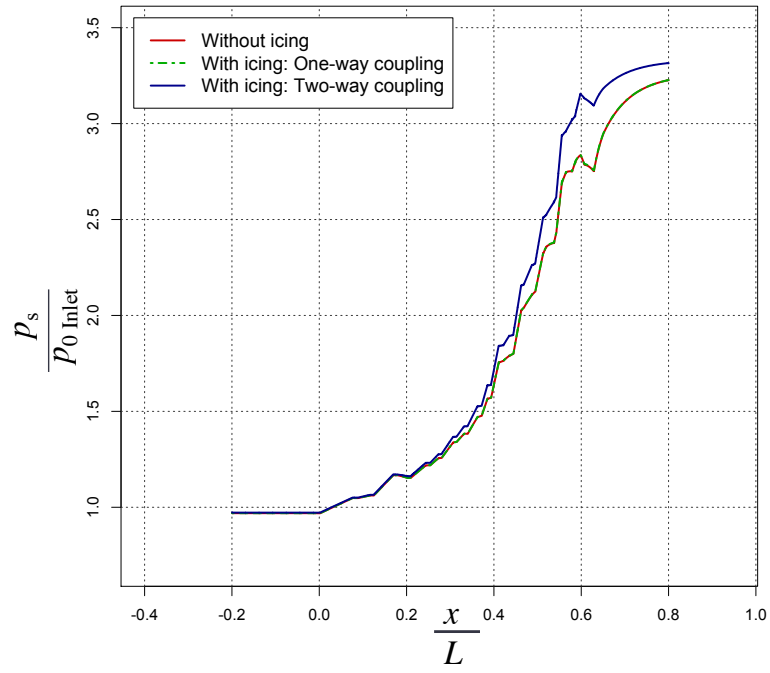

Figure 35: Pressure profile of gas through compressor with one-way and two-way coupling respectively

coupling between the air and the discrete phase.

The pressure variation with axial location (Fig.35) for a flow with one-way coupled icing model appears similar to the dry air pressure rise through the compressor, indicating that ice ingestion does not impact the pressure variation in the compressor. However, the two-way coupling implementation has a distinct rise in pressure as compared to that of dry air, especially at the rear stages due to mass addition.

The pronounced response emphasizes the impact of two-way coupling in the prediction of the behavior of the compressor flow field. The analysis based on one-way coupling is shown to underscore the necessity of the two-way coupling methodology.

5.1.2 Transient temperature and pressure response for a 0.47% ice flow rate

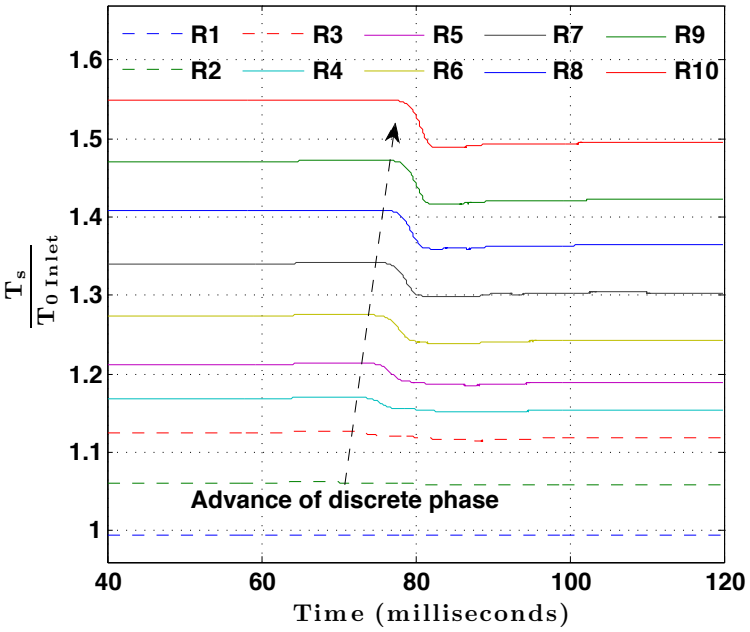

Figure 36: Transient temperature response.

Figures 36 and 37 depict the transient static pressure and temperature variations at the inlet of each of the ten rotor blade rows. The transient simulation for dry air is run until the solution converges to a steady state. Ice crystals are then introduced after 60 milliseconds in a continuous steady stream. The ice crystals manifest themselves as a disturbance in the flow.

The temperature time traces, as seen in Fig. 36, indicate the progression of ice particles

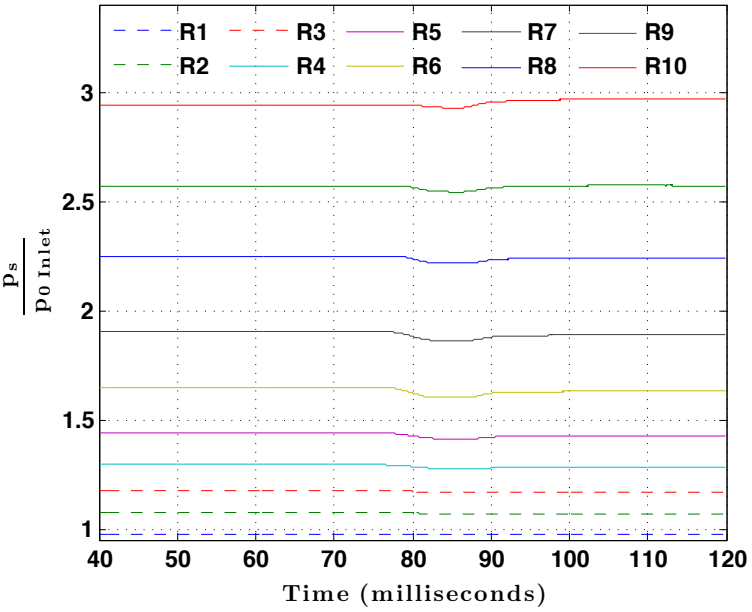

Figure 37: Transient pressure response.

through the compressor. As the ice moves through the inlet duct, the temperature falls at each consecutive station in response. There is a finite delay in the temperature drop from one stage to the next. This is consistent with transport delay - the finite time taken by a particle to travel from one stage to the next. Initial stages have a greater concentration of ice while the later stages have higher water content. Note that enthalpy of evaporation is higher than the latent heat absorbed by melting ice, leading to a steeper drop in temperature of the airflow through the compressor in the later stages.

The pressure time traces depicted by Fig. 37 also show a transient change in compressor response to the presence of ice that illustrates an eventual increase in overall pressure ratio. This behavior can be attributed to the off-design stage behavior of the compressor flow field. Cumpsty [18] explains the challenge of stage-wise matching of a multistage compressor. The compressor is designed to operate at a design or matching point, where the outlet flow conditions of one stage fit the inlet conditions of the next stage and each individual stage operates at its design point. However, ice ingestion induces a change in interstage flow response that result in stage rematching. The off-design performance is explained in Section 5.3 for performance and stall analysis of humid air with increasing ice flow rates at

idling speed operation.

5.1.3 Transient density, mass flow rate and velocity response for a 0.47% ice flow rate

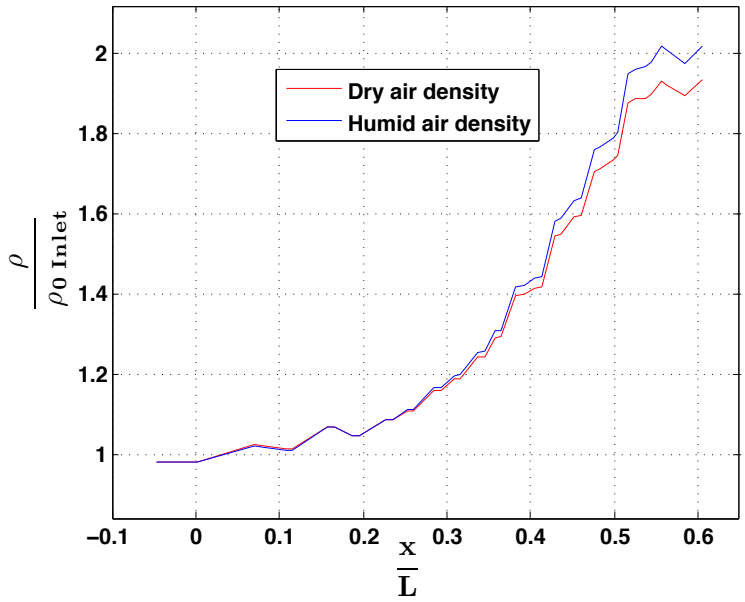

Figure 38: Density profile with and without ice

The temperature reduction at the exit causes a rise in the overall pressure ratio as seen in Fig. 37. The lower temperatures drive the rise in density at the exit of the compressor as shown in Fig. 38.

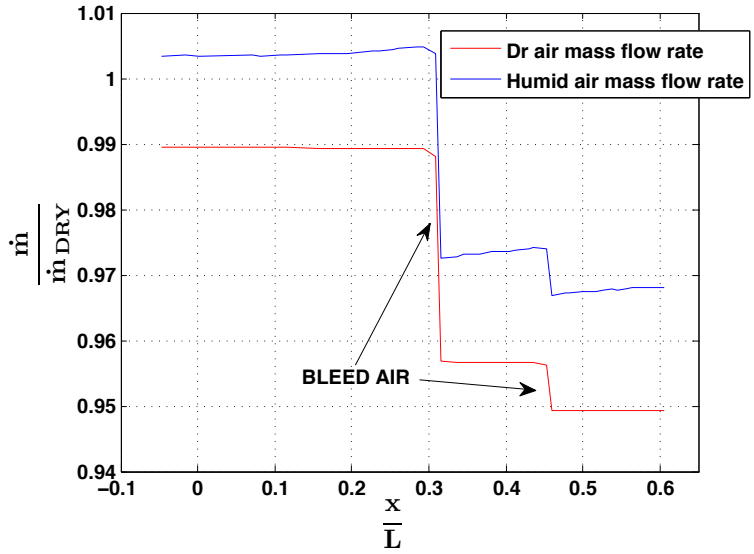

Figure 39: Mass flow rate profile with and without ice.

The computation of mass flow rates from the continuity equation (Eq. 6), accounts for mass of air bled from the compressor and mass of water vapor added due to phase changes. Two distinct drops in the mass flow rate of air plotted in Fig. 39 are due to bleed mass at two different locations. The mass flow rates are normalized with respect to the dry air value.

The throttle position at the end of the compressor is designed for a choked flow condition. A drop in temperature, rise in pressure and an increase in the density at the rear stages during ice ingestion contribute to an overall increased pumping capacity of the compressor. This is clearly observed in the rise of the mass flow rate profile. The concentration of water vapor in air at the initial stages is low. However, the increase in flow rates as the air incorporates the evaporating water is noticeable as a rising slope in the middle stages.

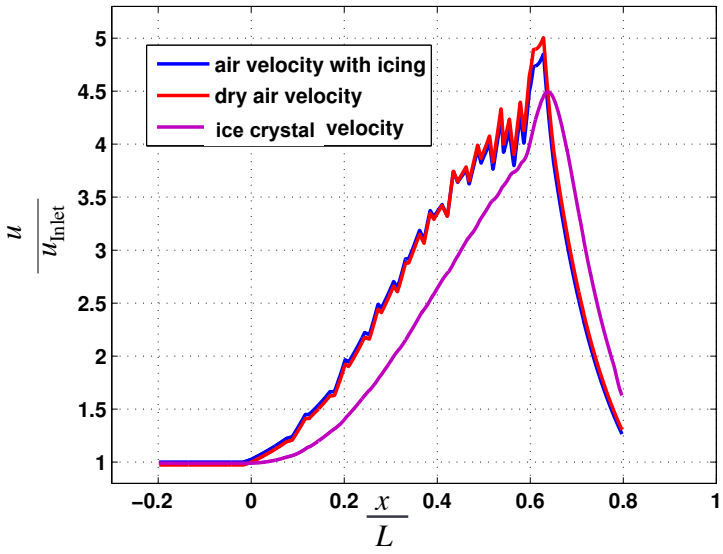

Figure 40: Velocity profile with and without ice

The velocity field in the compressor, as shown in Fig.40, has been normalized with the inlet velocity. The velocity of the continuous phase in the presence of icing decreases slightly at the rear stages as compared to the velocity of dry air for a 0.47%ice flow rate. The impact increases with increasing ice flow rates as will be discussed in the following sections.

The velocity of an ice crystal is contrasted with the velocity of air. Ice particles are assumed to enter the compressor at 1/10th the speed of air. The ice crystal size of 253 microns reaches the velocity of incoming air almost immediately in the inlet duct. However,

it lags behind as the velocity of air increases through the compressor, as a consequence of drag force acting on it. Inertia of the ice crystal accounts for the lag in velocity, as the velocity of air reduces at the diffuser section of the compressor.

5.1.4 Variation of ice crystal diameter

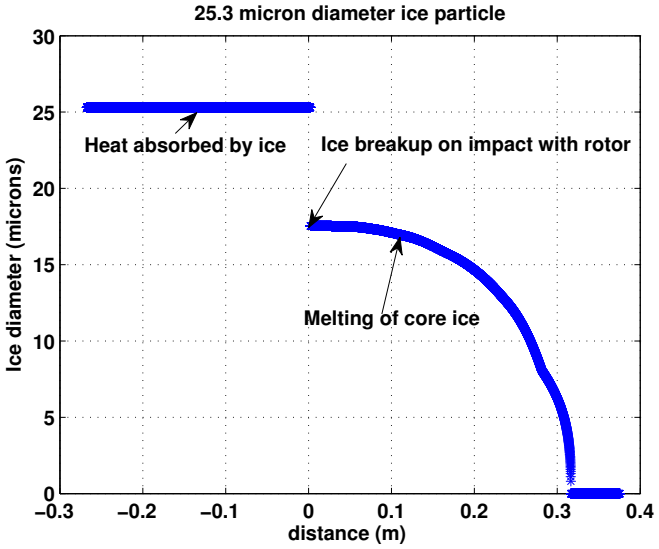

Figure 41: Variation of ice crystal diameter

The variation of ice crystal diameter (initial diameter: 25.3 µm) across the compressor is demonstrated in Fig. 41. The ice crystals are ingested by the jet engine as the aircraft passes through thunderstorm regions. These crystals are at subzero temperatures and act as heat sinks in the compressor flow field. During the period that the ice crystals absorb heat from the surrounding airflow to reach the melting point, their size remains constant. The sudden decrease in diameter illustrated in Fig. 41 occurs due to impact with a rotor blade, where an ice crystal beaks up into multiple ice crystals. After the ice crystal reaches melting point, latent heat is absorbed by the ice crystals to change phase from ice to water and then to vapor. This is exhibited by the slow reduction in the ice core diameter. The equations governing this energy exchange are detailed in Eqs. 30, 31 and 32.

Lou and Hammond [55] detailed equations modeling the heat and mass transfer of ice ingested into the compressor. The presented results for diameter variation of ice particles display a similar trend as in Fig 41.

5.2 Performance and stall analysis of compressor operating at nominal speed and loading conditions

Simulation Procedure: In this section, a stall onset in the compressor due to ice ingestion is investigated by gradually increasing the ice flow into a ten-stage compressor operating at nominal take-off conditions (98% speed). A ten bin Rosin-Rammler ice crystal distribution with 175 µm mean value diameter is selected. The dry air operation of the compressor is started and allowed to stabilize for the first 50 milliseconds. A steady flow rate of ice is then introduced and increased every 50 milliseconds till the compressor stalls. This interval allows the compressor sufficient time to attain a steady operating state, if it exists, for a particular ice inflow rate. The inertial and heat energy lost by the air to the discrete phase and the mass of vapor added to the continuous phase causes the operating point to migrate away from the design value to an off-design pressure ratio.

Brief Analysis: Figure 42 records the transient variation of ice through the inlet of each of the ten stages. Figure 43 shows the corresponding increase in vapor produced as ice gets ingested. The resulting variation of humid air mass flow rate through the compressor is plotted in Fig. 44. The impact on the following humid air flow parameters is analyzed as a percentage difference with the respective dry air values at steady state time instants: (i) mass flow rate (Fig. 45) (ii) temperature (Fig. 46) (iii) density (Fig. 47) (iv) velocity (Fig. 48) and, (v) pressure (Fig. 49). The individual stage response to ice is evaluated from these results. The analysis of the transient pressure response in Fig. 50 demonstrates the loading variation across stages. The stage where stall initiates is detected from the mass flow rate transients preceding instability (Fig. 51). The individual stage response and the stalling stage is corroborated from the shift in the operating point on the individual stage characteristics (Fig. 52). Finally, Fig. 53 shows the increase in compressor overall pressure ratio with increasing ice flow rates. A detailed analysis is presented in the next sections.

5.2.1 Transient variation of the discrete phase through the compressor

Figure 42 records the mass of ice at the inlet of each of the rotor stages in time. This quantity is normalized by the mass of air at the inlet of the compressor. The mass of ice

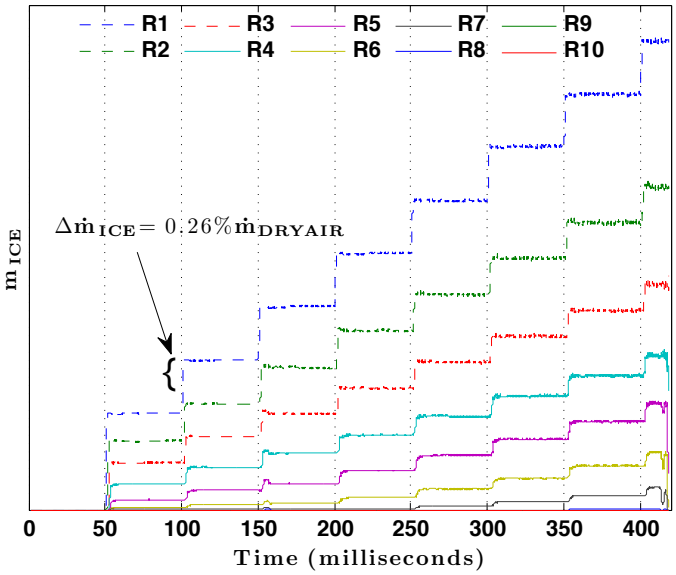

Figure 42: Time traces of ice flow across rotors

reduces through the stages along the compressor due to phase transitions to liquid water and eventually vapor.

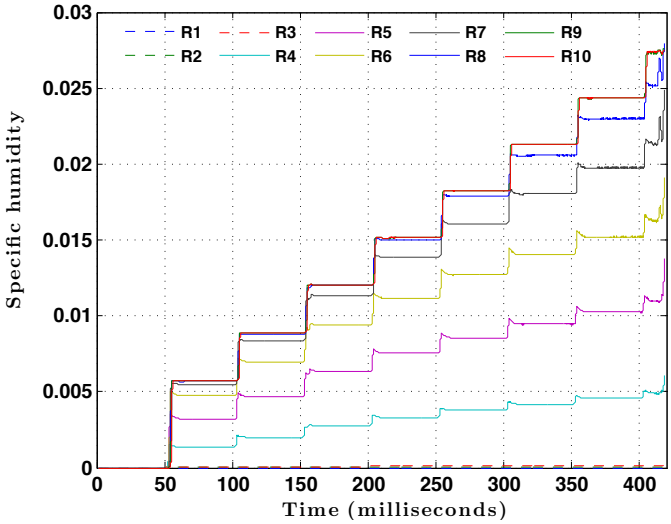

Figure 43: Time traces of specific humidity across rotors

The corresponding increase in the specific humidity (ratio of water vapor to dry air) induced by vaporization of the discrete phase is evident in Fig. 43. The increasing temperature profile (Fig. 36) from the front to the rear stages contributes to a higher phase

transition to vapor at the rear stages. The vapor appears as a source term, s_{vapor}, in the mass continuity equation of humid air (Eq. 6). After a certain duration of compressor operation, the specific humidity reaches a steady value. The water vapor at the compressor exit is an important quantity to note as it impacts the performance of the downstream combustor.

5.2.2 Humid air response to increasing ice flow preceding stall

Transient response of mass flow rate, pressure and temperature across the compressor in the presence of ice are investigated in this section (Kundu et al. [49]).

5.2.2.1 Mass flow rate variation in presence of ice

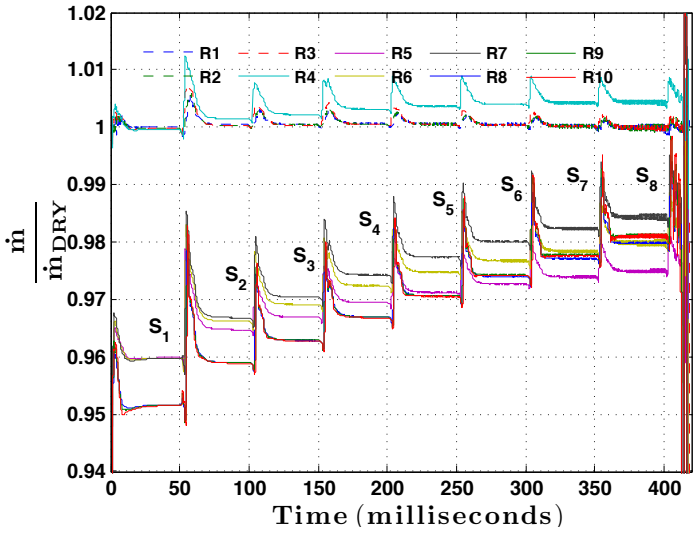

Figure 44: Humid air flow rate at inlet to rotor blade rows with increasing ice flow rates preceding stall instability

Figure 44 presents the variation of gas mass flow rate at the inlet of each of the rotor stages. The two distinct drops in the mass flow rate is due to bleed mass at the aft of the 4th and 7th stages, respectively.The mass flow rate profile across the compressor for dry air and in the presence of a single steady ice flow rate are depicted in Fig. 39. The drop in the mass flow rates corresponds to two bleed ports, one after the 4th stage and the other after the 7th stage, respectively. The transients decay and the dry air reaches a steady state at about 50 milliseconds of the compressor operation. A steady flow rate of

ice is introduced and periodically increased as portrayed in Fig. 42. Dry air mass flow rate is constant through the compressor, obeying the continuity equation. With ice ingestion, source term for vapor s_{vapor} gets added. The gas mass flow rate recorded at the inlet of the rotors increase as seen in Fig. 44, highlighting the increased presence of vapor especially at the rear stages.

The first approximate time when the flow conditions achieve steady dry air operating conditions is denoted by the steady state equilibrium position S_1. S_2 denotes a steady flow condition of the humid air with ice flowing at a rate of 0.74% of dry air. Similarly operating points S_3, S_4, S_5, S_6, S_7 and S_8 denote operating conditions when the flow transients have decayed and an equilibrium has been achieved for ice flow rates of 0.98%, 1.26%, 1.52%, 1.79%, 2.05% and 2.35% of dry air, respectively. The next step increase of ice flow rate to 2.5% of dry air after 400 milliseconds, triggered oscillatory pressure transients, causing an eventual stall instability.

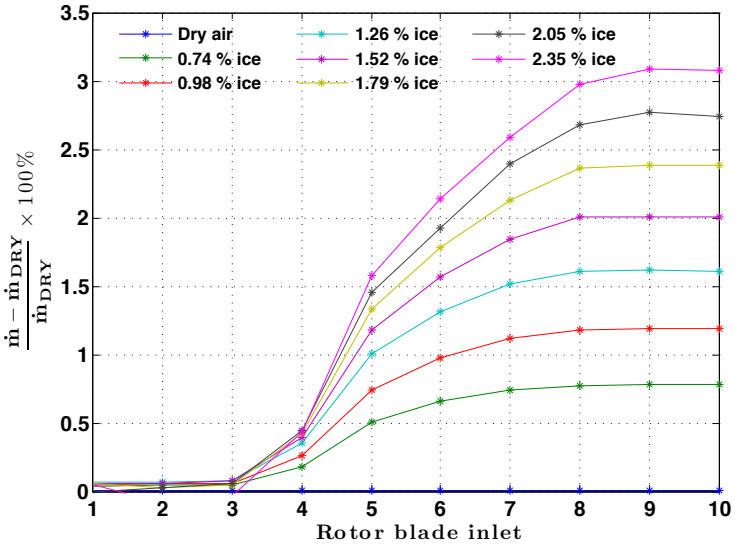

Figure 45: Percentage difference in mass flow rate at inlet to rotor blade rows with increasing ice flow rates preceding stall

Figure 45 illustrates the percentage difference between the mass flow rate of the air-vapor mixture and the dry air mass flow rate at the inlet of rotor blade rows. The values are normalized by dry airflow rate at the inlet of the individual rotor stages before the ice flow was initiated. The flow rates are registered at time instants of the compressor

operation when the air-vapor mixture has reached a steady state with the discrete phase. As the ice flow rate increases, mass of the continuous phase exhibits a rise that corresponds to incorporation of vapor, especially at the rear stages (Fig. 43). The compressor stalls beyond an incoming steady ice flow rate of 2.5% of dry air flow rate.

The rematching of the compressor to higher pressures at back stages and lower at the front stages causes an increase in the mass of dry air through the compressor. Also it must be noted that bleed ports downstream of the 4th and 7th stages respectively, remove a percentage of the air-vapor mixture as a function of the local static pressure and temperature $\dot{m}_b = k_b \left(\frac{p_g}{\sqrt{T_g}} \right)$. The discrete particle bleed is neglected. At nominal speeds, a higher drop in pressure accompanies a lower drop in temperature at the first bleed port where the rate of bleed air is larger. For example, a 2.35% of ice flow rate results in a 12.5% drop in temperature and 24% drop in pressure at the inlet to the rotor 4 (Figs. 46 and 49). Therefore, air bled out is reduced with increasing ice flow, as compared to dry air operation.

5.2.2.2 Static temperature response in presence of ice

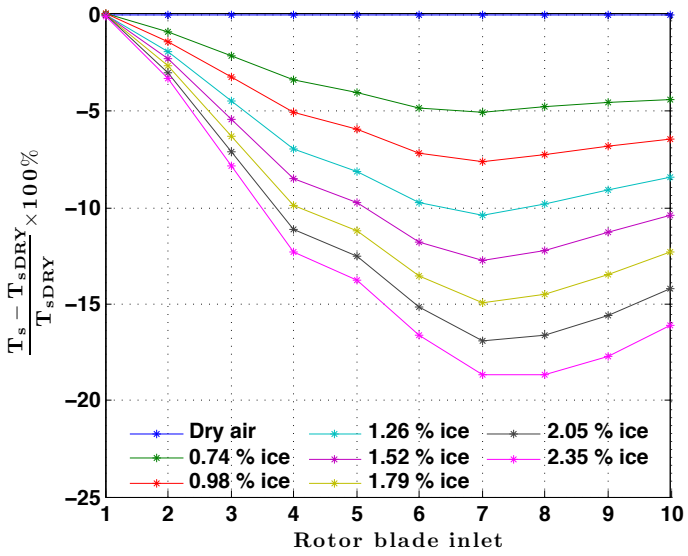

Figure 46: Percentage difference in static temperature at inlet to rotor blade rows with increasing ice flow rates preceding stall.

Figure 46 shows the percentage variation in static temperature through the compressor. A comparison of the temperature of the air-vapor mixture at the rotor blade inlets signifies

a reduction in the heating capacity of the air with increasing ice flow. As seen previously from Fig. 34, temperature drops at each consecutive stage in response to constant rate of ice ingestion. Front stages have greater concentration of ice that cause a small drop in temperature mainly due the drag force on particles and melting of ice. The evaporation of water at the rear stages results in a higher temperature drop due to large latent heat of vaporization absorbed from the air-vapor mixture. For nominal speed operation, complete evaporation occurs at rotors 7 or 8 as shown by the specific humidity plot (Fig. 43). Thus, the maximum drop in temperature occurs at these two stages.

5.2.2.3 Density and velocity response in presence of ice

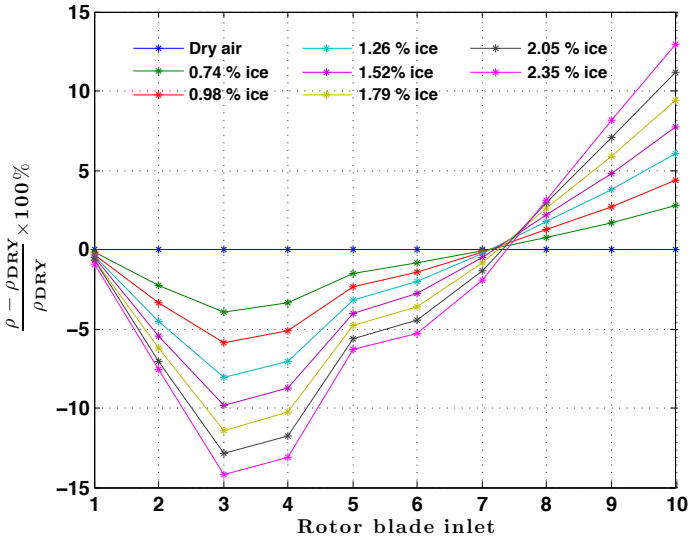

Figure 47: Density distribution at the rotor blade row inlets with increasing ice flow rates preceding stall

The density and velocity variation of the air-vapor mixture as compared to dry air values across individual stages are plotted in Figs. 47 and 48, respectively. The temperature drop in the rear stages creates an increase in fluid density and a reduction in axial velocity. The rear stages in Figs. 47 and 48, display this trend. The reduction in velocity and thus the flow coefficient, results in a shift of the rear stages on their characteristics to higher pressure coefficients and the stage loads (stage 10 characteristic, Fig. 52(c)). A simultaneous unloading of the pressure coefficients occurs at the front stages as the stages rematch in the

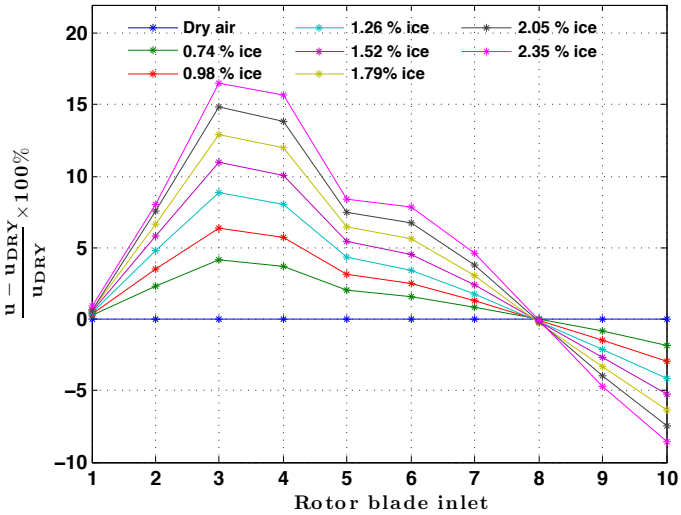

Figure 48: Velocity distribution at the rotor blade row inlets with increasing ice flow rates preceding stall

presence of ice (Fig. 49). The lower pressures at the mid- and front compressor zones result in an increase in dry air pumping. As the compressor pulls the flow, the middle stages are moved to higher flow coefficients (higher velocities, Fig. 48).

The rematching of the stages through the compressor eventually leads to unloading of the front stages to a lower operating point (stage 1 characteristic, Fig. 52(a)). Consequently, the pressure and density rise, fall below the dry air values (density plot, Fig. 47). The flow coefficient increases unloading at the front stages. Thereby, the corresponding axial velocity increases over the front stages (velocity plot, Fig. 48).

It must be noted that the fluid parameters like gas constant and the specific heat at constant pressure of the mixture change as the moisture content increases. These too play a role in the compressor performance [45].

5.2.2.4 Pressure response in presence of ice

Figure 49 shows an overall reduction in pressure as compared to dry air. The ideal gas equation governs this reduction corresponding to the drop in temperatures. Stage rematching that causes the front stage to unload and the back stages to load explains the concave

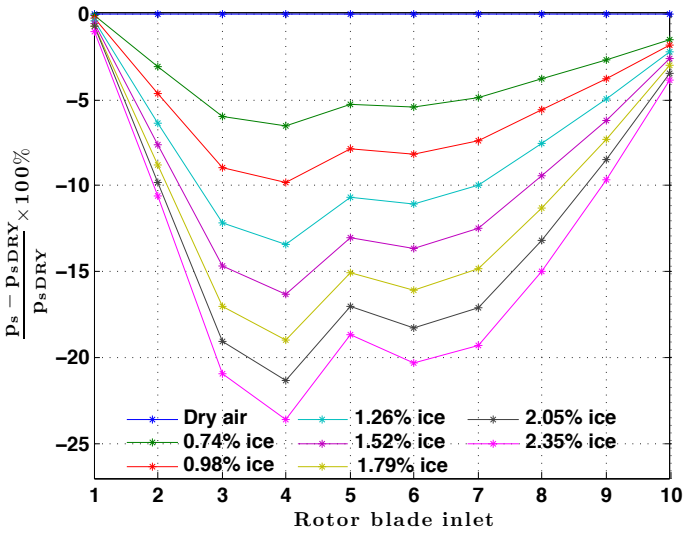

Figure 49: Percentage difference in static pressure at inlet to rotor blade rows with increasing ice flow rates preceding stall.

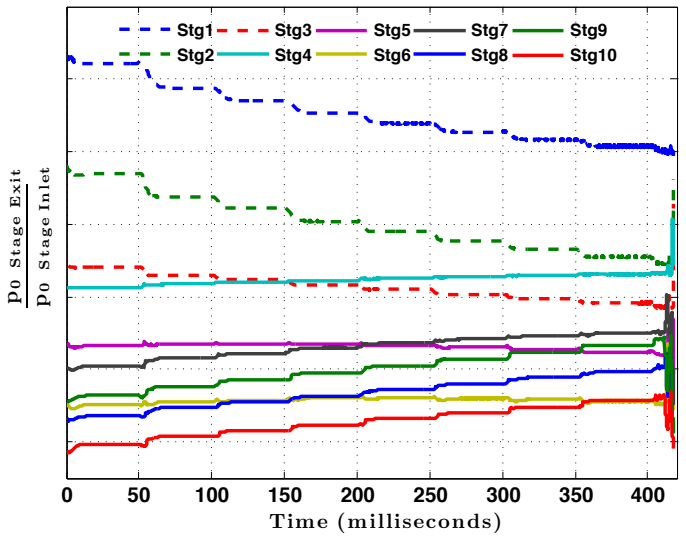

Figure 50: Stage-wise behavior of total pressure ratio across stages with increasing ice flow rates resulting in stall instability

shape of the pressure reduction as noted earlier. In the middle stages, the reduction in temperature is dominant causing the pressure to drop further based on a polytropic relation between the pressure and temperature. An approximate 24% maximum drop in pressure is recorded for a 2.35% of ice around stage 4 before the pressure starts rising again. This is due to the density rise due to cooling of the air. At the front stages with minimal temperature and density variations, the pressures are closer to dry air values. The rematching of

the stages is evident in Fig. 50, demonstrating the variation of stage pressure ratios with gradual increments of ice.

5.2.3 Response of the air-vapor mixture at onset of stall

5.2.3.1 Mass flow rate response

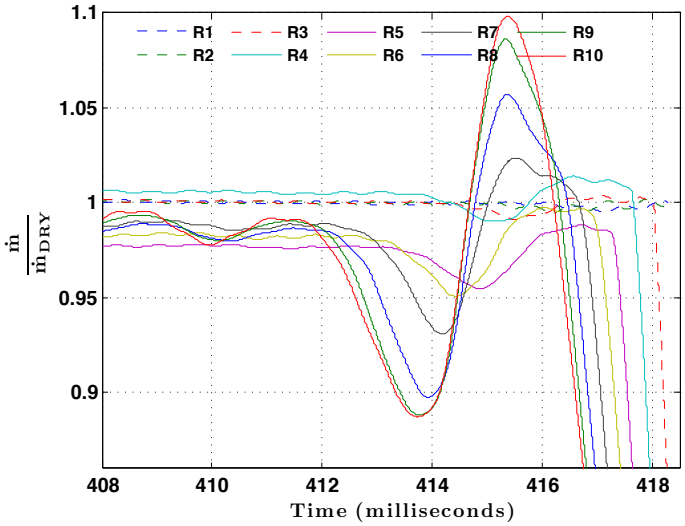

Figure 51: Snapshot of humid air flow rate at inlet to rotor blade rows during stall instability

Figure 51 captures a snapshot of the compressor operation just before stall when the flow starts exhibiting oscillatory behavior in response to ice. The mass flow rate variation from start of compressor operation is already shown in Fig. 44. The onset of stall is characterized by oscillations about the stall point followed by an irrecoverable rapid unloading of the front stages and a loading of the back stages. The plot clearly reveals that the stage 10 collapses first, ensued by a rapid propagation of the instability through the upstream stages one after another until the entire compressor fails. The dynamic stage characteristics are explored below.

5.2.3.2 Stage characteristic

Figure 52 depicts the axial force coefficient plotted versus the flow coefficient for stages 1, 5 and 10. It exhibits a shift in the operating point with growing ice flow rates. The dry compressor operation starts at the first design point on the force characteristic map (red square marker). As the ice crystals are ingested in the compressor, the operating point

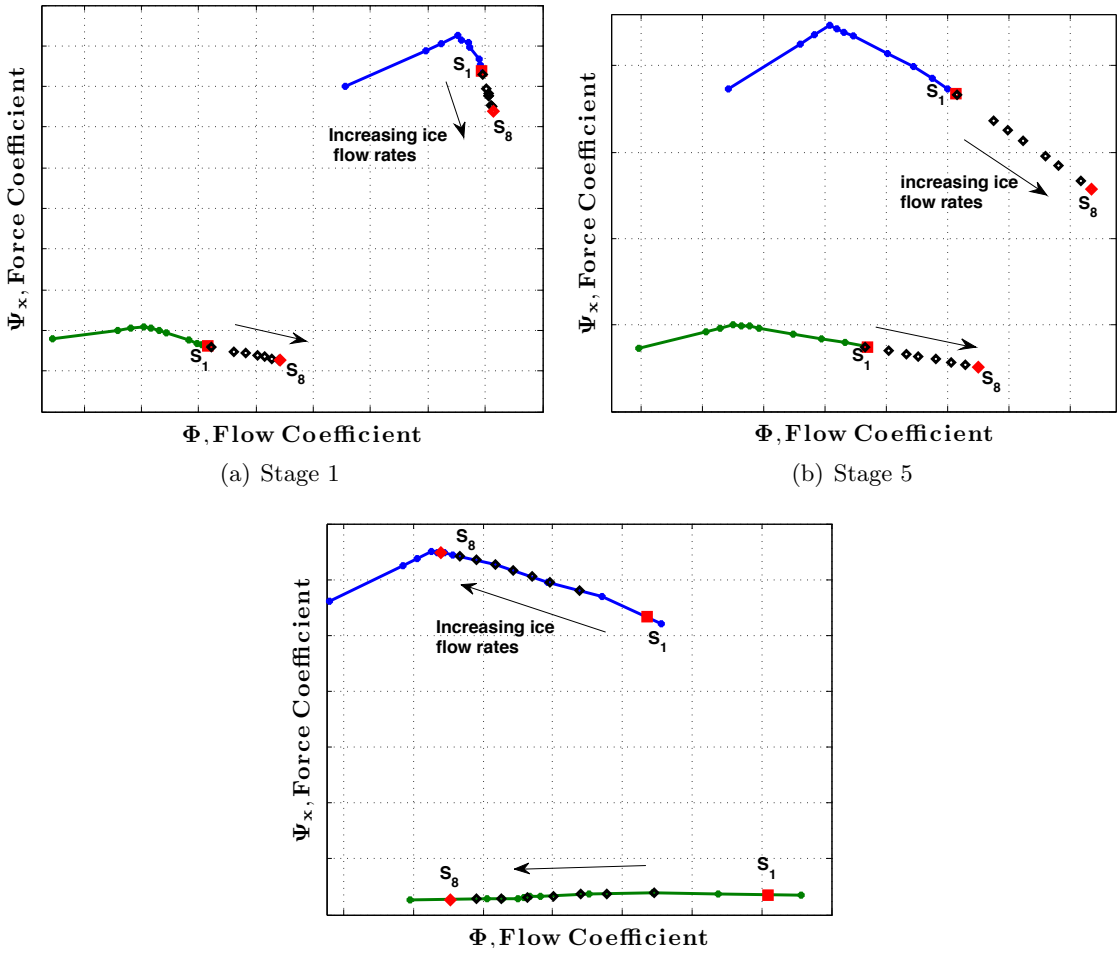

(a) Stage 1

(b) Stage 5

(c) Stage 10

Figure 52: Stage-wise behavior of axial force coefficient. Blue and green curves are the rotor and stator characteristic maps, respectively. Each of the markers are the steady states attained for every ice flow rate, denoted from S_1 to S_8.The red squares mark the initial state, whereas the diamonds mark the final state of the stages. The black diamonds are intermediate states.

shifts. A distinct directional deviation in the operating point is observed where the rear stages load, accompanied by unloading of the front stages. The trend confirms that the early stages operate near choke and the rear stages near stall. The corresponding stage pressure ratio in Fig. 50 captures the same trends.

5.2.3.3 Compressor pressure ratio in presence of ice

The maximum acceptable gas turbine power output and the surge limit in the compressor stages limit the total amount of ice that can be ingested. Figure 53 depicts the increase

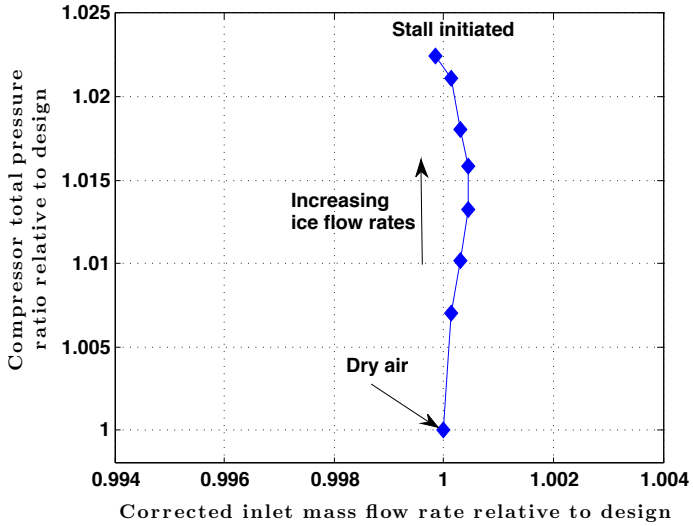

Figure 53: Pressure rise across compressor with increasing ice flow rates

in the compressor pressure ratio with ice flow versus the inlet corrected mass flow rate. The flow rate is restricted by the steep characteristic of the pressure rise with flow rate of the first stage as seen in Fig. 52(a). Thus the pressure rise is almost vertical. However, the continued increase in shed ice flow rates eventually leads to a compressor instability, primarily due to the transition of the operating point on the last stage compressor map towards the stall point.

5.3 Performance and stall analysis of compressor operating at ground idling speed and loading conditions

Simulation Procedure: In this section, a stall onset in the compressor for the same ten-stage compressor geometry as used in previous simulations, but operating at ground idling conditions (65% inlet corrected speed) is investigated. The compressor characteristic maps that govern the pressure and total temperature rise now corresponds to ground idling speed. The ice ingestion process is the same as described for nominal speed conditions (Sec. 5.2).

Brief Analysis: Figure 54 records the variation of humid air mass flow rate through the compressor. Figure 55 shows the increase in vapor produced as ice gets ingested. The percentage difference of humid air flow variables with the respective dry air values at steady state time instants is investigated for the following parameters: (i) mass flow rate (Fig. 56) (ii) temperature (Fig. 57) (iii) density (Fig. 58) (iv) velocity (Fig. 59) and, (v) pressure (Fig. 60). The individual stage response to ice is evaluated from these results. The individual stage response and the stalling stage is observed from the shift in the operating point on the individual stage characteristics (Fig. 61). The loading of the stages is investigated from the transient pressure response by Fig. 62. Figure 63 shows the increase in compressor overall pressure ratio with increasing ice flow rates. The stage where stall initiates is detected from the force coefficient transients preceding instability (Fig. 64). A further detailed analysis is presented in the next sections.

5.3.1 Humid air response to increasing ice flow preceding stall

Figure 54 depicts the mass flow rate of the gas through the compressor. Initially, the dry air operation is started and allowed to stabilize. A steady flow rate of ice is introduced after 60 milliseconds of dry air operation and is increased every 60 milliseconds. The first approximate time when the flow conditions achieve steady dry air operating conditions is denoted by S_1. S_2, S_3 and S_4 denotes a steady flow condition of the humid air for ice flow rates of 0.47%, 0.94% and 1.4% of dry air, respectively. The next step increase to 1.9% of dry air causes small steady oscillations in the flow. A slight further increase of ice rate to 1.95% after 300 milliseconds, triggers oscillatory pressure transients that causes the

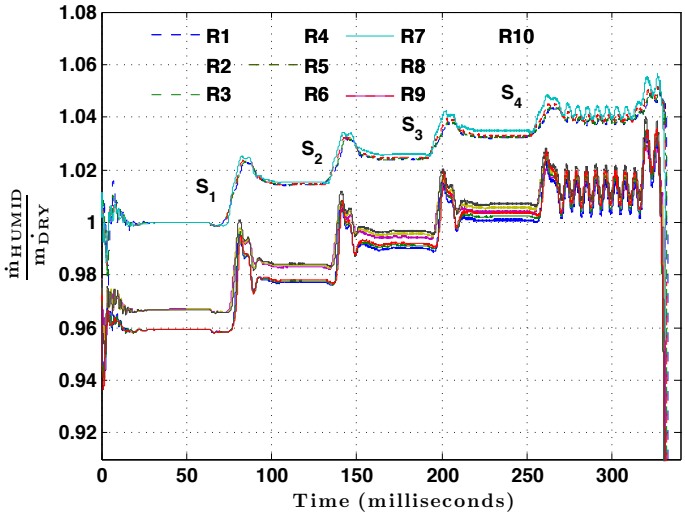

Figure 54: Transient mass flow rate variation at rotor inlet locations with increasing ice flow rates, preceding stall.

compressor to collapse into a stall instability.

5.3.1.1 Specific humidity

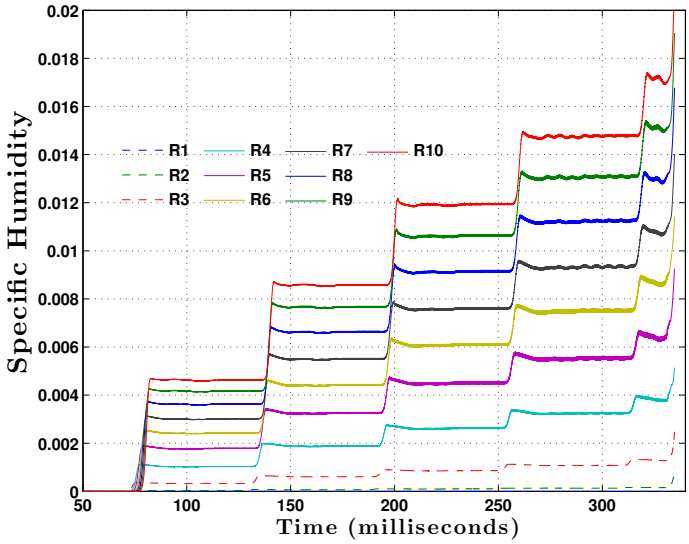

Figure 55: Transient variation of specific humidity with increasing ice flow rates at rotor inlet locations

Figure 55 shows the variation of specific humidity recorded at the rotor inlet locations. The clear delineation of the recorded mass of vapor at the rear stages in Fig. 55 suggests incomplete evaporation within the compressor. There is the possibility of residual water

and ice at the exit of the compressor that progress towards the combustor. This may have an impact on the combustor performance. Figure 43 illustrating the moisture content at high-speed operation indicates that evaporation is mostly completed by stage 8 and no more vapor is generated in the last two stages. This implies that discrete phase particles in the form of ice or water do not flow out through the compressor exit as opposed to idling speed conditions. The maximum specific humidity is 0.017 for a maximum ice flow rate of 1.9% at idling speed, while specific humidity rises to 0.0275 for an ice flow rate of 2.35% at nominal speed before stall.

The residence time of the discrete particles through the stages is higher at idling speed. At higher operating speeds, the mass flow rate or vapor response to advancing ice is signaled by a steep rising slope in quick succession at every stage, indicating faster traveling discrete particles (Fig. 43). While, a slower increase in mass of vapor at distinct times at successive stages for idling speeds emphasizes higher residence time through the stages (Fig. 55). Hence, the discrete particles start evaporating earlier as compared to nominal speed operating conditions. This can be observed with the noticeable rise in vapor flow at rotor 3 in Fig.55, while the specific humidity plot at nominal speed (Fig. 43) shows traces of vapor only after rotor 4.

5.3.1.2 Mass flow rate variation in presence of ice

The percentage change in mass flow rate of humid air is recorded in Fig. 56. Although, the pressure rise at the choked throttle decreases the mass flow rate, the pronounced drop in temperature causes the mass flow rate to display an overall increase. The lower pressure through the front and mid-compressor section results in an increase in dry air pumping capacity through the inlet with increasing ice rates. Most of the ice ingested by the compressor is converted to vapor. The total mass flow rates at the inlet of rotor 10 approximately equals to the dry air at the inlet of rotor 1 and the mass of ice flow rate through the compressor.

It is noted that the compressor can tolerate a smaller amount of ice (ice to air ratio of 1.9%, Fig. 56) at lower speeds for stable operation as compared to nominal speed conditions (ice to air ratio of 2.35%, Fig. 45), before the inception of stall instability. Lower

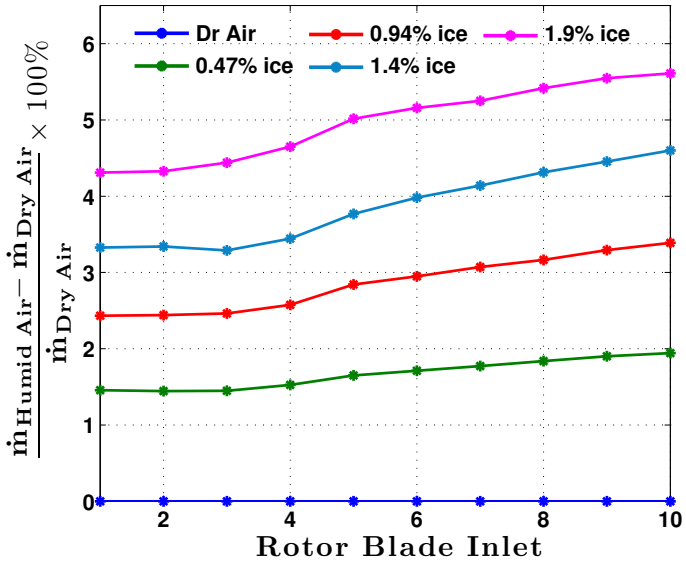

Figure 56: Percentage change in humid air mass flow rate at rotor inlet locations

flow velocities and lower temperatures at the idling speed operating conditions explain the contrast with the performance at nominal speed operation.

5.3.1.3 Static temperature, density and velocity variation in presence of ice

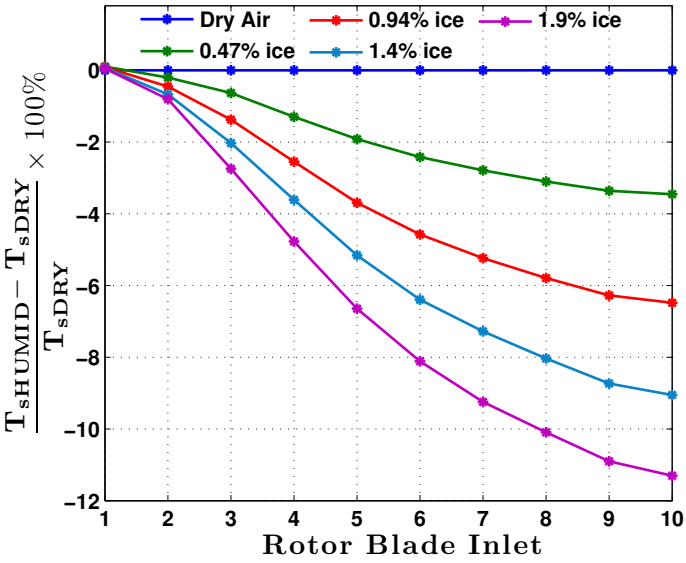

Figure 57: Percentage change in humid air static temperatures at rotor inlet locations

Figure 57 shows that the static temperature of humid air monotonically decreases in the presence of ice through the compressor. This matches with continuous enthalpy loss

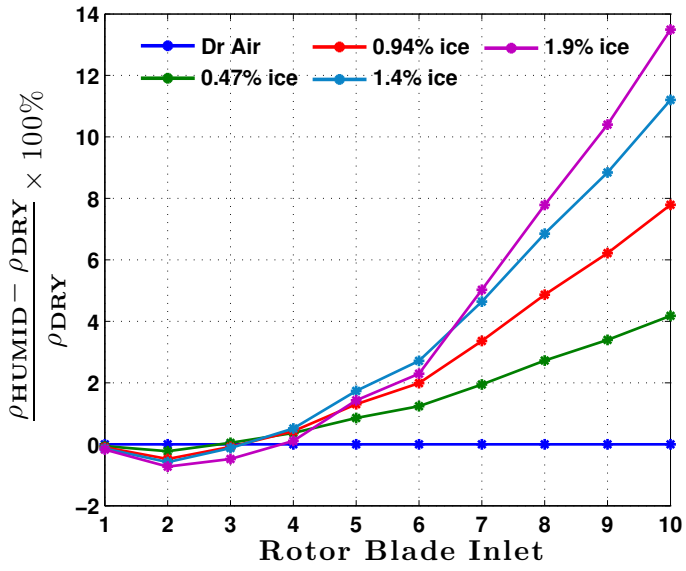

Figure 58: Percentage change in humid air density at rotor inlet locations

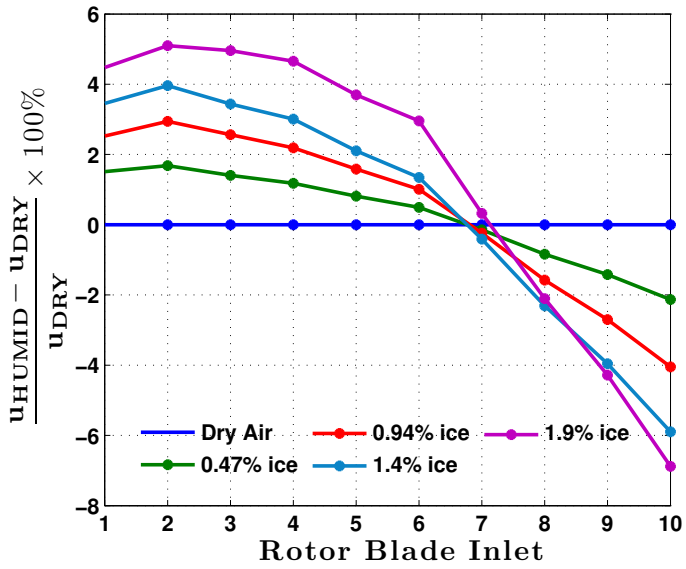

Figure 59: Percentage change in humid air axial velocity at rotor inlet locations

up to the compressor exit due to evaporation as seen from the monotonic specific humidity rise. The drop in temperature is exacerbated by an increase in incoming ice (11.4% prior to stall). On the other hand, for the high-speed case, complete evaporation occurs by the time ice particles get to rotor 8. Thus, the drop in temperature peaks at stages 7 and 8 (temperature plot, Fig. 46).

The peak in temperature reduction at rotor 10 inlet is responsible for the corresponding rise in density at rotor 10, as demonstrated in Fig. 58. Figure 59 exhibits a drop in the velocity at rotor 10 corresponding to the density rise. The change in velocity across the compressor can be explained by analyzing the stage rematching.

5.3.1.4 Static pressure variation in presence of ice

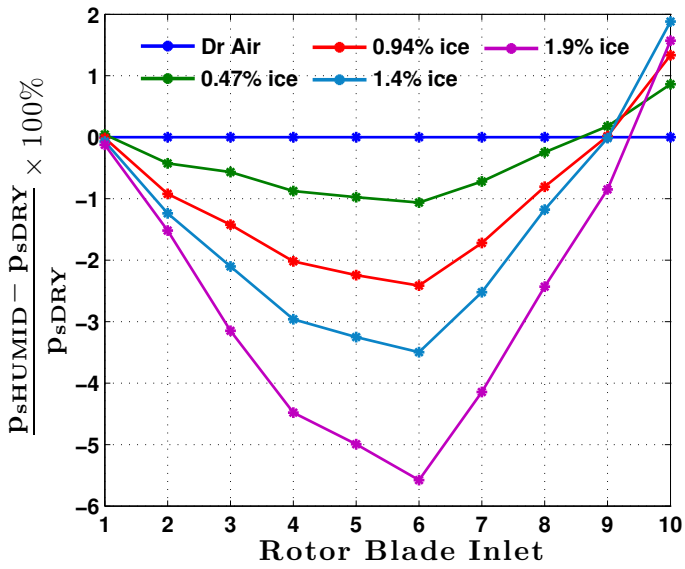

Figure 60: Percentage change in humid air static pressures at rotor inlet locations

Figure 60 shows an overall reduction in pressure as compared to dry air. The ideal gas equation governs this reduction corresponding to the temperature reduction. Stage rematching that causes the front stages to unload and the back stages to load explains the concave shape of the pressure reduction.

5.3.2 Response of the air-vapor mixture during onset of stall

5.3.2.1 Stage rematching in presence of ice

Figure 61 presents the pressure coefficients for the first, middle and last stages of the compressor. Figure 61(c) reveals a loading of pressure characteristic with increasing ice flow rates. The increase in density and corresponding drop in velocity occurs due to the cooling effect. This is highlighted by the decrease in flow coefficient on rotor 10 characteristic

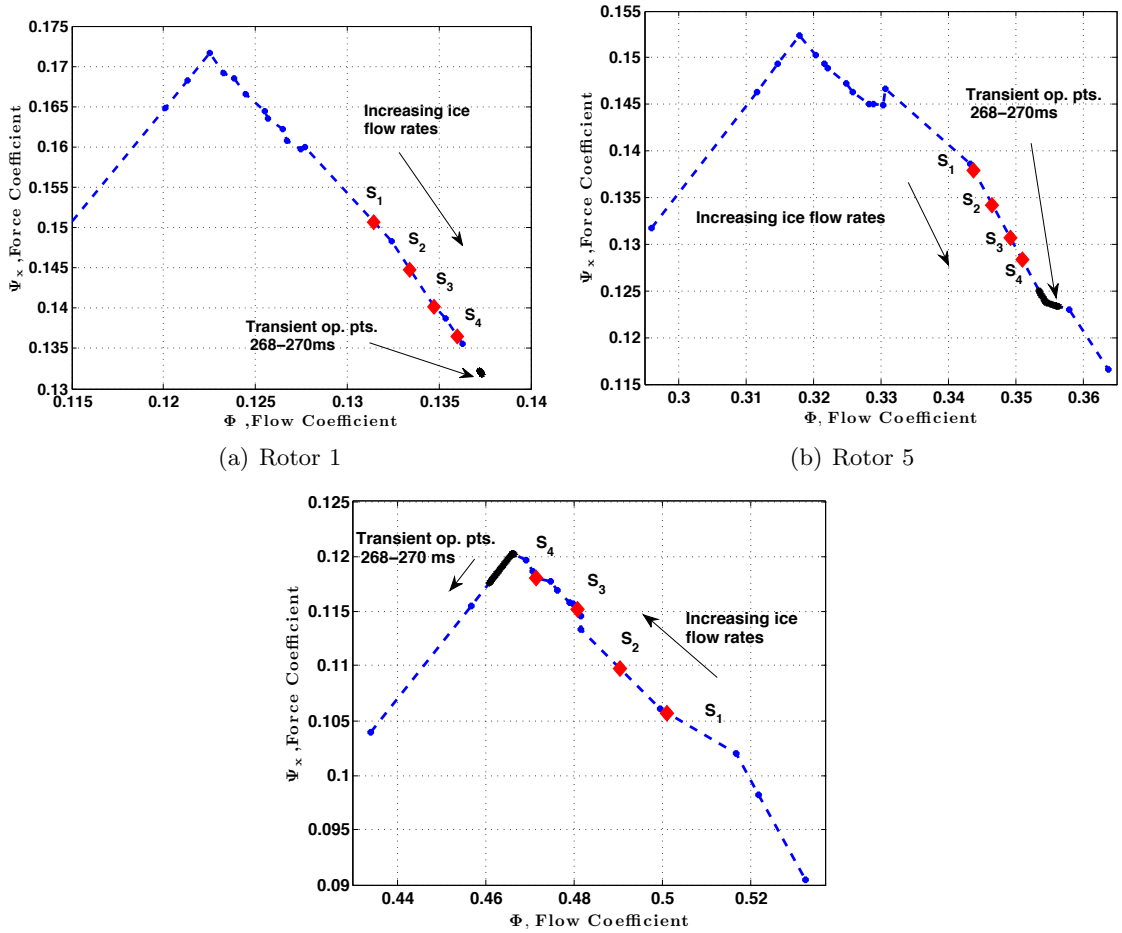

(a) Rotor 1

(b) Rotor 5

(c) Rotor 10

Figure 61: Stage-wise behavior of axial force coefficient. The diamonds mark the steady state of the stage for every ice flow rate. The black markers are the transient points for the time period of 268 to 270 milliseconds during stall instability.

map (Fig. 61(c)). In turn, the pressure coefficient and thus the pressure increases at the rear stages, depicted by the pressure plot (Fig. 60).

The rise in pressure at the choked throttle reduces the mass flow rate, however the drop in temperature increases the overall mass flow rate through the exit. The rematching of the stages to a lower pressures in the front and mid-stages of the compressor causes an increase in the pumping capacity of the compressor. The rise in dry air mass flow rate at the inlet, as seen in Fig. 56, is as a consequence. There is negligible variation in temperature and density at the front stages of the compressor. Therefore, the velocity increases (Fig. 59), with the increasing mass flow through the front stages. The flow ratios follow the upward

trend in velocity, thus unloading the front stages as noted in the rotor 1 characteristic in Fig. 61(a).

The characteristics also aid in illustrating that the last stage, approaches stall point first and initiates instability. Stall is initiated at the 10th stage for both nominal and idling speed operations with increasing ice ingestion.

5.3.2.2 Compressor pressure ratio variation in presence of ice

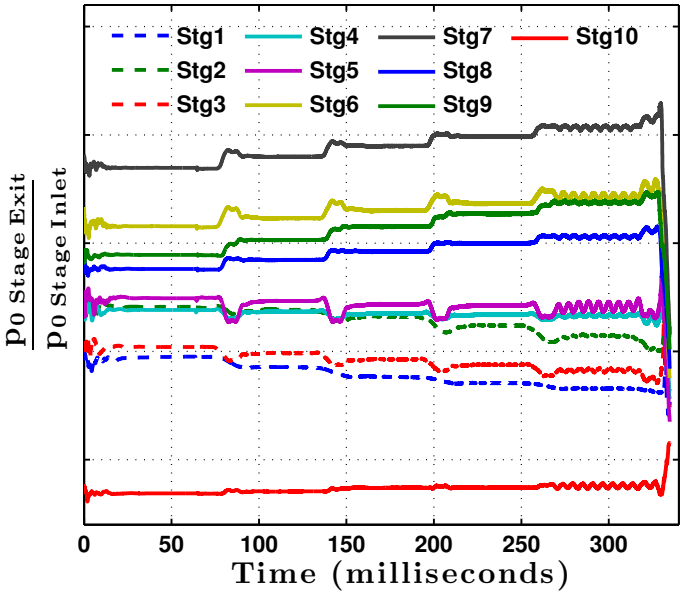

Figure 62: Transient variation of total pressure ratio across stages for increasing ice flow rates.

The loading of the pressure at the rear stages can be also ascertained from the stage pressure ratio trend in Fig. 62. Pressure ratios from stages 6 to 10 are seen to be increasing, while stages 1 to 5 unload with an increase in ice ingestion rates.

The stage rematching causes the overall compressor pressure ratio to increase as indicated in Fig. 63. The stage characteristic of rotor 1 at idling speed operating conditions, has a small slope (Fig. 61(a)) as compared to the steep slope of rotor 1 characteristic at the nominal operating speed (Fig. 52(a)). This is manifested in a large increase in flow ratio as the stage unloads. Consequently, the compressor pressure ratio increase with the corrected inlet flow rate has a lower slope as shown in Fig.63, as compared to the almost vertical rise

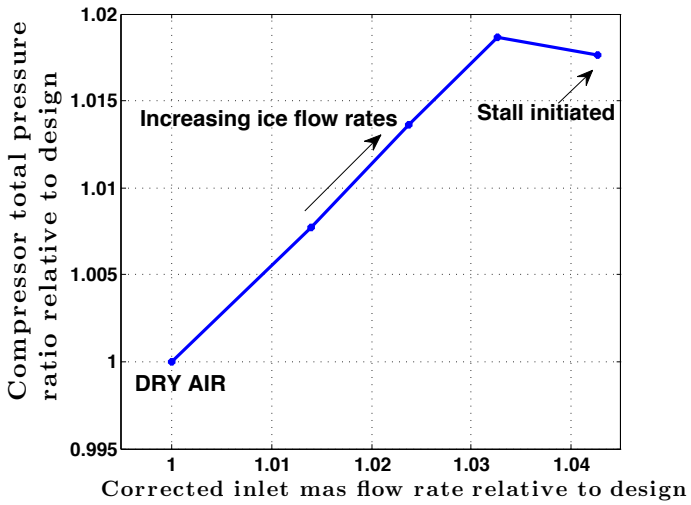

Figure 63: Overall compressor pressure ratio

in pressure ratio versus inlet flow rate at higher speed (Fig.53).

5.3.2.3 Force coefficient variation in presence of ice

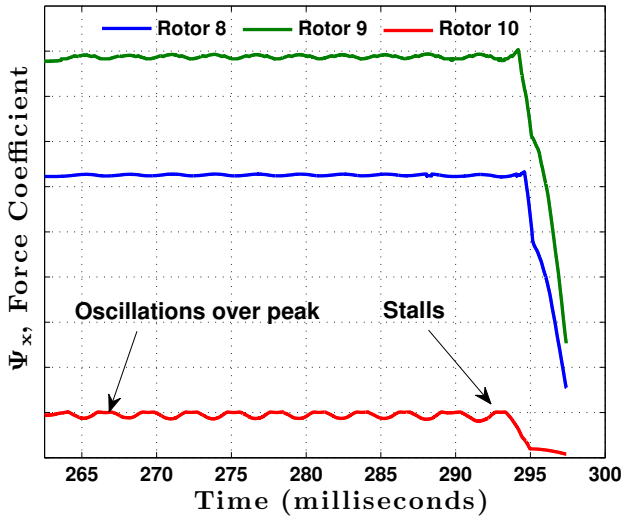

Figure 64: Force coefficient of the rear stages displaying stall of compressor and the stalling stage.

Figure 64 depicting a snapshot of the variation of axial force coefficient for rotors 8, 9 and 10 demonstrates the instability of the compressor operation when the ice rate is increased by a step from 1.9% to 1.95% of dry air rate. The compressor falls into an unstable regime

after 260 milliseconds as the rear stages move beyond the stall point with increasing ice ingestion. Between 268 to 270 milliseconds with ice flow rates at 1.9%, the force coefficient and the total pressure, begin to oscillate. The oscillations on the characteristic maps are displayed in Fig. 61. A small increase in ice to 1.95% triggers the collapse. Rotor 10 is the first to locally collapse (Figs. 61(c) and 64) followed by the rapid decay of pressures in the upstream stages.

5.4 Summary

A summary of findings of the response of the compressor to ice ingestion is detailed here. The fundamental flow response of the compressor for both idling and nominal speed operations remains the same. The locations of maximum temperature, pressure and density vary at different speeds.

Table 4: Compressor performance recorded for the last stable humid air flow conditions with the final step increase in ice rate beyond which the compressor stalls. (Percentages are with respect to dry air design conditions).

Performance prior to stall	Nominal (98%) speed	Ground idling (65%) speed
Stall instability range % $\dot{m}_{ice}$	2.35 -2.5%	1.9 -1.95%
specific humidity	0.0275	0.017
$\approx$ % rise in $\dot{m}_{exit}$	3.10%	5.60%
$\approx$ % drop in T_g, stage	18.5%, Rotor 7	11.4%, Rotor 10
$\approx$ % drop in p_g, stage	24.0%, Rotor 4	5.8%, Rotor 6
$\approx$ % rise in density, stage	13.0%, Rotor 10	13.8%, Rotor 10
$\approx$ % drop in density, stage	14.5%, Rotor 3	0.8%, Rotor 2
$\approx$ % rise in velocity, stage	17.0%, Rotor 3	5.2%, Rotor 2
$\approx$ % drop in velocity, stage	8.0%, Rotor 10	7.0%, Rotor 10
Stalling blade row	Rotor 10	Rotor 10

The compressor stall is triggered when a step increase in ice flow rate is applied from 2.35% to 2.5% of dry air at nominal speed. The dry air mass flow rate used for comparison is measured at the inlet in absence of any ice flow rate. The ice step from 1.9% to 1.95% triggers stall at idling speed conditions. The percentage change in humid air flow variables recorded in Table 4 is for the final ice flow rate (2.35% nominal speed and 1.9% idling

speed). The following observations are drawn,

1. The percentage rise in humid air recorded at the compressor exit is higher at idling speed (Fig. 56) than at nominal speed (Fig. 45). This is due to the pronounced increase in dry air pumping capacity at idling speed.

2. The rematching of the stages causes an inflection (rise/fall) of the response of humid air flow variables in the mid-compressor section. The stage where this occurs depends on the operating speed conditions.

3. The maximum inflection point of percentage pressure (drop followed by rise) occurs earlier (rotor 4) at nominal conditions as compared to idling speed (rotor 6). The maximum temperature inflection point (drop followed by rise) occurs at rotor 7 indicating completed evaporation of the discrete ice and water droplets at nominal conditions. The monotonic drop in temperature up to the exit at idling speeds indicates continuous evaporation till the exit. Thus, the compressor may have residual discrete particles flowing out at idling speed.

4. The rise in density at the exit of the compressor is temperature induced and is comparable between the two speeds. The drop in density at the mid-compressor section is pressure driven and is more pronounced at nominal speeds.

5. The rise in density at the compressor exit is accompanied by a drop in velocity. Similarly, the drop in density at rotor 3 for nominal conditions and rotor 2 for idling conditions is accompanied by a rise in velocity at the same rotors.

6. The percentage of ice that causes the stall is lower for the idling speed as compared to the nominal speed case. For the ten-stage compressor investigated in this thesis, the last stage stalls in presence of ice. This finding may vary for a different compressor configuration.

5.5 Comparison of ice ingestion effects with water droplet injection

The injection of water droplets into the compressor is commonly used for boosting power output from industrial gas turbines. The gas turbine power increases chiefly due to reduced compressor work per unit flow and increase in mass flow rate from vaporizing water. A vital aspect of performance impact with ingested ice that is analogous to wet compression, is the nature of the off-design behavior of the compressor that results from evaporative cooling.

White and Meacock [104] have investigated the mechanism of stage rematching with water over-spray where significant evaporation takes place within the compressor. Bianchi et al. [8] developed the code IN.FO.G.T.E. (Interstage Fogging Gas turbine Evaluation) to predict the shift of the operating point on an axial compressor performance map due to injected water. The researchers also performed a parametric study to study the effect of different droplet diameters on the compressor performance.

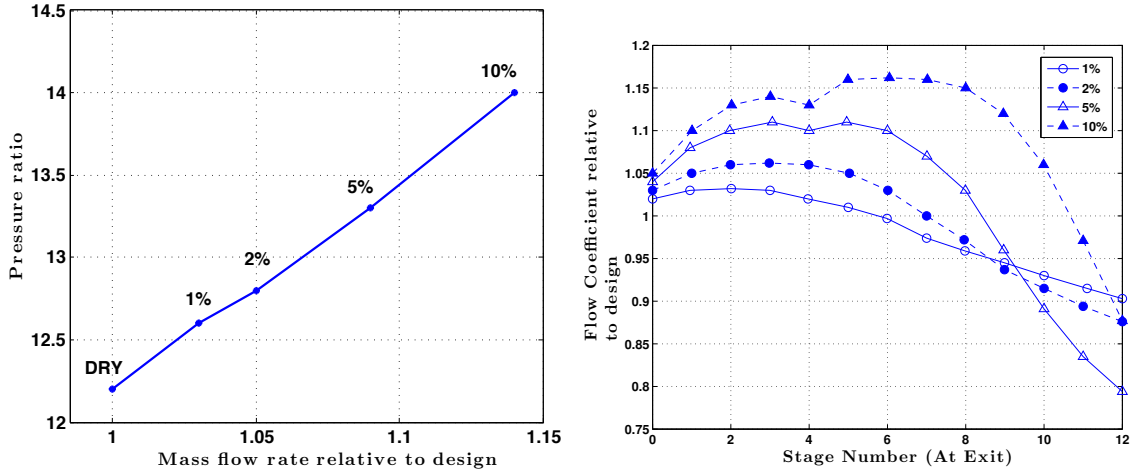

(a) Compressor pressure ratio

(b) Stage flow coefficients

Figure 65: Qualitative comparison with increasing water injection rates, White and Meacock [104]

Results from White and Meacock [104] and Bianchi et al. [8] are used to illustrate the wet compression effects. Table 5 presents the similarities of the performance trend resulting from increasing percentage of water spray to that of the compressor response with increasing ice ingestion rates. The table refers to trends observed from plots for idling speed and nominal speed compressor operations with ice crystal ingestion in the present study. A comparison

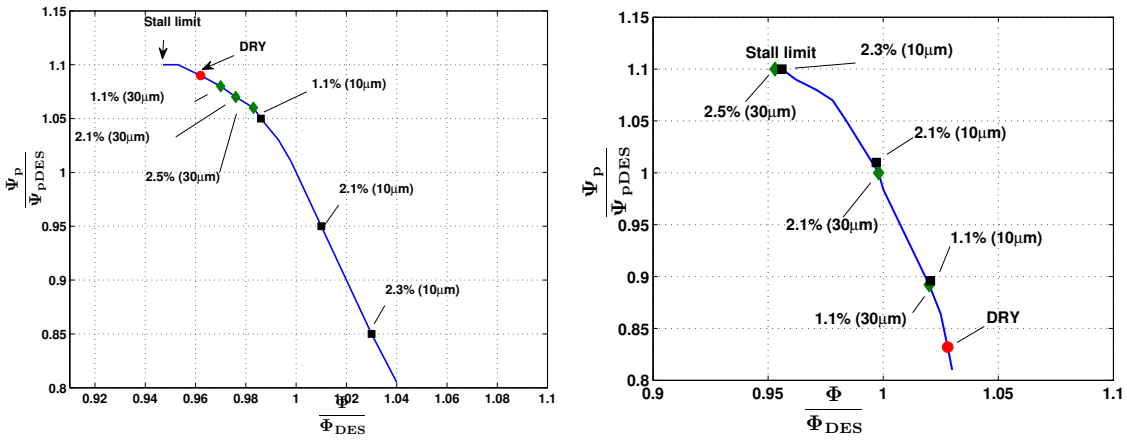

(a) First stage performance map and operating points

(b) Seventeenth stage performance maps and operating points

Figure 66: Qualitative comparison with increasing water injection rates, Bianchi et al. [8]

is made with the plots from the literature as discussed in Table 5.

Table 5: A qualitative comparison of compressor performance between increasing water droplet injection in literature and ice crystal ingestion in the present study.

Performance trend	Literature (water droplets)	Present Study (ice crystals)
Increase in overall compressor pressure ratio	Pressure ratio, Fig. 65(a), White and Meacock [104]	Nominal speed case: Fig. 53 and Idling speed case: Fig. 63
Increase in dry air pumping capacity of the compressor	Mass flow rate, Fig. 65(a), White and Meacock [104]	Idling speed increase in inlet dry air flow rate Fig. 56
Stage rematching where front stages unload while back stages load	Flow coefficients increases at front and decreases at rear stages, Fig. 65(b), White and Meacock [104]	Nominal speed case: 52 and Idling speed case: Fig. 61
Front stages operate near choke	First stage characteristic, Fig. 66(a), Bianchi et al. [8]	Idling speed, Fig. 61(a) and Nominal speed, Fig.52(a)
Back stages move closer to stall	Last stage characteristic, Fig. 66(b), Bianchi et al. [8] AGARD report [30], Ch. 1, Fig. 5	Nominal speed case: Fig.52(c) and Idling speed case: Fig. 61(c)

CHAPTER VI

EVALUATION OF MODEL PARAMETERS AND ASSUMPTIONS

The impact of some of the assumptions and semi-empirical models used in the coupled discrete-continuous phase computer code on the simulation results is investigated (Kundu et al. [48]). There are numerous physical inputs that affect the icing study results. Of particular interest are the size and distribution of ice crystals, percentage bleed of ice particles through compressor bleed ports and the discrete particle breakup semi-empirical models. Understanding and quantifying the influence of these parameters on the predicted results from the numerical model is important for gaining an understanding of icing related engine instabilities. The impact of these factors on the compressor flow dynamics is estimated through a parametric analysis. The numerical results presented in this chapter are for the nominal speed operation of the same ten-stage compressor that was discussed in Chapter 5.

6.1 Impact of ingested ice diameter distribution at compressor inlet on the compressor flow dynamics

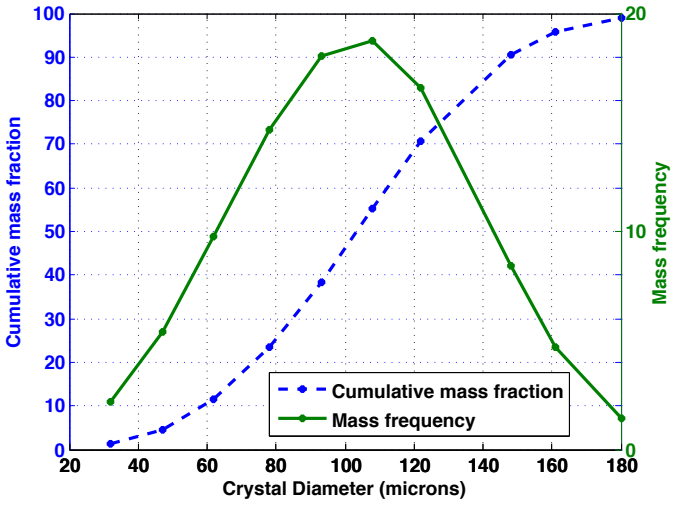

Figure 67: Particle size distribution

Bianchi et al. [8] discussed the droplet size and temperature influence on wet compression. The response of gas turbine performance and distribution of load across the stages to variation in liquid water droplet size was found to be significant. Sun et al. [92], applied a droplet spray distribution to study the effects of water ingestion in a transonic compressor. Knezevici et al. [46] ascertained the importance of ice crystal size in the accretion of ice in the compressor through an experimental investigation. An examination on the impact of ice crystal sizes on the overall compressor performance due to ingested ice is carried out in this section.

A Rosin-Rammler diameter distribution is adopted for the spread of atmospheric ice crystal sizes flowing into the compressor. The Rosin-Rammler distribution can be expressed as,

$$Y = 1 - exp\left(-\left(\frac{D_p}{\overline{D}}\right)^n\right) \tag{73}$$

where Y is the cumulative mass fraction of particles smaller than diameter D_p, $\overline{D}$ is the mean value diameter (MVD) of the distribution and n is the spread parameter. n expresses the steepness of the particle size distribution curve. As value of n increases, the diameter distribution becomes more uniform. Usually the constant n is in the range $1.5 \leq n \leq 4$ for most sprays. The total ice flow rate ($\dot{M}_p$) entering into the compressor free stream is specified as an input variable. A ten-bin distribution around the mean diameter is constructed. Figure 67 illustrates an example of the particle size distribution for $n = 3.4$ and mean diameter $\overline{D} = 115\,\mu m$. Simulations were performed for ice crystal MVD's of 55 µm, 115 µm, 175 µm, 235 µm, 295 µm, 355 µm, 415 µm, 615 µm, 815 µm, and 1015 µm for a steady ice flow rate at 0.7% of the airflow rate. The number of ice crystals (N_p) corresponding to each particle diameter that confirms to a Rosin-Rammler distribution $\tilde{f}_m$ is expressed by Eq. 1, in Ch. 2.

Source terms of the discrete phase for a converged simulation are plotted in Fig. 68 for an ice flow with MVD of 55 µmand 1015 µm, respectively. This plot aids in comprehending the impact of the discrete phase of ice, water and vapor on the compressor flow dynamics. The implication of selection of a break model of ice crystals/ water droplets on the temperature

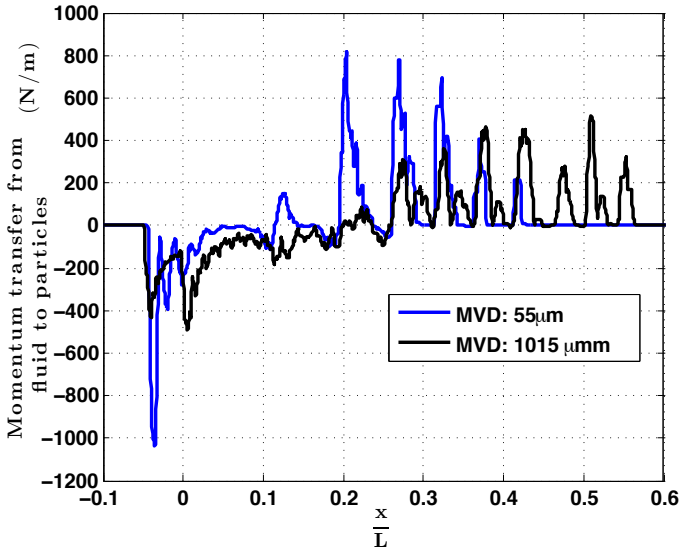

(a) Momentum lost in drag + Momentum of vapor added to fluid

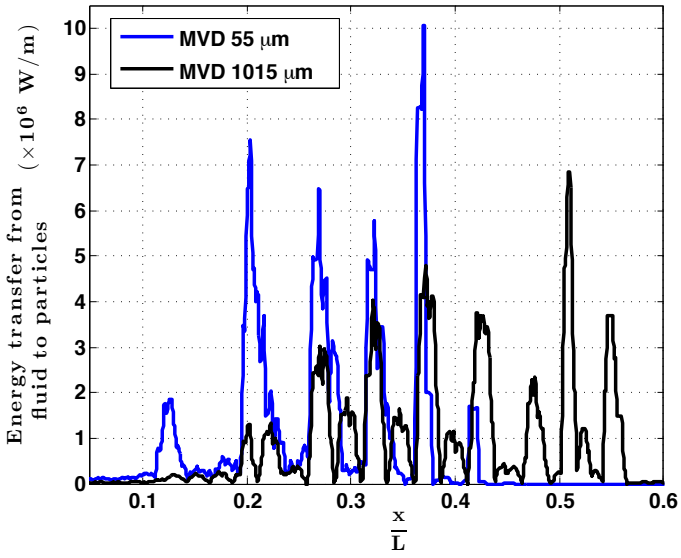

(b) Heat absorbed from fluid + Energy lost in drag + Enthalpy of vapor added to fluid

Figure 68: Source terms from the discrete phase

and pressure dynamics of air is also of relevant interest.

Figure 68(a) depicts the momentum exchange between the air and the discrete phase particles at various stations across the compressor, expressed as the momentum term in source vector $\mathbf{Q}_{\text{discrete}}$ of Eq. 42. The term includes (1) momentum lost by the air as drag on particles, and (2) momentum gained by the gas through incorporation of vapor mass. The drag force predominates at the front end of the compressor. It rapidly decreases as the

crystals break upon encountering the rotor blades. At the rear stages of the compressor, the air acquires momentum of the vapor flowing into it.

Figure 68(b) depicts the energy lost by the air to the discrete phase particles at various stations across the compressor, expressed as the energy term in source vector $\mathbf{Q}_{\text{discrete}}$ of Eq. 42. The term consists of (1) energy lost as drag on the discrete phase, (2) energy absorbed during phase changes as latent heat, and (3) energy added as a gain in enthalpy when vapor is formed. It arises as a negative term in the continuous phase equations. Around the mid-compressor location the smaller particles completely evaporate resulting in a peak of the energy contribution, and thereafter their contribution to the energy source term is absent, as can be observed from the trend of the 55 µm in Fig. 68(b). Larger ice crystals tend to melt and evaporate slower as compared to the smaller ice crystals resulting in incomplete evaporation at the compressor exit. The lower peaks of the 1015 µm crystal ice flow spread across the compressor, relative to the large peaks of the 55 µm ice crystal flow terminating at the the mid-compressor section illustrate this trend.

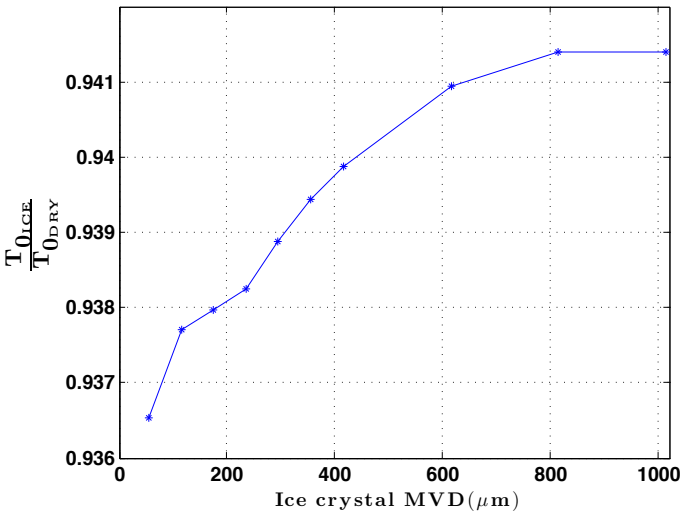

Figure 69: Stagnation temperature variation with crystal size at compressor exit

The disparity in energy contributions seen in Fig. 68 is used in explaining the influence of ingested ice particle sizes on the airflow variables. Figure 69 records the stagnation temperature of the air-vapor mixture at the compressor exit. The stagnation temperatures of air with ice flow is normalized by the dry air temperature at the exit. It can be deduced

that as the size of the ice crystals is progressively reduced, the air is cooled with higher efficiency corresponding to a higher heat sink for smaller crystal sizes (Fig. 68(b)).

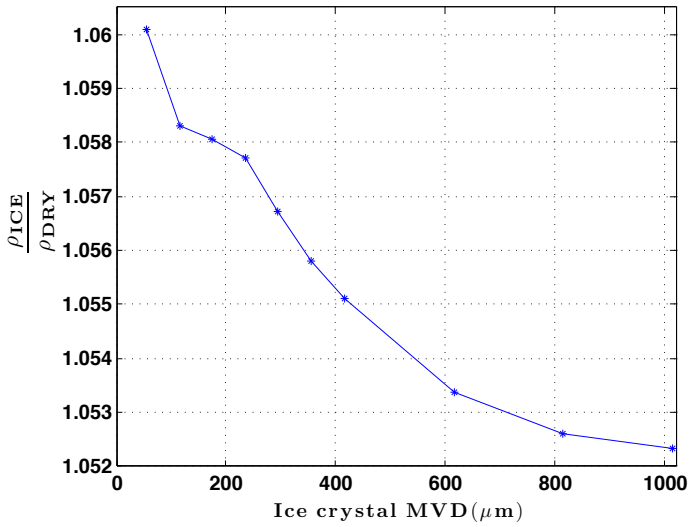

Figure 70: Density variation with crystal size at compressor exit

Chapter 5 presented the change in performance of the compressor stages due to ice ingestion. It has been established that density increases (Chap. 5, Fig. 47, density plot) and the velocity of the humid air decreases (Chap. 5, Fig. 48, velocity plot) as compared to the dry air design values at the exit of the compressor. This causes the compressor rear stage pressures to increase. The larger drop in temperature (Fig. 69) near the back of the compressor for a smaller MVD exacerbates the rise in density of the gas in the presence of ice. This trend is illustrated in Fig. 70 which shows increasing density at the exit of the compressor with a decreasing MVD. As density rises with reduction of MVD, a higher mass flow rate of air is drawn.

Figure 71 illustrates the pressure distribution for varying sizes of ingested ice crystal diameter. Chapter 5, Figure 50 highlights the increase in the pressure at the rear stages and the front stage pressures drop due to ice ingestion as compared to the dry air design conditions. A further increase of density with a reduction in MVD at the compressor exit is accompanied by a higher increase in pressure for the smaller ice particles as compared to the larger ones. The exit pressure in Fig. 71(a) increases with a reducing MVD. The rematching of stages toward the front end of the compressor is seen as a dropping trend in

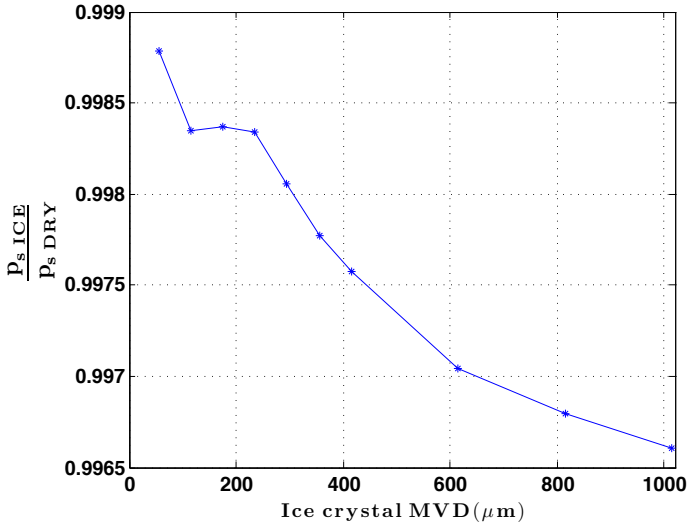

(a) Pressure variation with crystal size at compressor exit

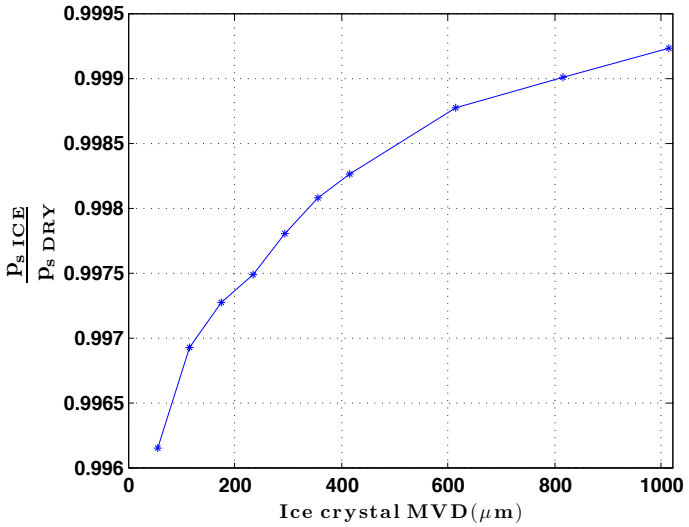

(b) Pressure variation with crystal size at compressor inlet

Figure 71: Pressure distribution.

pressures with decreasing particle sizes at the compressor inlet (Fig. 71(b)).

6.2 Impact of blockage effect on compressor flow dynamics

A concern related to large size ice crystals is their role in blocking the effective area for the airflow. The numerical model for flow of gas in the compressor, (Chap. 2, section 2.2), accounts for this blockage, where the mass flow rate of the continuous phase through a cloud of discrete phase elements is expressed as, $\dot{m} = \rho_c \alpha_c u A$. This section compares the effect of blockage with increasing sizes of incoming ice crystals.

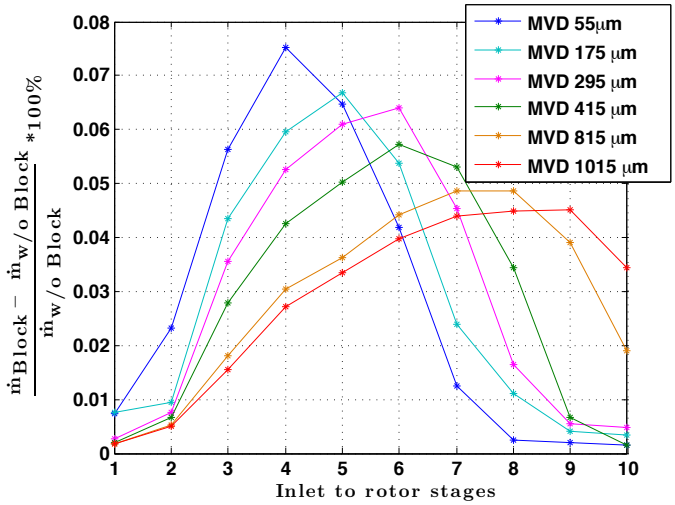

(a) Percentage variation of mass flow rate with and w/o blockage

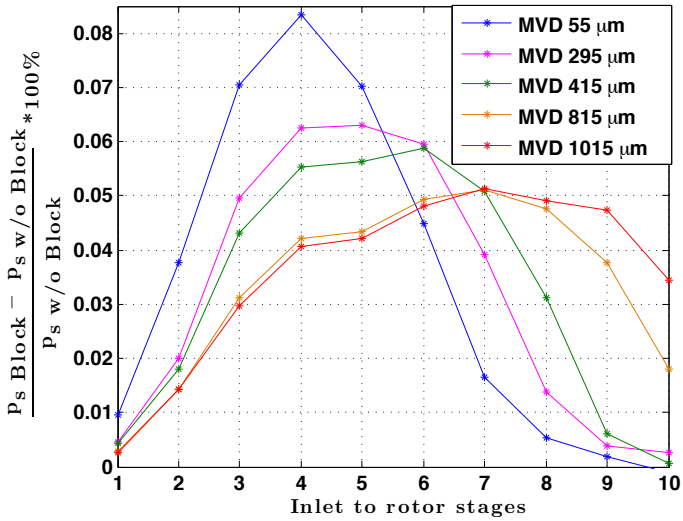

(b) Percentage variation of pressure with and w/o blockage

Figure 72: Mass flow rate and pressure distribution across rotor inlet of 10 stage compressor.

Figure 72(a) plots the mass flow rate of the numerical model with blockage as compared to a baseline model without the blockage. The mass flow rate is recorded at the inlets of each of the rotor stages. The percentage change in the mass flow rate initially increases indicating that as the ice crystals break and the water film is splashed, the blockage increases. The ice particles eventually evaporate and the influence of blockage reduces towards the end of the compressor. Since the breakup and splash of smaller ice crystals is higher and their subsequent evaporation is faster, the smaller ice MVD's display a peak earlier than the larger MVD's. The peak blockage is flatter and more spread out for the larger MVD's

owing to their gradual breakup and evaporation through the compressor.

The pressure plot shown in Fig. 72(b) follows the mass flow rate variation. It is observed from the plots that the application of blockage has less than 1% impact on the flow dynamics. Therefore, it is apparent that the size of the ice particles rather than the ensuing blockage has greater importance in modeling the impact of ice ingested by the compressor on its performance.

6.3 Impact of bleeding of ice on compressor flow dynamics

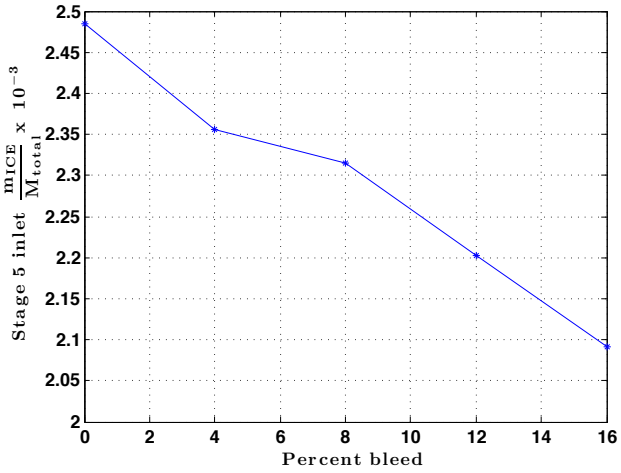

(a) Variation of mass of following a bleed port, at inlet of stage 5

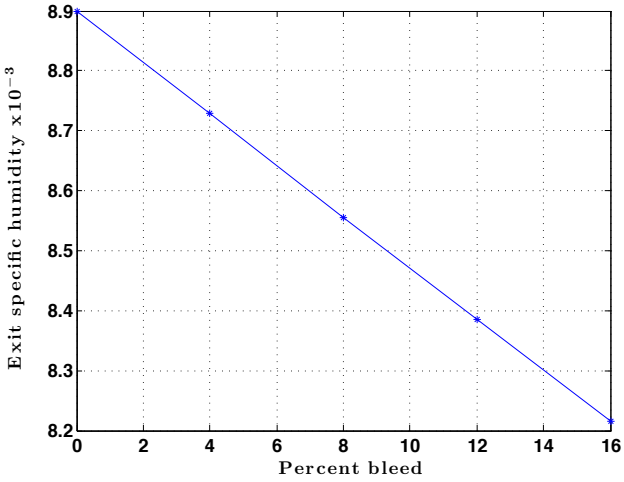

(b) Variation of vapor at the exit of the compressor

Figure 73: Ice and vapor distribution with bleed ice

The compressor has two bleed ports; one aft of the 4th stage, and the next aft of the 7th stage. Chapter 5 results neglect the bleed of discrete particles. This section investigates the response of the flow to bleed of discrete phase particles. Approximately 4% of the air is bled out at the first bleed port. The ice is also assumed to bleed out at the same percentage of the flow rate of ice crossing the bleed locations. The ice bleed percentage is then gradually increased from 4% to $16f$% at the bleed ports. Figure 73(a) quantifies the mass of ice at the entry to the rotor 5 after the first bleed port. The mass of ice shows a clear drop as

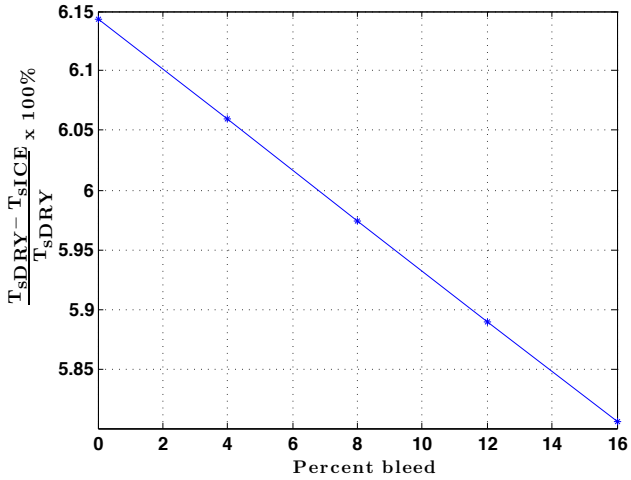

(a) Static temperature at exit of stage 10

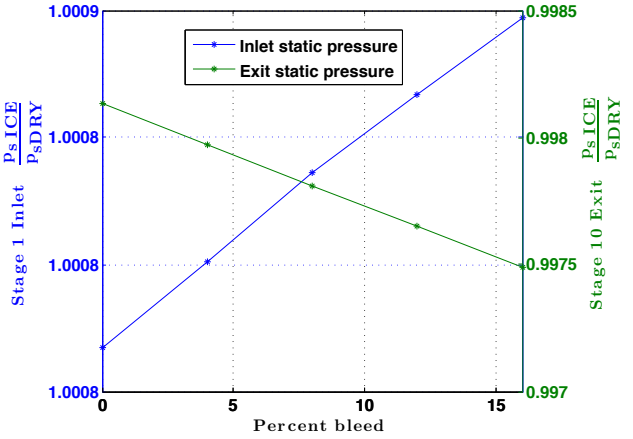

(b) Pressure distribution

Figure 74: Temperature and pressure variation with bleed of discrete phase

bleed is turned on and increased. Plainly, the amount of vapor corresponding to the ice flow also decreases as seen in Fig. 73(b).

The reduction of ice after the 4th stage manifests into a reduced temperature drop from the dry air temperature. This is evident in Fig. 74(a) that shows the exit temperature of the compressor. The pressure rises at the back of the compressor with increasing bleed rates illustrated in Fig. 74(b) along with the drop in pressure at the front end of the compressor.

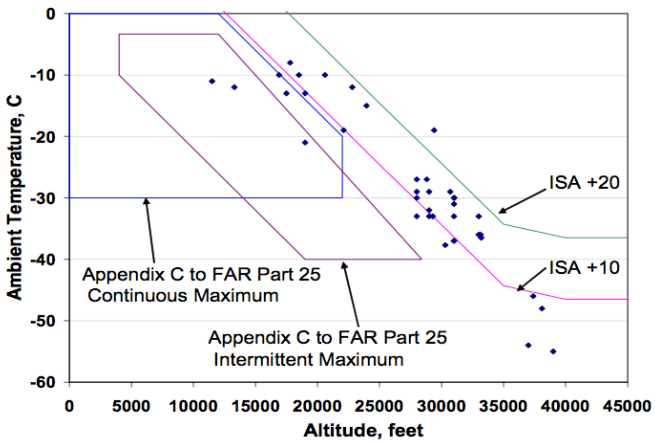

Figure 75: Event temperature-altitude envelope, superimposed on the Appendix C, FAR Part 25 icing envelopes (Mason et al. [61])

6.4 Impact of initial ice crystal temperature on compressor flow dynamics

Engine icing events were recorded at altitudes ranging from 10,000 feet to 40,000 feet at various temperatures. Mason et al. [61] have catalogued power loss events due to ice crystal icing for a spread of temperatures from −60 °C to −10 °C as shown in Fig. 75. It is important to gauge the impact of ingested ice crystal temperatures on the compressor flow behavior. The initial ice crystal temperatures considered are in the range of 213 K to 263 K. Numerical simulation for a 175 MVD with a Rosin-Rammler spread is carried out for an ice flowrate of 0.7% of the airflow rate.

As the air is compressed, the temperature increases from the front to the back of the compressor (temperature profile across compressor in Ch. 5, Fig. 34). The phase transitions of the discrete phase show a corresponding increase. The amount of water vapor increases progressively through the stages (Ch. 5, Fig. 12(a)). Figures. 76(a) and 76(b) illustrate a simultaneous drop in the mass of ice and an increase in the mass of water, respectively.

There are two inlet and one IGV control volumes before the rotor blade control volume. Hence, the number 4 on the X-axis in Fig. 76 indicates the rotor 1 inlet.

Ice completely melts in the compressor around the inlet of stator 3 (Fig. 76(a)). The mass of water, shows a peak at rotor 3 exit (Fig. 76(b)). Following this, the water evaporates until

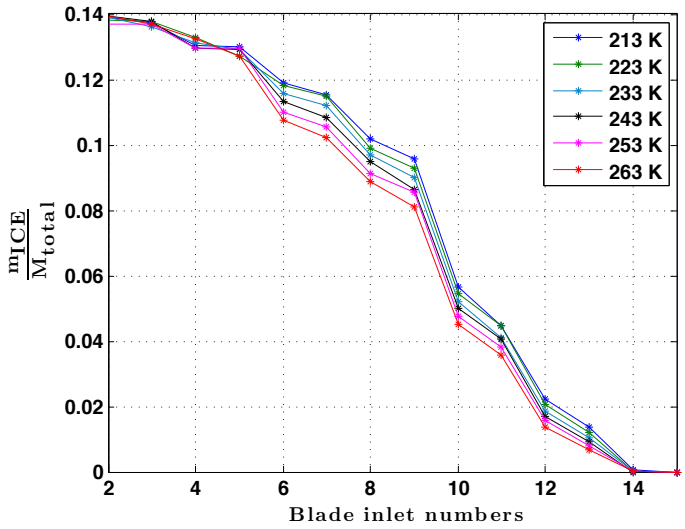

(a) Mass of ice depleting through the compressor

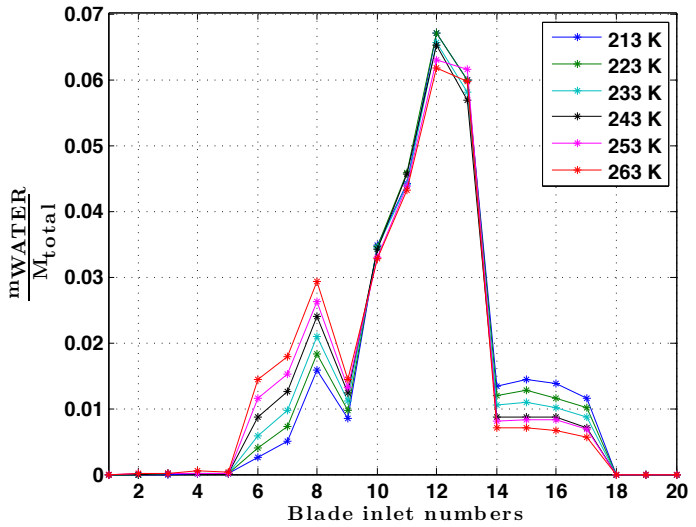

(b) Mass of water variation through the compressor

Figure 76: Ratio of mass of ice and water to the total mass of incoming ice.

only vapor remains around the inlet to the stator 4. Figure 76(a) reveals that the melting of ice is slower as the incoming ice temperature is reduced. Clearly, the corresponding mass of melted water, that usually is in the form of a thin film on the ice crystal, is lower. However, as all the ice melts and the water is in the form of droplets, it starts evaporating faster at higher initial temperature of ice, as evident from the corresponding drop in mass of water in Fig. 76(b).

Figure 77(a) plots the percentage drop in temperature of air due to ice ingestion for a

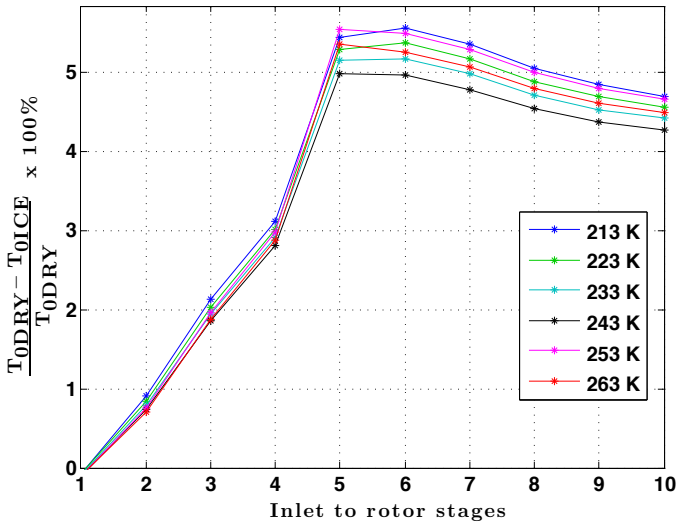

(a) Variation of stagnation temperature at rotor blade inlet

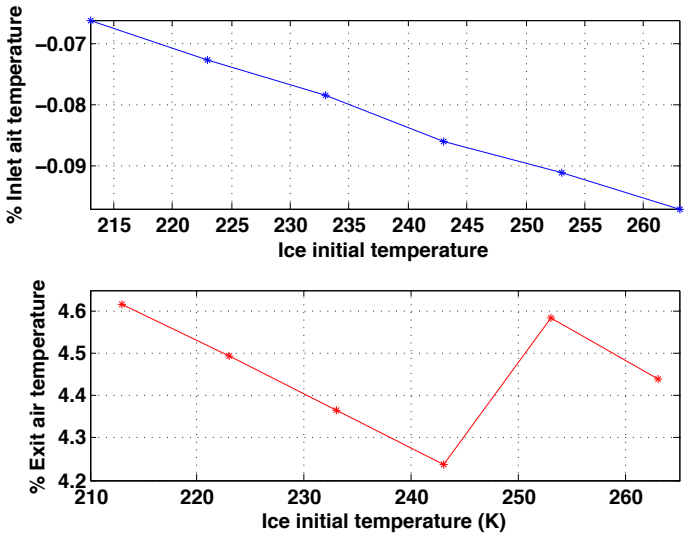

(b) Variation of stagnation temperature at inlet and exit of compressor

Figure 77: Percentage change in temperature of gas in the presence of ice as compared to dry air temperature

temperature range from 213 K to 263 K. Figure 77(a) highlights the increase in temperature drop of air until all the discrete phase evaporates till rotor 5 inlet. Figure 77(b) shows that at the inlet of the compressor the percentage drop in temperature is negative, indicating a slight increase in the air temperature in the presence of ice as compared to dry air conditions. This is predominantly due to the fact that air performs work as drag force on the incoming

ice crystals (seen as momentum loss at front end of compressor, Fig. 68(a)). The relative increase in temperature at the inlet reduces as the temperature of incoming ice crystals is reduced since the energy lost to melt the ice is higher.

Further, Fig. 77(b) shows that at the exit of the compressor, the relative drop in temperature of air decreases with an increase in temperature of the incoming ice crystals. This is considering that the energy absorbed from air to melt and evaporate is lower for discrete phase at a higher temperature. It can be deduced that the water droplets with higher initial temperatures evaporate faster to smaller sizes. It has been previously observed that smaller diameters cause a larger energy loss (temperature plot with varying MVD, Fig. 69). This explains the jump in the temperature trend of the air at the exit of the compressor.

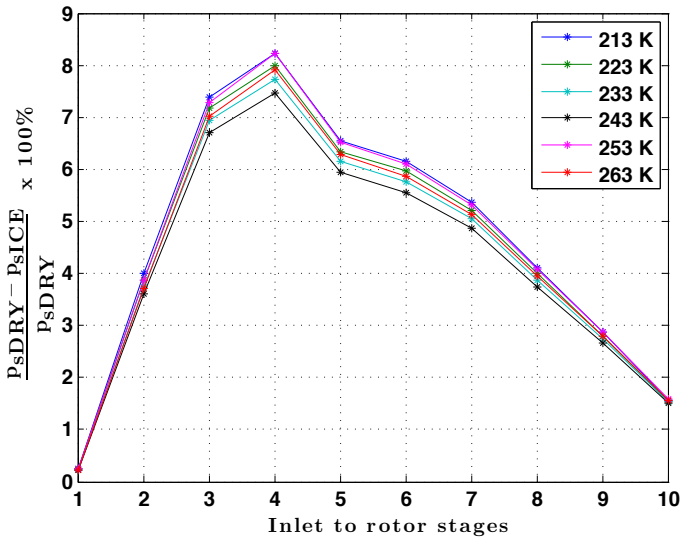

Figure 78: Variation of stagnation pressure of gas at rotor blade inlets in the presence of ice

Figure 78 shows the percentage drop in static pressure at the rotor blade inlet positions. Chapter 5, Fig. 49 discusses this trend in pressure across the compressor in the presence of ice. Figure 79 illustrates a negligible change in the gas pressure at the compressor inlet for various initial ice temperatures. Chapter 5 establishes that in the presence of ice, the gas temperature at the compressor exit exhibits a drop that results in an increase in the pressure. Thus, the trend of the gas temperature with increase in initial ice temperature shown in Fig. 77(b), dictates the trend in compressor pressure at the exit, as plotted in Fig. 79.

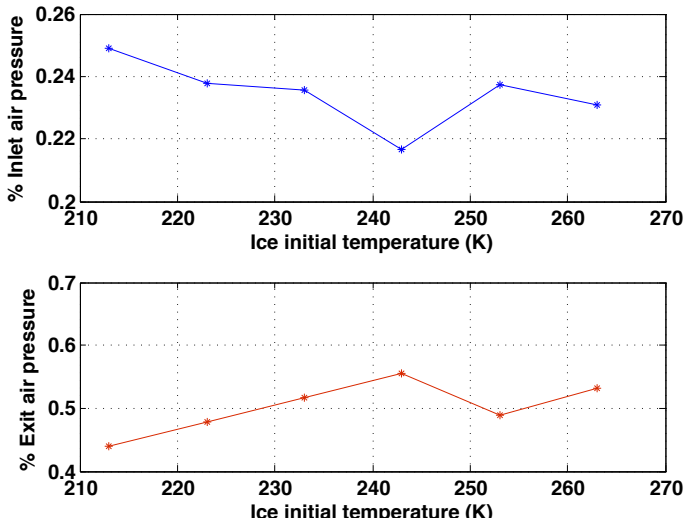

Figure 79: Variation of static pressure of gas in the presence of ice at inlet and exit of compressor

Nevertheless, the difference in the percentage pressure for the range of temperatures tested is within 0.5% and can be assumed to have a minimal impact on the icing physics.

6.5 Impact of ice break and water splash on compressor flow dynamics

The results in this section compare the response of the discrete phase and compressor gas phase to the following conditions: (1) response with semi-empirical models for breakup of ice crystals and splash of water droplets used in the present study, (2) response with semi-empirical model for breakup of ice crystals used in the present study. However, the Mundo model [69], is used for splash of water droplets, and (3) response when no collision of particles is assumed.

The Mundo model is discussed in the Chapter 2, section 2.5, describing the discrete model.

Figure 80 depicts the variation of mass of ice and specific humidity through the compressor. Without any break/splash model, the discrete phase particles flow unhindered through the compressor and they slowly absorb latent heat to melt and vaporize. On the other hand, the application of a break/splash model on the ice crystals and water droplets results in rapid conversion from ice to vapor. This is evident from the fast depletion of mass of ice and

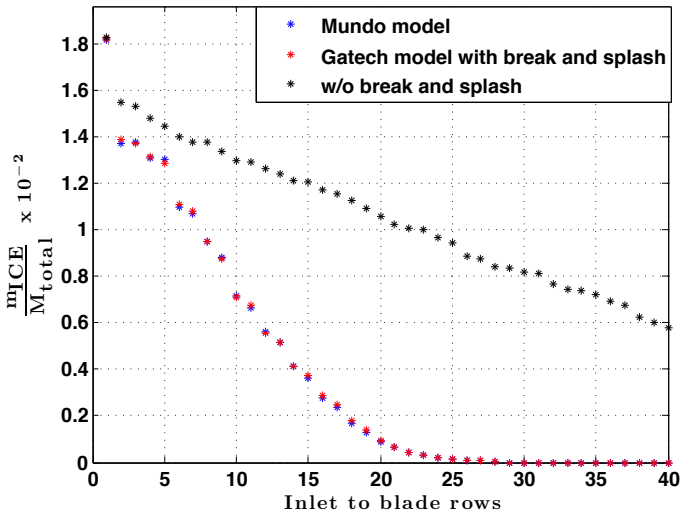

(a) Ice variation through compressor

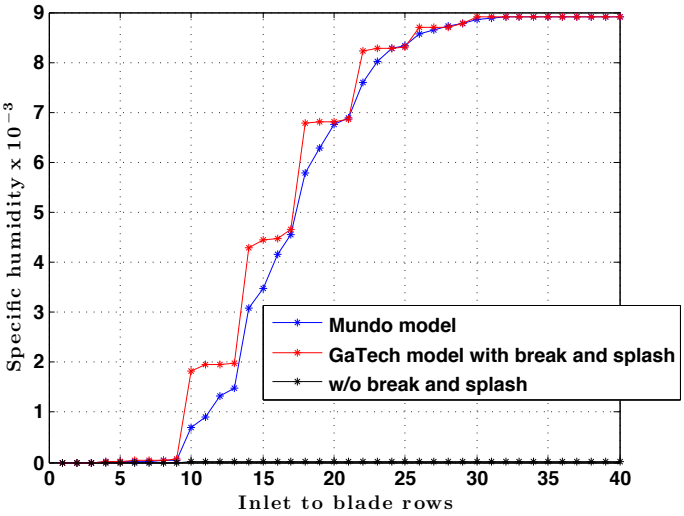

(b) Vapor variation through compressor

Figure 80: Influence of the break/splash empirical models on depletion of ice and rise of vapor through the compressor

corresponding rise in specific humidity when the particles are assumed to impinge on rotors and break. This exercise proves the inaccuracy that can arise if the apparent break/splash of the discrete phase with the rotor blades is omitted from an ice ingestion simulation.

Figure 81 displays the percent change in pressure and temperature at the inlet of all the rotors and stators of the 10 stage compressor. The percent change is based on the difference between the pressure when there is no ice ingestion and the converged pressure with ice

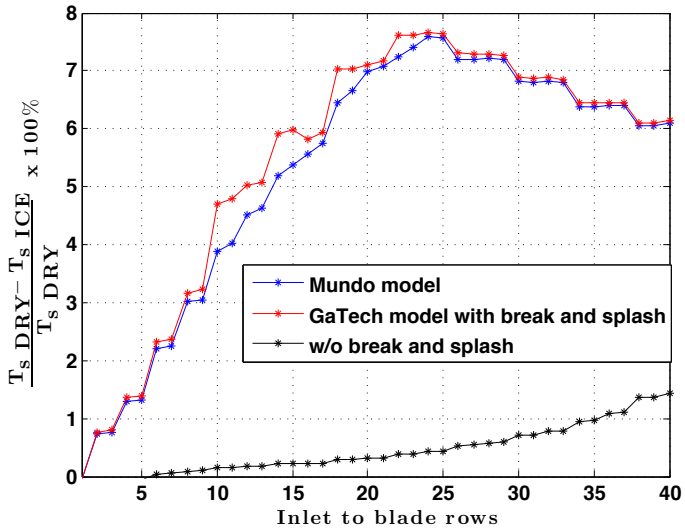

(a) Temperature variation through compressor

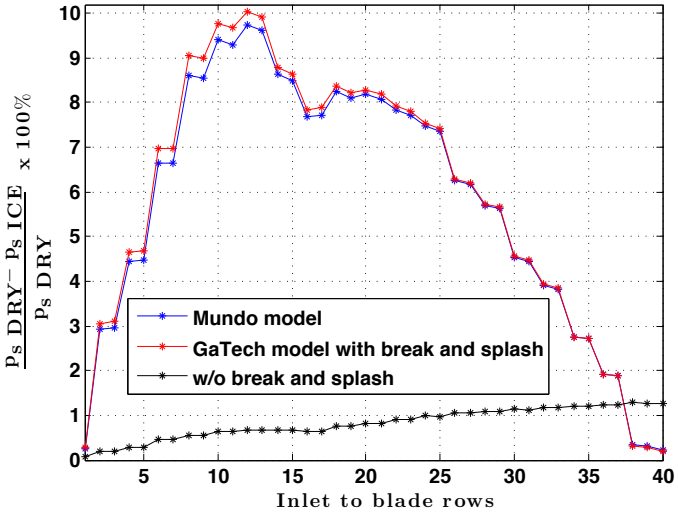

(b) Pressure variation through compressor

Figure 81: Influence of the break/splash empirical models on the compressor fluid flow response

ingestion. Similar calculations with the temperature characteristic are carried out.

The maximum shift in humid air response compared to dry air conditions that are predicted with inclusion of collisions is 10% for static pressures and 8% for static temperature. However, less than a 1.5% difference between the humid air response and the dry compressor flow characteristics is exhibited for the same input ice flow rate, if break and splash phenomena are excluded. Thus, for accurate prediction of the compressor response, break and splash models are required to be applied on the discrete phase particles. Additionally,

the application of the droplet splash model used in the present study and the Mundo splash model, both demonstrate similar results.

6.6 Comparison of ice ingestion effects with water droplet injection

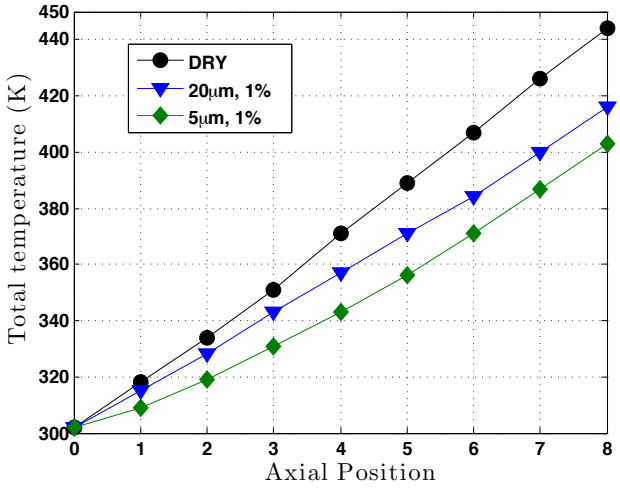

Figure 82: Axial variation of total temperature for dry and wet cases (Lou et al. [56])

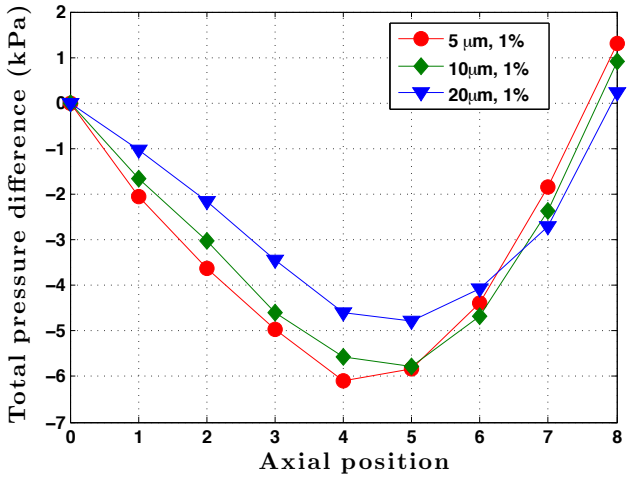

Figure 83: Axial variation of total pressure difference between each wet case and dry case (Lou et al. [56])

In the field of wet compression of axial compressors, Lou et al. [56] establishes the response of an eight stage axial compressor, to a variation in droplet sizes. A decreasing water droplet diameter increases the impact of water ingestion on the compressor performance. Reducing ice crystal sizes also exacerbates the compressor performance as compared to dry

air. The following correlation can be made between results presented by Lou et al. [56] and icing related change in performance:

1. The total temperature variation for a 1% water ingestion is demonstrated in Fig 82. The drop in temperature with water injection gets exacerbated as the droplet diameter decreases. This trend is found to match the case of ice ingestion. The total temperature with an ice flow rate of 0.7%, is plotted at the exit of the compressor in Fig. 69. The temperature drops as the ice crystal size reduces.

2. Figure 83 indicates a drop in pressure from dry conditions with water injection. The corresponding trend of pressure with ice ingestion in chapter 5, Fig. 49 also shows the same behavior.

   Further, the decreasing water droplet diameter is seen to cause a higher pressure drop in Fig. 83. Figures 71(a) and 71(b) display the variation of pressure at the exit and inlet of the compressor, respectively, with varying ice crystal sizes for a constant ice flow rate. The increased loading at the exit and unloading at the inlet with reducing ice crystal size, indicate a similar trend with water droplets as shown in Fig 83.

   The varying pressure at inlet and exit with different ice crystal sizes, resembles that shown by Bianchi et al. [8] in Figs. 66(a) and 66(b), for water droplet sizes.

CHAPTER VII

CONCLUSIONS AND FUTURE WORK

7.1 Conclusions

A quasi-one-dimensional axisymmetric transient model for the continuous gas phase and a Lagrangian model for the discrete particle phase are coupled together in a conservative framework. Based on the observations of the compressor operation for both, a dry compressor and a compressor with humid air and discrete particle multiphase flow, the following conclusions are drawn,

1. The methodology for simulating the compressor flow dynamics is first tested and validated for dry operation. Stall is predicted through throttling of the flow in a four-stage compressor. The surge points for 95% and 100% operating speeds are compared with experiments. Further, the stage that triggers stall is determined from the pressure time history.

   The stalling stage for a ten-stage compressor was previously validated from experiments by comparing the pressure transients between simulation and experiments.

   The work is significant in establishing the ability of the existing base compressor model in capturing the flow response through every stage of the compressor. This is critical to detect the stage that triggers stall by evaluating the stage-wise pressure transients.

2. The impact of ice ingestion on the flow of a ten-stage axial compressor at both nominal (98% inlet corrected speed) and ground idling (65% inlet corrected speed) conditions are investigated. The compressor stage pressure ratios reveal that ice ingestion causes the front stages to unload and the rear stages to load. The migration of the operating point towards the stall point at the rear stage with increasing ice flow rates ultimately causes the compressor to stall. The onset of stall is characterized by initial oscillations followed by a rapid decay of pressures of the last stage with the instability traveling

quickly toward the front of the compressor. Effectively, a reduction in stall margin is observed as the ice flow rate is increased.

Thus, the modeling of the unsteady response of the compressor flow dynamics is important to evaluate the impact on operability of the compressor due to ice ingestion.

3. The principal aspects of ice intake through the compressor are studied for nominal speed and ground idling speed conditions for a ten-stage compressor. At nominal speed operation, the flow temperature reduces up to the 7th stage and then starts increasing. This signifies a complete evaporation of the discrete phase before the exit of the compressor. At idling speeds, the compressor flow displays a monotonic drop in temperature up to the compressor exit indicating a possible incomplete evaporation of the discrete phase inside the compressor.

   Thus, the coupled compressor flow and icing physics model can be used to predict inlet conditions for the downstream combustor.

4. Ice ingestion causes the rematching of the operation across the stages compared to dry air operating points. The temperature and pressure drop across the compressor as compared to dry air design conditions. In the front and mid-compressor sections the pressure drop effect is dominant resulting in a decrease in density whereas the evaporative cooling at the rear stages of the compressor induces an increase in density. A simultaneous increase in velocity in the front and a decrease in velocity at the rear stages of the compressor is observed. Further, the dry air pumping capacity of the compressor increases with lower pressure at the front stages of the compressor.

   It can be concluded that the fundamental flow response of the compressor for both idling and nominal speed operations remains the same. However, the locations of maximum inflections of temperature, pressure and density are different for the two operating speeds considered in this study.

5. A benchmark is set to relate the percentage of ice that can cause compressor stall and the stage vulnerable to stall from ice ingestion. The ten-stage compressor can sustain

a $2.35\% - 2.5\%$ of ice flow rate at nominal operation and $1.9\% - 1.92\%$ ice flow rate at ground idling operation. Any additional ice ingestion triggers stall at the 10th stage for both speeds. The present work for the ten-stage compressor considered in this study shows that the last stage is vulnerable to stall due to ice ingestion.

6. A comparison is made for similarities in the influence between water droplets and ice ingestion on the compressor performance. The dominant phenomenon are the enthalpy changes due to heat absorbed from the air by the discrete phase and presence of water vapor. The front stage operation shifts towards choke while the back stages operate near stall, for both processes.

   Although a steady state simulation can capture the stage rematching with ice ingestion, the present work has considered the transients leading to stall from atmospheric ice ingestion in a multistage axial compressor.

7. A parametric study has revealed that the temperature drop with respect to dry air conditions increases as the ice crystal sizes are reduced. The stage rematching leading to unloading of the front stages with simultaneous loading of the back stages, is further exacerbated with reducing ingested ice particle size. Thus the compressor performance (power output) increases as diameter of the shed ice crystals decreases. However, the stall of the compressor will occur earlier, as the back stages approach the stall limit faster with reducing particle size.

   The simulation results demonstrate an impact of moisture on the dynamic characteristics of the compressor flow. Thus, the developed model accounts for the change in gas properties with the intake of ice.

   From the parametric studies conducted in this study, it is seen that parameters such as moisture content and the incoming ice crystal size have a dominant effect on the compressor flow response and the subsequent redistribution individual stage loading. Further, the predicted results from the model are found to be sensitive to inclusion of semi-empirical models for the particle breakup and splash on collision with the rotor blades.

7.2 Future Work

7.2.1 Effect of ice ingestion on overall engine operability

One of the operability concerns observed during flight test in a convective cloud environment is engine rollback. Engine rollback can be simulated as the engine fuel response to the compressor performance. As the ice ingestion starts, the compressor operating point shifts. McDonald [63] presented experimental data showing the higher fuel requirement to offset the increased energy claim by the compressor in the presence of hail, for maintaining the speed demanded by throttle setting . The control logic in an engine is designed to limit the fuel flow such that the operability of the engine is safeguarded by mitigation of any engine acceleration rates. Increasing ice ingestion may activate the fuel limiter thus the engine speed no longer is maintained causing rollback.

The engine rollback with decreasing speeds may result in reduced airflow further increasing the concentration of ice entering the engine. This can affect the stability of the combustor resulting in a combustor blow-out event.

The present work is done on a compressor rig system and does not include the change in engine variables such as shaft speed and additional fuel demand. It would be of interest to identify the rematching of the engine components (compressor, turbine, burner) due to ice ingestion. This can be done by embedding the current capability in a full engine model like the Commercial Modular Aero-Propulsion System Simulation 40k (C-MAPSS40k) package or Numerical Propulsion System Simulation (NPSS) engine software

7.2.2 Model Improvements

1. The present work assumes no heat loss to the metal blades. For dry air operation the metal of the compressor blades and walls are in equilibrium with the flowpath. However as ice flow starts, initially the metal will lose heat to the air and ice. This will partially balance the energy dispersed to the ice. As metal temperatures decline, less heat will be added by the metal and continued increase in fuel will become essential to maintain the engine speed. Thus, the inclusion of metal heat transfer rates in the model is desirable.

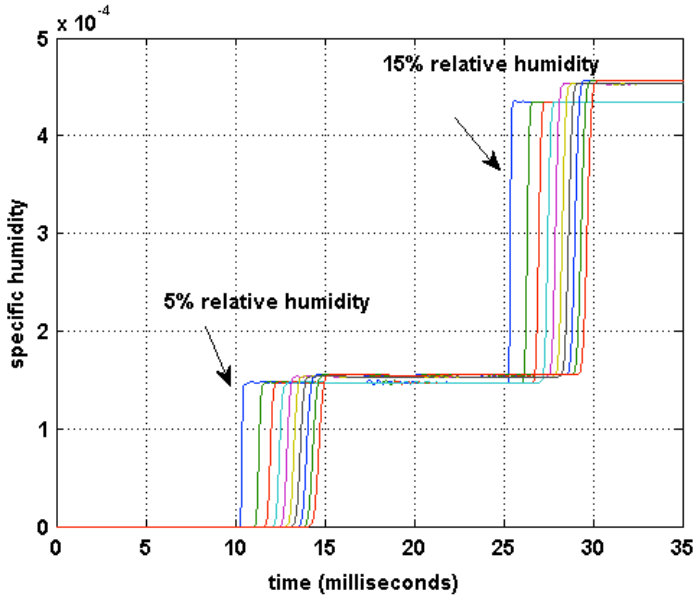

Figure 84: Specific humidity at inlet to each of the 10 rotor blades in absence of ice, with 5% and 15% humidity assumed at compressor inlet

2. The present study assumes that the compressor inlet experiences dry air inflow along with ingestion of ice crystals. However, realistically a mixed phase will exist at the inlet with ice as well as vapor inflow. Figure 84 illustrates the rise in specific humidity at each of the rotor stages, if the air flowing in through the inlet is assumed to be 5 and 15% humid, respectively, even without any ice traces. Thus the impact of ice ingestion will be greater with inclusion of inlet vapor. There will be condensation of droplets if the conditions are conducive involving low temperatures and high humidity. A droplet generation algorithm can be added.

3. The performance impact of the compressor can be quantified by computation of the efficiency. The stage-wise power and efficiency calculations will show the shift in compressor performance with increasing ice inflow rates.

4. The present system does not have any viscous terms. An additional friction term in the Euler equations is required to better represent the actual flow and help in steady state solution convergence.

APPENDIX A

VALIDATION OF COMPRESSOR PERFORMANCE FOR A TEN STAGE COMPRESSOR

Dhingra et al. [24] validated the dynamic compressor simulation for a dry compressor stall prediction capability. Pressure data from core tests corresponds to a combustor growl event. The stall sequence between the experiment and the code were compared.

In the simulation a combustor growl is simulated by including an oscillating throttle in the exit boundary condition. Method 1 is selected as the inlet boundary condition. A nonreflecting boundary condition is imposed at the exit boundary as detailed in Chapter 3, Section 3.3. However, the throttle constant given by Eq. 64, takes the following form,

$$k_T = 1 - A\sin(\omega t) \tag{74}$$

where A is the amplitude of oscillations. A constant in time or time variant amplitude can be prescribed. ω is the frequency of oscillation that simulates the combustor growl. Two sets of experimental data comparisons were carried out as detailed below.

A.1 Low amplitude combustor growl stall sequence for compressor operating near stall limit

Figure 85 shows the operation of the compressor that is relatively close to its stall line. A low amplitude combustor growl is used to initiate a compression system instability. Figure 85(a) shows the pressure time history before stall instability occurs for the test data. The pressure traces exhibit an increasing trend for the first stage, while the pressure associated with the last stage declines. A similar trend is captured by the simulation in Fig. 85(b).

The experiment displays a sharp upward pressure spike in stage 4 followed by a drop in pressure of stage 8. This is representative of a stall triggered by stage 4. A careful analysis of the simulation shows a rise in pressure at stage 4. This is followed by the compression waves traveling upstream and expansion waves downstream of the stage 4. Albeit, not as

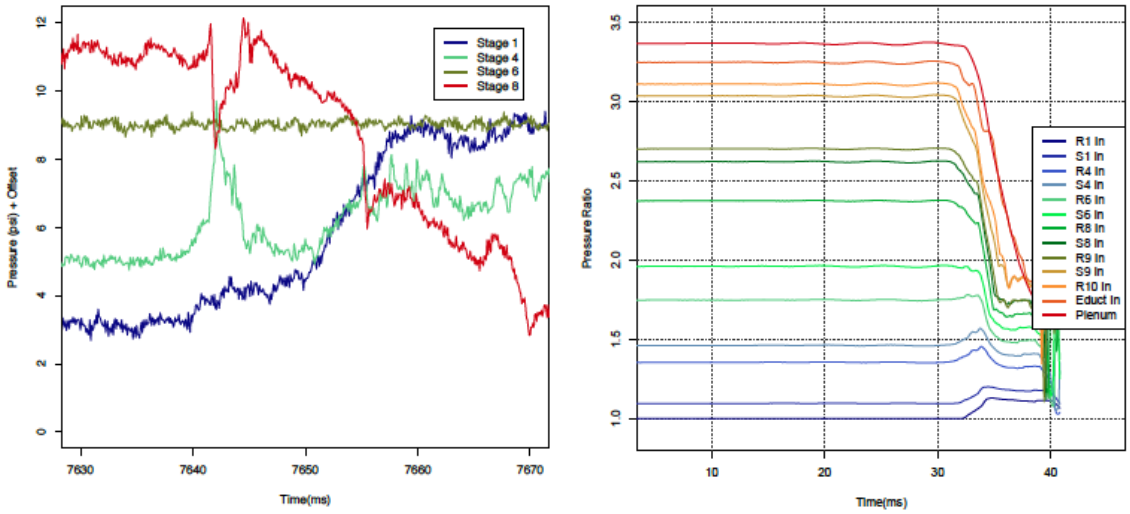

(a) Experiment (b) Simulation

Figure 85: Compressor instability with a mild excitation (reprinted with permission (Dhingra et al. [24]))

sharp as experimental trends, the pressure traces in the simulation indicate the inception of a stall instability at stage 4. Thus, the simulation and test data are consistent. Given the 1-D nature of the simulation, any circumferential phenomena cannot be captured. It is expected that the sharpness of the spike in the test data has some contribution from rotating instabilities.

A.2 High amplitude combustor growl stall sequence for compressor operating away from the stall limit

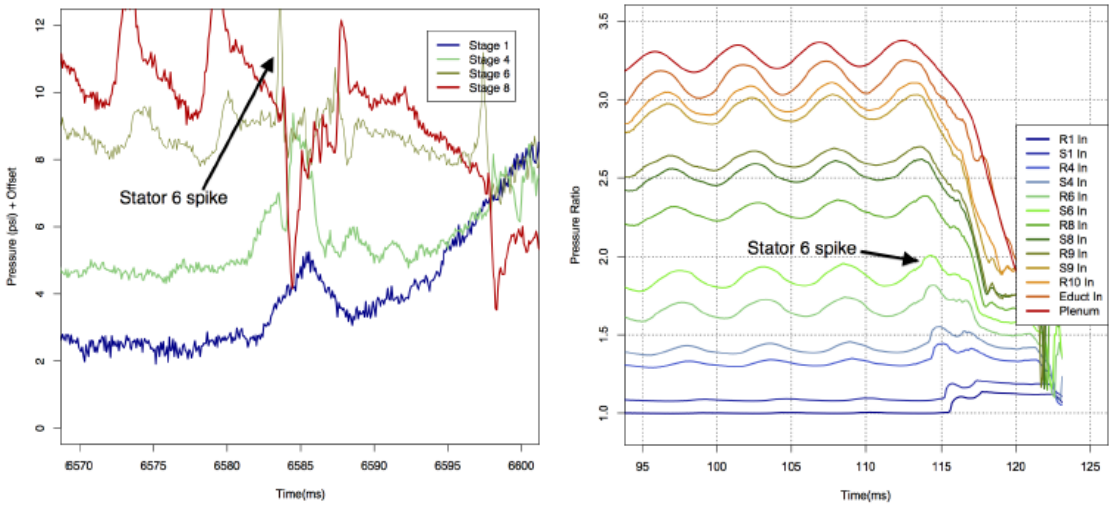

(a) Experiment (b) Simulation

Figure 86: Compressor instability with a strong excitation (reprinted with permission (Dhingra et al. [24]))

The similarity between the test data and simulation is apparent for the compressor operation away from its stall point (Fig. 86). A large amplitude pressure oscillation (combustor growl) pushes the machine into stall. The experiment in Fig. 86(a), shows that the stage 6 triggers stall instability in the compressor. The compression waves travel upstream of the stage 6, while expansion waves are created downstream, following the stall of stage 6. The simulation also shows the stall inception in stage 6 pressure signal (Fig. 86(b)).

REFERENCES

[1] Addy, H. and Veres, J. P., "An overview of NASA engine ice-crystal icing research," in *SAE 2011 Int. Conference on Aircraft and Engine Icing and Ground Deicing*, (Chicago, IL.), June 2011.

[2] Amendola, A., Mingione, G., Cailhol, D., and Hauf, T., "EURICE: An european effort for the improvement of in-flight aircraft icing safety," in *36th Aerospace Sciences Meeting and Exhibit*, (Reno, NV), Jan. 1998.

[3] Bagnoli, M., Bianchi, M., Melino, F., and Spina, P., "Development and validation of a computational code for wet compression simulation of gas turbines," *J. Eng. Gas Turbines and Power*, vol. 130, no. 1, pp. 01200 (4–8), 2008.

[4] Bain, J., Sankar, L., Garza, D., Aubert, R. J., and Flemming, R. J., "A methodology for the prediction of rotor blade ice formation and shedding," in *Proceedings of the SAE 2011 Aircraft and Engine icing and Ground Testing Conference*, (Chicago, IL.), June 2011.

[5] Beaugendre, H., Morency, F., Baruzzi, G., and Habashi, W., "Design of ice protection systems and icing certifications through cost-effective use of CFD," in *40th AIAA Aerospace Sciences Meeting*, (Reno), 2002.

[6] Berlemont, A., Grancher, M. S., and Gouesbet, G., "Heat and mass transfer coupling between vaporizing droplets and turbulence using a Lagrangian approach," *Int. J. Heat and Mass Transfer*, vol. 38, no. 16, pp. 3023–3034, 1995.

[7] Bhargava, R. K., Meher-Homji, C. B., Chaker, M. A., Bianchi, M., Melino, F., Peretto, A., and Ingistov, S., "Gas turbine fogging technology: A state-of-the-art review–Part 1: Inlet evaporative fogging - analytical and experimental aspects," *J. Eng. for Gas Turbines and Power*, vol. 129, no. 2, pp. 443–453, 2006.

[8] Bianchi, M., Melino, F., Peretto, A., Spina, P., and Ingistov, S., "Influence of water droplet size and temperature on wet compression," in *ASME Turbo Expo 2007: Power for Land, Sea, and Air*, vol. 3, (Montreal, Canada), pp. 651–662, May 2007.

[9] Boyce, M. P., *Gas Turbine Engineering Handbook*, ch. Axial-Flow Compressors. Elsevier, fourth ed., 2012.

[10] Brun, K., Kurz, R., and Simmons, H. R., "Aerodynamic instability and life-limiting effects of inlet and interstage water injection into gas turbines," *J. Eng. for Gas Turbines and Power*, vol. 128, no. 3, pp. 617–625, 2004.

[11] Califf, C. and Knezevici, D. C., "Use of a turbofan engine to measure ice crystal cloud concentration in-flight," in *50th AIAA/ASME/SAE/ASEE Joint Propulsion Conference*, (Cleveland, Ohio), July 2014.

[12] Casey, M. and Robinson, C., "A new streamline curvature throughflow method for radial turbomachinery," *J. Turbomachinery*, vol. 132, no. 3, pp. 031021 1–10, 2010.

[13] Chaker, M., Meher-Homji, C. B., and Mee, T., "Inlet fogging of gas turbine engines - Part I: Fog droplet thermodynamics, heat transfer, and practical considerations," *J. Eng. Gas Turbines and Power*, vol. 126, no. 3, pp. 545–558, 2004.

[14] Chima, R. V., "A three-dimensional unsteady CFD model of compressor stability," in *ASME Turbo Expo 2006: Power for Land, Sea, and Air*, vol. 6: Turbomachinery, Part A and B, (Barcelona, Spain), pp. 1157–1168, May 2006.

[15] Cousins, W. T., *The Dynamics of Stall and Surge Behavior in Axial - Centrifugal Compressors*. PhD dissertation, Virginia Polytechnic Institute and State University, Dept. of Mechanical Engineering, Dec. 1997.

[16] Crowe, C. T., Schwarzkopf, J. D., Sommerfeld, M., and Tsuji, Y., *Multiphase Flows with Droplets and Particles*. CRC Press, second ed., Aug. 2011.

[17] Csanady, G. T., *Theory of Turbomachines*. McGraw Hill, first ed., 1964.

[18] Cumpsty, N. A., *Compressor Aerodynamics*. Longman Scientific & Technical, 1989.

[19] Cumpsty, N. A., *Jet Propulsion: A simple guide to the aerodynamic and thermodynamic design and performance of jet engines*. Cambridge University Press, second ed., 2003.

[20] Currie, T. C., Struk, P. M., Tsao, J. C., Fuleki, D., and Knezevici, D. C., "Fundamental study of mixed–phase icing with application to ice crystal accretion in aircraft jet engines," in *4th Atmospheric and Space Environments Conference*, (New Orleans, Louisiana), June 2012.

[21] Day, I. and Freeman, C., "The unstable behavior of low and high-speed compressors," *J. Turbomachinery*, vol. 116, no. 2, pp. 194–201, 1994.

[22] Day, I., Williams, J., and Freeman, C., "Rain ingestion in axial flow compressors at part speed," *J. Turbomachinery*, vol. 130, no. 1, pp. 011024 (1–10), 2008.

[23] Denton, J., "Throughflow calculations for transonic axial flow turbines," *J. Eng. for Power*, vol. 100, no. 2, pp. 212–218, 1978.

[24] Dhingra, M., Kundu, R., and Prasad, J. V. R., "A reduced order model for compressor stall dynamics icing application," in *Georgia Tech internal report*, (Atlanta, Georgia), December 2011.

[25] Dhingra, M., Prasad, J. V. R., Tiwari, P., Nakano, T., and Breeze-Stringfellow, A., "Impact of inter-stage dynamics on stalling stage identification," in *ASME 2011 TurboExpo: Turbine Technical Conference and Exposition*, vol. 7, (Vancouver, Canada), pp. 1799–1808, Jun 2011.

[26] Djelassi, C. and Riou, A., "Detection of the ingress of water or hail into a turbine engine," June 20 2013. US Patent App. 13/818,729.

[27] Du, W., Zhu, J., and Olivier, L., "Dynamic simulations of post-stall performance in multistage axial compressors," *J. Thermal Science*, vol. 21, no. 4, pp. 311–321, 2012.

[28] Fortin, G., Laforte, J. L., and Ilinca, A., "Heat and mass transfer during ice accretion on aircraft wings with an improved roughness model," *Int. J. Thermal Sciences*, vol. 45, no. 6, pp. 595–606, 2006.

[29] Garrard, G., *ATEC: The Aerodynamic Turbine Engine Code for the Analysis of Transient and Dynamic Gas Turbine Engine System Operations*. PhD dissertation, University of Tennessee, Dept. of Mechanical Eng., 1995.

[30] Garwood, K. R., "Recommended practices for the assessment of the effects of atmospheric water ingestion on the performance and operability of gas turbine engines," tech. rep., AGARD AR-332 Advisory Group for Aerospace Research and Development, North Atlantic Treaty Organization, Neuilly-Sur-Seine, France, 1995.

[31] Giles, M. B., "Nonreflecting boundary conditions for Euler equation calculations," *AIAA Journal*, vol. 28, no. 12, pp. 2050 – 2058, 1990.

[32] Gouttebroze, S., Farooq, Saeed, and Paraschivoiu, I., "CANICE - Capabilities and current status," in *NATO/RTO Workshop, Assessment of Icing Code Prediction Capabilities*, (CIRA, Capua, Italy), 2000.

[33] Greitzer, E. M., Tan, C. S., and Graf, M. B., *Internal Flow: Concepts and Applications*. Cambridge University Press, first ed., April 2004.

[34] Hamed, A. A., Das, K., and Basu, D., "Numerical simulations of ice droplet trajectories and collection efficiency on aero-engine rotating machinery," in *43rd AIAA Aerospace Sciences Meeting and Exhibit*, (Reno, Nevada), Jan 2005.

[35] Härtel, C. and Pfeiffer, P., "Model analysis of high-fogging effects on the work of compression," in *ASME Turbo Expo 2003, collocated with the 2003 Int. Joint Power Generation Conference*, vol. 2, (Atlanta, Georgia), June 2003.

[36] Hedde, T. and Guffond, D., "ONERA Three-Dimensional Icing Model," *AIAA Journal*, vol. 33, no. 6, pp. 1038–1045, 1995.

[37] Hong, S., *Nonlinear Instability Behavior of a High Speed Multi-Stage Compressor*. Masters dissertation, Massachusetts Institute of Technology, Dept. of Aeronautics and Astronautics, Feb. 1996.

[38] Horlock, J. H., "Compressor performance with water injection," in *ASME Turbo Expo 2001: Power for Land, Sea, and Air*, vol. 1, (New Orleans, Louisiana), June 2001.

[39] Hradecky, S., "Incidents and news in aviation," *The Aviation Herald*, Aug 2013.

[40] Jennions, I. and Stow, P., "A quasi-three-dimensional turbomachinery blade design system: Part I – Throughflow analysis," *J. Eng. Gas Turbines and Power*, vol. 107, no. 2, pp. 301– 307, 1985.

[41] Jorgenson, P. C., Veres, J. P., and Jones, S. M., "Modeling the deterioration of engine and low pressure compressor performance during a rollback event due to ice accretion," in *AIAA Propulsion and Energy Forum and Exposition 2014*, (Cleveland, Ohio), July 2014.

[42] Jorgenson, P. C., Veres, J. P., Wright, W. B., and May, R. D., "Engine icing modeling and simulation (Part 1): Ice crystal accretion on compression system components and modeling its effects on engine performance," in *SAE Int. Conference on Aircraft and Engine Icing and Ground Deicing*, (Chicago, IL), June 2011.

[43] Kim, J., Sankar, L., and Kreeger, R., "Assessment of classical and extended Messinger models for modeling rotorcraft icing phenomena," in *European Rotorcraft Forum*, (Southhampton, UK), Sept. 2014.

[44] Kind, R. J., Potapczuk, M. G., Feo, A., Golia, C., and Shah, A. D., "Experimental and computational simulation of in-flight icing phenomena," *Progress in Aerospace Sciences*, vol. 34, no. 5, pp. 257–345, 1998.

[45] Klepper, J., Hale, A., Davis, M., and Hurwitz, W., "A numerical investigation of the effects of steam ingestion on compression system performance," in *ASME Turbo Expo 2004: Power for Land, Sea, and Air*, vol. 2, (Vienna, Austria), pp. 295–303, June 2004.

[46] Knezevici, D. C., Fuleki, D., Currie, T. C., and MacLeod, J. D., "Particle size effects on ice crystal accretion," in *4th Atmospheric and Space Environments Conference*, (New Orleans, Louisiana), June 2012.

[47] Kumari, N., Bahadur, V., Hodes, M., Salamon, T., Kolodner, P., Lyons, A., and Garimella, S. V., "Analysis of evaporating mist flow for enhanced convective heat transfer," *Int. J. Heat and Mass transfer*, vol. 53, no. 15–16, pp. 3346–3356, 2010.

[48] Kundu, R., Prasad, J., Saxena, S., Singh, R., Breeze-Stringfellow, A., and Nakano, T., "Modeling and analysis of ice shed in multistage compressor of jet engines," in *6th AIAA Atmospheric and Space Environments Conference*, (Atlanta, GA), June 2014.

[49] Kundu, R., Prasad, J., Tiwari, P., Breeze-Stringfellow, A., Szucs, P., Nakano, T., and Pritchard, B., "Impact of engine icing on jet engine compressor flow dynamics," in *48th AIAA/ASME/SAE/ASEE Joint Propulsion Conference & Exhibit*, (Atlanta, GA), 2012.

[50] Kurganov, A. and Tadmor, E., "New high-resolution central schemes for nonlinear conservation laws and convection-diffusion equations," *J. Computational Physics*, vol. 160, no. 1, pp. 241– 282, 2000.

[51] Lawson, R. P., Angus, L. J., and Heymsfield, A. J., "Cloud particle measurements in thunderstorm anvils and possible weather threat to aviation," *Journal of Aircraft*, vol. 35, no. 1, pp. 113–121, 1998.

[52] Leary, W., ""We freeze to please" - a history of NASA's icing research tunnel and the quest for flight safety," tech. rep., National Aeronautics and Space Administration, NASA SP-2002-4226, Washington, DC, 2002.

[53] Leishman, B. A. and Cumpsty, N. A., "Mechanism of the interaction of a ramped bleed slot with the primary flow," *J. Turbomachinery*, vol. 129, no. 4, pp. 669–678, 2006.

[54] Li, X. and Wang, T., "Effects of various modeling schemes on mist film cooling simulation," *J. Heat Transfer*, vol. 129, no. 4, pp. 472–482, 2007.

[55] Lou, D. and Hammond, D. W., "Heat and mass transfer for ice particle ingestion inside aero–engine," *J. Turbomachinery*, vol. 133, no. 3, pp. 031021 (1–5), 2010.

[56] Luo, M., Zheng, Q., Sun, L., Deng, Q., and Yang, J., "The effect of wet compression on a multistage subsonic compressor," *J. Turbomachinery*, vol. 136, no. 3, pp. 031016 (1– 8), 2013.

[57] Marrero, T. R. and Mason, E. A., "Correlation and prediction of gaseous diffusion coefficients," *AIChE Journal*, vol. 19, no. 3, pp. 498–503, 1973.

[58] Mason, J. G., Chow, P., and Fuleki, D. M., "Understanding ice crystal accretion and shedding phenomenon in jet engines using a rig test," *J. Eng. Gas Turbines and Power*, vol. 133, no. 4, pp. 041201 1–8, 2010.

[59] Mason, J. G. and Grzych, M., "The challenges identifying weather associated with jet engine ice crystal icing," in *SAE 2011 Int. Conference on Aircraft and Engine Icing and Ground Deicing*, (Chicago, Illinois), June 2011.

[60] Mason, J. G., Grzych, M., and Chow, P., "Current perspectives on jet engine power loss in ice crystal conditions: Engine icing," in *2008 AIAA Atmospheric and Space Environments*, June 2008.

[61] Mason, J. G., Strapp, J. W., and Chow, P., "The ice particle threat to engines in flight," in *44th AIAA Aerospace Sciences Meeting and Exhibit*, (Reno, Nevada), Jan 2006.

[62] May, R. D., Guo, T., Veres, J. P., and Jorgenson, P. C., "Engine icing modeling and simulation (Part 2): Performance simulation of engine rollback phenomena," in *SAE Int. Conference on Aircraft and Engine Icing and Ground Deicing*, (Chicago, IL), June 2011.

[63] McDonald, P. W., "Transient model applications. 3: Transient engine simulation and analysis of an ice ingestion test," in *von Karman Institute for Fluid Dynamics Lecture Series: Gas Turbine Engine Transient Behavior*, vol. 1, (Rhode Saint Genese, Belgium), May 1993.

[64] Meacock, A. J. and White, A. J., "The effect of water injection on multispool gas turbine behavior," *J. Eng. Gas Turbines and Power*, vol. 128, no. 1, pp. 97–102, 2004.

[65] Messinger, B. L., "Equilibrium temperature of an unheated icing surface as a function of air speed," *J. Aeronautical Sciences*, vol. 20, no. 1, pp. 29–42, 1953.

[66] Mingione, G. and Brandi, V., "Ice accretion prediction on multielement airfoils," *Journal of Aircraft*, vol. 35, no. 2, pp. 240 – 246, 1998.

[67] Mouton, P. C., "Anti-flameout safety system for a gas turbine engine," Nov. 30 1993. US Patent 5,265,414.

[68] Mugele, R. A. and Evans, H. D., "Droplet size distribution in sprays," *Industrial and Engineering Chemistry*, vol. 43, no. 6, pp. 1317 – 1324, 1951.

[69] Mundo, C., Sommerfeld, M., and Tropea, C., "On the modeling of liquid sprays impinging on surfaces," *Atomization and Sprays*, vol. 8, no. 6, pp. 625–652, 1998.

[70] Myers, W. J., "Methods and apparatus for operating gas turbine engines," Nov. 11 2003. US Patent 6,644,009.

[71] Naidoo, R. and Baboolal, S., "Application of the Kurganov - Levy semi-discrete numerical scheme to hyperbolic problems with nonlinear source terms," *Future Generation Computer Systems*, vol. 20, no. 3, pp. 465–473, 2004.

[72] Nessyahu, H. and Tadmor, E., "Non-oscillatory central differencing for hyperbolic conservation laws," *J. Computational Physics*, vol. 87, no. 2, pp. 408–463, 1990.

[73] Niazi, S., *Numerical Simulation of Rotating Stall and Surge Alleviation in Axial Compressors*. PhD dissertation, Georgia Institute of Technology, Dept. of Aerospace Engineering, July 2000.

[74] Nikolaidis, T. and Pilidis, P., "The effect of water ingestion on an axial flow compressor performance," *Proceedings of the Institution of Mechanical Engineers, Part G: J. of Aerospace Engineering*, vol. 228, no. 3, pp. 411–423, 2013.

[75] Nikolaidis, T., *Water Ingestion Effects on Gas Turbine Engine Performance*. PhD dissertation, Cranfield University, School of Engineering, Oct. 2008.

[76] Norris, G., "Core engine icing strikes russian 747-8f," *Aviation Week*, Sept. 2013.

[77] Novak, R. A., "Streamline curvature computing procedures for fluid flow problems," *J. Eng. Gas Turbines and Power*, vol. 89, no. 4, pp. 478–490, 1967.

[78] Oliver, M. J., "Validation ice crystal icing engine test in the propulsion systems laboratory at NASA Glenn Research Center," in *6th AIAA Atmospheric and Space Environments Conference*, (Atlanta, Georgia), June 2014.

[79] Olivier, L. and Olivier, A., "A quasi-one-dimensional CFD model for multistage turbomachines," *J. Thermal Science*, vol. 17, no. 1, pp. 7–20, 2008.

[80] Pasztor, A., "Airline regulators grapple with engine-shutdown peril," *The Wall Street Journal*, p. A1, April 2008.

[81] Poinsot, T. J. and Lele, S. K., "Boundary conditions for direct simulations of compressible viscous flows," *J. Computational Physics*, vol. 101, no. 1, pp. 104 – 129, 1992.

[82] Pritchard, B., Califf, C. D., Wood, P., Holm, R., van de Wall, A., and Pezzi, P., "Gas turbine engine variable bleed valve for ice extraction," Apr. 24 2014. US Patent App. 13/657,193.

[83] Rios, M. A. and Cho, Y. I., "Analysis of ice crystal ingestion as a source of ice accretion inside turbofans," in *38th Fluid Dynamics Conference and Exhibit*, (Seatlle, Washington), June 2008.

[84] Roe, P. L., "Characteristic based schemes for the Euler equations," *Ann. Rev. Fluid Mech.*, vol. 18, pp. 337–365, 1986.

[85] Roumeliotis, I. and Mathioudakis, K., "Evaluation of water injection effect on compressor and engine performance and operability," *Applied Energy*, vol. 87, no. 4, pp. 1207–1216, 2010.

[86] Rowe, A. L., "Gas turbine engine water ingestion compensation system," Dec. 5 1995. US Patent 5,471,831.

[87] Ruff, G. and Berkowitz, B., "Users manual for the NASA Lewis ice accretion prediction code (LEWICE)," in *NASA-CR-185129*, May 1990.

[88] Sang, L. and Loth, E., "Simulation of icing on a cascade of stator blades," *J. Propulsion and Power*, vol. 24, no. 6, pp. 1309–1316, 2008.

[89] Silva, G. A. L., Silvares, O. M., and Zerbini, E. J. G. J., "Numerical simulation of airfoil thermal anti-ice operation part 1: Mathematical modeling," *Journal of Aircraft*, vol. 44, no. 2, pp. 627–633, 2007.

[90] Smith, L., "The radial equilibrium equation of turbomachinery," *J. Eng. for Gas turbines and Power*, vol. 88, no. 1, pp. 1–12, 1966.

[91] Sun, L., Zheng, Q., Lin, Y., and Bhargava, R., "Understanding effects of wet compression on separated flow behavior in an axial compressor stage using CFD analysis," *J. Turbomachinery*, vol. 133, no. 3, pp. 031026(1–14), 2011.

[92] Sun, L., Zheng, Q., Luo, M., Li, Y., and Bhargava, R., "On the behavior of water droplets when moving onto blade surface in a wet compression transonic compressor," *J. Eng. Gas Turbines and Power*, vol. 133, no. 8, pp. 082001(1–10), 2011.

[93] Tan, C. S., Pritchard, B., Plybon, R., Califf, C., and et al., "Development of an icing tool for aircraft engines," in *SAE 2011 Int. Conference on Aircraft and Engine Icing and Ground Deicing*, (Chicago, Illinois), June 2011.

[94] Thompson, K. W., "Time dependent boundary conditions for hyperbolic systems," *J. Computational Physics*, vol. 68, no. 1, pp. 1–24, 1987.

[95] Turner, M. G., Reed, J. A., Ryder, R., and Veres, J. P., "Multi–fidelity simulation of a turbofan engine with results zoomed into mini-maps for a Zero-D cycle simulation," in *ASME Turbo Expo 2004: Power for Land, Sea and Air*, vol. 2, (Vienna, Austria), pp. 219–230, June 2004.

[96] Utamura, M., Kuwahara, T., Murata, H., and Horii, N., "Effects of intensive evaporative cooling on performance characteristics of land-based gas turbines," in *Joint Power Generation Conference*, (San Francisco), 1999.

[97] Veillard, X., Habashi, W. G., Aube, M. S., and Baruzzi, G. S., "FENSAP-ICE: Ice accretion in multi-stage jet engines," in *19th AIAA Computational Fluid Dynamics*, vol. 4158, (San Antonio, Texas), June 2009.

[98] Venkataramani, K. S., Plybon, R. C., Holm, R. G., and Krupp, B. R., "Aircraft engine icing model," in *46th AIAA Aerospace Sciences Meeting and Exhibit*, (Reno, Nevada), Jan 2008.

[99] Veres, J. P. and Jorgenson, P. C. E., "Modeling commercial turbofan engine icing risk with ice crystal ingestion," in *5th AIAA Atmospheric and Space Environments Conference*, (San Diego, CA), June 2013.

[100] Veres, J. P., Jorgenson, P. C., Wright, W. B., and Struk, P., "A model to assess the risk of ice accretion due to ice crystal ingestion in a turbofan engine and its effects on performance," in *4th AIAA Atmospheric and Space Environments Conference*, (New Orleans, Louisiana), AIAA, June 2012.

[101] Vidaurre, G. and Hallett, J., "Particle impact and breakup in aircraft measurement," *J. of Atmospheric and Oceanic Technology*, vol. 26, no. 5, pp. 972–983, 2009.

[102] Walsh, P. P. and Fletcher, P., *Gas Turbine Performance*. Blackwell Science Limited, second ed., 2004.

[103] Wellborn, S. R. and Koiro, M. L., "Bleed flow interactions with an axial-flow compressor powerstream," in *38th AIAA/ASME/SAE/ASEE Joint Propulsion conference & Exhibit*, (Indianapolis, Indiana), July 2002.

[104] White, A. J. and Meacock, A. J., "An evaluation of the effects of water injection on compressor performance," *J. Eng. Gas Turbines and Power*, vol. 126, no. 4, pp. 748–754, 2004.

[105] Wright, W. B., Jorgenson, P. C., and Veres, J. P., "Mixed phase modeling in GlennICE with application to engine icing," in *AIAA Atmospheric and Space Environments Conference*, (Toronto, Canada), Aug 2010.

[106] Wright, W. B. and Potapczuk, M. G., "Semi-empirical modeling of SLD physics," in *42nd AIAA Aerospace Sciences Meeting and Exhibit*, (Reno, Nevada), January 2004.

[107] Wu, C. H., "A general theory of three dimensional flow in subsonic and supersonic turbomachines of axial, radial and mixed flow," tech. rep., National Aeronautics and Space Administration , NACA TN–2604, Washington DC, Jan. 1952.

[108] Zhao, B., Li, S., Li, Q., and Zhou, S., "Impact of air system bleeding on aircraft engine performance," in *ASME–JSME–KSME 2011 Joint Fluids Engineering Conference*, vol. 1, (Hamamatsu, Japan), July 2011.

[109] Zheng, Q., Sun, Y., Li, S., and Wang, Y., "Thermodynamic analyses of wet compression process in the compressor of gas turbine," *J. Turbomachinery*, vol. 125, no. 3, pp. 489–496, 2003.